Solar Phys (2010) 265: 49–127
DOI 10.1007/s11207-010-9602-8

REMOTE SENSING OF THE INNER HELIOSPHERE

From the Sun to the Earth: The 13 May 2005 Coronal Mass Ejection

M.M. Bisi · A.R. Breen · B.V. Jackson · R.A. Fallows · A.P. Walsh · Z. Mikić · P. Riley · C.J. Owen · A. Gonzalez-Esparza · E. Aguilar-Rodriguez · H. Morgan · E.A. Jensen · A.G. Wood · M.J. Owens · M. Tokumaru · P.K. Manoharan · I.V. Chashei · A.S. Giunta · J.A. Linker · V.I. Shishov · S.A. Tyul'bashev · G. Agalya · S.K. Glubokova · M.S. Hamilton · K. Fujiki · P.P. Hick · J.M. Clover · B. Pintér

Received: 9 December 2009 / Accepted: 30 June 2010 / Published online: 3 August 2010
© The Author(s) 2010. This article is published with open access at Springerlink.com

Remote Sensing of the Inner Heliosphere
Guest Editors: M.M. Bisi and A.R. Breen

M.M. Bisi (✉) · B.V. Jackson · M.S. Hamilton · P.P. Hick · J.M. Clover
Center for Astrophysics and Space Sciences, University of California, San Diego, 9500 Gilman Drive #0424, La Jolla, CA 92093-0424, USA
e-mail: Mario.Bisi@aber.ac.uk

B.V. Jackson
e-mail: bvjackson@ucsd.edu

M.S. Hamilton
e-mail: sarhas@gmail.com

P.P. Hick
e-mail: pphick@ucsd.edu

J.M. Clover
e-mail: jclover@ucsd.edu

M.M. Bisi · A.R. Breen · R.A. Fallows · A.G. Wood · M.J. Owens · B. Pintér
Institute of Mathematics and Physics, Aberystwyth University, Penglais Campus, Aberystwyth, Ceredigion, SY23 3BZ, Wales, UK

A.R. Breen
e-mail: azb@aber.ac.uk

R.A. Fallows
e-mail: raf@aber.ac.uk

A.G. Wood
e-mail: aow@aber.ac.uk

B. Pintér
e-mail: b.pinter@aber.ac.uk

M.J. Owens
Space Environment Physics Group, Department of Meteorology, University of Reading, Earley Gate, PO Box 243, Reading, RG6 6BB, England, UK
e-mail: m.j.owens@reading.ac.uk

A.P. Walsh · C.J. Owen
Mullard Space Science Laboratory, University College London, Holmbury St. Mary, Dorking, Surrey, RH5 6NT, England, UK

A.P. Walsh
e-mail: apw@mssl.ucl.ac.uk

C.J. Owen
e-mail: cjo@mssl.ucl.ac.uk

Z. Mikić · P. Riley · J.A. Linker
Predictive Science, Inc., 9990 Mesa Rim Road Suite 170, San Diego, CA 92121, USA

Z. Mikić
e-mail: mikicz@predsci.com

P. Riley
e-mail: pete@predsci.com

J.A. Linker
e-mail: linkerj@predsci.com

A. Gonzalez-Esparza · E. Aguilar-Rodriguez
MEXART, Instituto de Geofisica, Unidad Michoacán, Universidad Nacional Autonoma de Mexico, Tzintzuntzan 310, Col. Vista Bella, Morelia, Michoacán 58098, Mexico

A. Gonzalez-Esparza
e-mail: americo@geofisica.unam.mx

E. Aguilar-Rodriguez
e-mail: ernesto@geofisica.unam.mx

H. Morgan
Institute for Astronomy, University of Hawaii, 2680 Woodlawn Drive, Honolulu, HI 96822, USA
e-mail: hmorgan@IfA.Hawaii.Edu

E.A. Jensen
ACS Consulting, 40 FM 1960 W PMB 370 Houston, TX 77090, USA
e-mail: eaj@acs-consulting.com

E.A. Jensen
MMT Observatory, Mt. Hopkins, Amado, AZ 85645, USA

M. Tokumaru · K. Fujiki
Solar-Terrestrial Environment Laboratory (STELab), Nagoya University, Furo-cho, Chikusa-ku, Nagoya 464-8601, Japan

M. Tokumaru
e-mail: tokumaru@stelab.nagoya-u.ac.jp

K. Fujiki
e-mail: fujiki@stelab.nagoya-u.ac.jp

P.K. Manoharan · G. Agalya
Radio Astronomy Centre, National Centre for Radio Astrophysics, Tata Institute of Fundamental Research, Udhagamandalam (Ooty), 643 001, India

P.K. Manoharan
e-mail: mano@ncra.tifr.res.in

Abstract We report the results of a multi-instrument, multi-technique, coordinated study of the solar eruptive event of 13 May 2005. We discuss the resultant Earth-directed (halo) coronal mass ejection (CME), and the effects on the terrestrial space environment and upper Earth atmosphere. The interplanetary CME (ICME) impacted the Earth's magnetosphere and caused the most-intense geomagnetic storm of 2005 with a Disturbed Storm Time (*Dst*) index reaching −263 nT at its peak. The terrestrial environment responded to the storm on a global scale. We have combined observations and measurements from coronal and interplanetary remote-sensing instruments, interplanetary and near-Earth *in-situ* measurements, remote-sensing observations and *in-situ* measurements of the terrestrial magnetosphere and ionosphere, along with coronal and heliospheric modelling. These analyses are used to trace the origin, development, propagation, terrestrial impact, and subsequent consequences of this event to obtain the most comprehensive view of a geo-effective solar eruption to date. This particular event is also part of a NASA-sponsored Living With a Star (LWS) study and an on-going US NSF-sponsored Solar, Heliospheric, and INterplanetary Environment (SHINE) community investigation.

Keywords Active regions, magnetic fields · Corona, models · Corona, radio emission · Coronal mass ejections, initiation and propagation · Coronal mass ejections, interplanetary · Magnetic fields, interplanetary · Magnetic fields, models · Radio bursts, association with flares · Radio scintillation · Solar wind, disturbances · Sunspots, magnetic fields · Velocity fields, solar wind · X-ray bursts, association with flares

G. Agalya
e-mail: gkagali@gmail.com

I.V. Chashei · V.I. Shishov · S.A. Tyul'bashev · S.K. Glubokova
Pushchino Radio Astronomy Observatory, Astrospace Center, Lebedev Physical Institute, Pushchino, Moscow region, 142290, Russia

I.V. Chashei
e-mail: chashey@prao.ru

V.I. Shishov
e-mail: shishov@prao.ru

S.A. Tyul'bashev
e-mail: serg@prao.ru

S.K. Glubokova
e-mail: glubokovask@yandex.ru

A.S. Giunta
Department of Physics, University of Strathclyde, John Anderson Building, 107 Rottenrow, Glasgow, G4 0NG, Scotland, UK

A.S. Giunta
Space Science and Technology Department, Rutherford Appleton Laboratory, Didcot, Oxfordshire, OX11 0QX, England, UK
e-mail: alessandra.giunta@stfc.ac.uk

S.K. Glubokova
Pushchino State University, Pushchino, Moscow region, 142290, Russia

P.P. Hick
San Diego Supercomputer Center, University of California, San Diego, 9500 Gilman Drive #0505, La Jolla, CA 92093-0505, USA

1. Introduction

The phenomenon of coronal mass ejections (CMEs), their associated interplanetary counterparts, and the effects they cause on the Earth environment are well studied but still not completely understood (see, *e.g.*, Gosling, 1993; Harrison, 2003; Schwenn *et al.*, 2005; Zhang *et al.*, 2007a). When a CME erupts from the Sun it removes a large amount of mass (solar plasma) and magnetic energy, and hurls it out into the interplanetary medium. When these interplanetary counterparts are detected, they are generally deemed interplanetary coronal mass ejections (ICMEs) (Lindsay *et al.*, 1999). A subset of ICMEs containing one or more defined flux ropes can be classified as Magnetic Clouds (MCs). This special case of flux rope within an ICME was defined by L.F. Burlaga (Burlaga *et al.*, 1981; Burlaga, Lepping, and Jones, 1990; Burlaga, 1995) as having strong magnetic fields (when compared with the surroundings) displaying a large and coherent rotation, and depressed ion temperature; thus these were named as MCs.

It is important to remember the definition of a CME (see Schwenn *et al.*, 2005; and references therein). We can define a CME as an observable change in coronal structure which occurs on time scales of a few minutes to several hours and where outward motion can be observed (Schwenn *et al.*, 2005). It also involves the instance of a newly-appearing, bright, white-light feature, which is seen as being discrete in coronagraph imagery. Note that this precise definition does not specify anything of the origin/source of the "feature" nor its nature; be it ejecta themselves or any subsequent effects driven by them (Schwenn *et al.*, 2005).

CMEs, particularly the larger ones, most-commonly originate from active regions (ARs) and can leave behind signatures of coronal dimming (see, *e.g.*, Bewsher, Harrison, and Brown, 2008). These signatures are generally best observed in extreme-ultraviolet (EUV) frequencies or sometimes in X-rays. CMEs can be accompanied by large flares, or indeed initiated by flare eruptions (see, *e.g.*, Lippiello, de Arcangelis, and Godano, 2008; and references therein). Such flares often have associated coronal radio bursts, usually of Type II or Type III, or sometimes both (see, *e.g.*, Gopalswamy *et al.*, 2005). The characteristic detection of a CME while looking at the Sun is by a localised increase in the brightness of white-light emission from the Sun due to dense features scattering more of the photospheric white light. CMEs in general contribute to about 5% of the total mass flux of the solar wind (see, *e.g.*, Lang, 2001).

At around 1 AU ($\approx 215.5\ R_{\odot}$) distance from the Sun, there are various features which can be picked up by spacecraft *in-situ* measurements during the passage of an ICME. The larger ones tend to result in density increases. There is often a change in velocity; this change is relatively sharp when the ICME velocity is much different from the "ambient" solar wind at the time. Such changes often cause interplanetary (IP) shocks to be seen before the passing of the ICME, and sometimes behind the ICME as a reverse shock. In addition, a sheath (a density increase usually composed of piled-up solar-wind plasma) is often seen behind the IP shock but before the core of material passes over the spacecraft (there is sometimes another increase in density trailing or inside the ejecta which could be associated with an erupting filament accompanying the CME), depending on the overall orientation and placement within the ICME structure which the spacecraft measures. An MC is defined (as previously stated) as a flux rope, but not all ICMEs have to contain a single MC; it is possible for multiple MCs to be contained within the single passage of a "merged" ICME structure at 1 AU distance (Burlaga *et al.*, 1981; Burlaga, Lepping, and Jones, 1990; Burlaga, 1995).

The response of the Earth's space environment and upper atmosphere (the terrestrial magnetosphere, ionosphere, and thermosphere) to solar-wind impact depends critically upon the

orientation of the interplanetary magnetic field (IMF) carried by the solar wind (see, *e.g.*, Brekke, 1997). When the north – south component of the IMF (B_z) is negative (that is, the field is oriented southwards), then direct reconnection can take place between the interplanetary and geomagnetic fields along the sub-solar region of the solar-wind – magnetosphere interface – the magnetopause (see, *e.g.*, Reiff and Burch, 1985; Schwenn *et al.*, 2005). Schwenn *et al.* (2005) also note that since the 1970s there have been two fundamentally different recognised sources of negative B_z: sources on the non-active Sun (*e.g.* high-speed streams), and sources on the active Sun (*e.g.* CMEs). The ionospheric footprint of merged flux tubes are then dragged across the polar regions, driving dayside – nightside convection in the high-latitude magnetosphere and ionospheric polar caps, with return flow at lower latitudes (Dungey, 1961). The solar wind then continues to drag the merged flux tubes downstream away from the Earth, forming a long magnetotail on the anti-solar side. We define "downstream" in the direction of flow of the solar wind, and "upstream" in the direction against the flow of the solar wind, *i.e.* back towards the Sun, and stick to this convention throughout all aspects of this paper. Reconnection eventually takes place in the magnetotail, separating the interplanetary and geomagnetic fields, and the resulting contraction of the nightside geomagnetic flux tubes accelerates plasma back towards the Earth, depositing energy in the upper atmosphere around the nightside auroral oval and perturbing ionospheric and thermospheric structure (see, *e.g.*, Brekke, 1997). This is the situation under which the most-efficient coupling between the solar wind and the Earth's space environment takes place, and leads to the most-pronounced observable effects. The precise morphology of the magnetospheric and ionospheric convection patterns also depends on the azimuthal component (B_y) of the IMF, with positive azimuthal values shifting the entire convection pattern towards the dawn section, and negative values leading to a duskwards bias.

When the north – south component of the IMF is northward, by contrast, the interplanetary and geomagnetic fields do not interact with each other at the leading edge of the magnetosphere, but some reconnection may still occur around the polar lobes of the geomagnetic field if the azimuthal component of the IMF is not too large (see, *e.g.*, Freeman *et al.*, 1993), and under appropriate conditions, plasma of dayside origin can still be observed in the nightside ionosphere (Wood *et al.*, 2008). Under these circumstances, the resulting convection patterns in the magnetosphere and high-latitude ionosphere display sunwards flow around the sub-solar point (Lockwood and Moen, 1999). Also under these conditions, energy deposition into the upper atmosphere takes place on the sunward side and energy transfer from the solar wind to the terrestrial space environment is much less efficient: auroral activity can still take place under conditions of northward IMF, but it is both weaker and considerably harder to observe (see, *e.g.*, Brekke, 1997).

Once magnetic reconnection has occurred downstream from the Earth, the magnetic field is convected away from this region. The field on the earthward side of the reconnection point is transported towards the Earth and plasma is accelerated in this direction. As the plasma travels earthward, it encounters a steady increase in the strength of the geomagnetic field and this gradient is approximately perpendicular to the direction of the field. The resulting force on the charged particles causes protons to drift westwards and electrons to drift eastwards, setting up a current in the magnetosphere flowing from east to west known as the ring current. This current, generally located between 4 Earth radii ($R_\oplus$) and 6 $R_\oplus$, creates a magnetic field which opposes the geomagnetic field and, following a magnetic storm, this depression may last for several days (Hargreaves, 1992).

The response of the terrestrial ionosphere to large-scale disturbances in the solar wind has been reviewed in detail by Buonsanto (1999) and Mendillo (2006). In summary, compression of the magnetosphere by the solar wind causes downwelling of the ionospheric

plasma. At lower altitudes plasma loss by recombination is enhanced due to the greater thermospheric densities and so the plasma density is reduced. The thermospheric composition is also modified by the neutral winds and therefore the response of the ionosphere varies with location. In addition, at polar latitudes, the IMF carried by the solar wind is connected to the geomagnetic field and the convection electric field drives the high-latitude plasma convection pattern. During storms this electric field intensifies, enhancing plasma transport, and the convection pattern also expands to lower latitudes.

We report on a series of remote-sensing observations and *in-situ* measurements of the 13 May 2005 CME, its progression through interplanetary space, and its interaction with the Earth's magnetosphere and ionosphere. The CME was an Earth-directed halo CME which erupted following a two-ribbon M8.0 solar flare at 16:13 UT above the United States (US) National Oceanic and Atmospheric Administration (NOAA) designated AR 10759, situated at latitude 12° north and longitude 54°, or 11° east of the meridian, which had associated coronal dimming later and a (possibly partial) filament eruption. Preceding this large flare was a C1.5 class flare around 12:54 UT. There is a possibility that the CME seen in white-light coronagraph images has two parts and thus could be made up of two separate CMEs merging together in the low corona. The two parts appear to be travelling at different speeds in post-processed coronagraph images. By ~ 6 solar radii ($R_{\odot}$), the inner brighter edge has caught up with the outer fainter halo-like CME feature. This flare-related CME resulted in strong coronal radio bursts (Type II and Type III) and intense MC features in the interplanetary medium near Earth. The ICME was observed as commencing at the Sun – Earth first Lagrangian Point (L_1) on 15 May 2005 at 02:11 UT with the B_z component of the IMF reaching -140 nT. It impacted the Earth under an hour later and caused the most-intense geomagnetic storm of 2005 with a Disturbed Storm Time (*Dst*) index reaching -263 nT at its peak. This particular ICME was of the MC variety. Recently, it has been noted that there were two distinct eruptions that produced two non-merging MCs (Dasso *et al.*, 2009). In addition, *in-situ* data show the presence of bi-directional electrons indicating that the field lines remain connected to the Sun. The ionosphere responded to the storm on a global scale as observed using a multi-instrument approach. We combine X-ray, EUV, white-light, and interplanetary scintillation (IPS) observations as well as measurements from multiple spacecraft, ground-based instruments, and coronal/heliospheric modelling, to detail the history of this event and summarise its features from launch to its interception by the Earth.

The first paper to discuss this event was Jones *et al.* (2006), who discussed the coronal radio-burst aspect of the CME. Bisi (2006) discussed some preliminary non-radial flow analysis of the event along with some IPS velocities. Yurchyshyn *et al.* (2006) discusses the initial investigations into the magnetic structure on the solar "surface" and how this compares with what is seen near Earth. Kozyreva and Kleimenova (2007) talked about geomagnetic pulsations and magnetic disturbances during the initial phase of the Earth-interaction of the ICME/MC. Jones (2007) discussed some preliminary velocity analysis of the event from IPS and white-light observations as well as some details of the coronal radio-burst aspect of the CME. The outer radiation belt dynamics and some magnetospheric and near-Earth *in-situ* indices were discussed by Tverskaya *et al.* (2007). Kleimenova and Kozyreva (2007) discussed the daytime quasi-periodic geomagnetic pulsations during the recovery phase on to 17 May 2005. A sigmoid-shaped AR was described by Liu *et al.* (2007). Zhang *et al.* (2007b), with their corrected CME table, provide some of the earlier CME/ICME/MC-feature values for this event. A preliminary analysis of the Carrington rotation in which this event took place (CR2029) was carried out by Bisi *et al.* (2007b) using three-dimensional (3-D) reconstruction of IPS data. Fallows *et al.* (2007) discussed the multi-frequency side of IPS observations which included the 13 – 15 May 2005 CME/ICME event. This event and

some preliminary discussion on its 3-D structure comparison from 3-D reconstruction to what is seen in coronagraph data can be found in Bisi *et al.* (2007c). Breen *et al.* (2008) introduce the poleward deflection of the fast solar wind due to the passage of the 13 – 15 May 2005 CME/ICME and we also revisit this here in this article. Jain *et al.* (2008) noted that there was a large decrease in cosmic-ray particles hitting the Earth around the time the event was interacting with the Earth's magnetosphere and this resulted in a strong Forbush Decrease (FD). An overview of ionospheric response is discussed in relation to high-Latitude ionospheric convection and Birkeland Current response by Eriksson *et al.* (2008). Lara and Borgazzi (2009) use the 13 May 2005 CME and associated Type II burst to test their analytical model for ICME transport based on hydrodynamic theory. A numerical simulation was carried out by Xie, Gopalswamy, and St. Cyr (2009) to study the propagation of this shock-driven event. The possibility of two non-interacting MCs resulting within the ICME of this event is discussed by Dasso *et al.* (2009). Haider *et al.* (2009) briefly talks about total electron content (TEC) effects at both the Earth and at Mars. Kazachenko *et al.* (2009) notes that sunspot rotation nearly triples the energy for this eruption. Finally, known to date, this event is also discussed in some detail by Gopalswamy (2010). Here, we conduct the most-complete study to date, within a single article.

For the purpose of this article, we use the term CME to describe the 13 May 2005 event in coronagraph white-light imagery and its initiation, ICME when seen in heliospheric observations of IPS and in our heliospheric 3-D tomographic reconstruction in interplanetary space, and MC when describing the event's effects and interaction with the Earth's magnetosphere and ionosphere. We review many of the available data covering this solar eruption, the passage of the associated ICME through the inner heliosphere and its interaction with the space environment of the Earth. The aim throughout has been to discuss the initiation, development, propagation, and planetary impact of the event in a clear sequential manner, and thus to provide a secure starting point for future studies of this event. A summary of each of the key steps in sequence of this event from Sun to Earth can be seen in here Table 1. In Section 2 we describe the observing techniques and models used in this paper in some detail. Section 3 describes the different types of observations and measurements of the 13 May 2005 CME and its propagation from the Sun to the Earth. We form a brief overall summary and have been able to draw some preliminary conclusions, and we discuss these in Section 4.

This paper emphasises the need for multiple techniques to analyse these many data sets available for studying eruptive events and their effects on the Earth and Earth environment. These are necessary to try to understand each process, or step, along the way from the early aspects of initiation near (or "on") the Sun, right through to the effects on, and interaction with, the Earth.

2. Techniques and Models

This section covers a brief description of the techniques and models we use here for the 13 – 15 May 2005 combination CME/ICME/MC event sequence, and serves as a brief overview of each for context in Section 3.

2.1. Observations and Modelling of Active Regions, Coronal Dimming, and Coronal Magnetic Features

Many observations of solar phenomena such as EUV observations of active regions (ARs), coronal dimming (often as a result of flare/CME initiation), and coronal magnetic features

Table 1 Summary table of the various parts of the 13 – 15 May 2005 CME/ICME/MC event sequence as discussed in this paper. The magnetosphere compression was a result of the ICME sheath crossing the Earth. Any thus-far undefined acronyms will be subsequently defined in the detailed information given in Sections 2 and 3.

13 – 15 May 2005 CME/ICME/MC Sequence and timing of each part			
Description	Instrument	Value	Date and Time (UT)
Active Region (AR)	SOHO|CDS	Latitude 12°/Longitude 54°	13 May 2005
Flare	GOES 12	C1.5 Class Flare	13 May 2005 12:54
Two-ribbon flare eruption	GOES 12	M8.0 Class Flare	13 May 2005 16:13
EUV brightenings	SOHO|EIT	N/A	13 May 2005 16:37
CME initiation	Various	500 Mm height	13 May 2005 ∼ 16:42
Initiation speed	SOHO|LASCO	POS 1689 km s^{-1}	13 May 2005 17:52
Interplanetary transit speed	Multi-IPS	900 – 1200 km s^{-1}	13 – 15 May 2005
Shock arrival at L_1	SOHO|CELIAS	∼ 1100+ km s^{-1}	15 May 2005 02:11
ICME/Sheath arrival at L_1	*Wind*|SWE	∼ 1000 km s^{-1}	15 May 2005 ∼ 02:11
Shock arrival at Earth	*Geotail*/*Cluster* 1	Magnetopause Compression/Sheath Crossing	15 May 2005 02:40
PCN Max.	Magnetometer	11.1 nT	15 May 2005 03:15
Kp Max.	Global Magnetometer Network	83	15 May 2005 06:00
AU	Auroral Magnetometers	1.3 nT	15 May 2005 06:05
AL	Auroral Magnetometers	−1.7 nT	15 May 2005 06:30
B_z component max.	*Geotail*	−140 nT	15 May 2005 06:30
Dst min.	Equatorial Magnetometers	−263 nT	15 May 2005 08:00

can be taken with instrumentation aboard the *SOlar and Heliospheric Observatory* (SOHO) (Domingo, Fleck, and Poland, 1995) spacecraft in orbit about the Sun – Earth L_1. Event studies are characterised by an exhaustive investigation of carefully picked individual CMEs that have been well observed. Event studies have required significant development of theoretical models to be able to ingest observed data and to directly simulate observed quantities. The Predictive Science, Inc., inner-coronal model has been developed to the point where it can now perform detailed CME studies using observed photospheric magnetic fields with strengths approaching kilo-Gauss (kG) fields and with spatial resolutions approaching one arc sec. With this capability, the detailed structure of the coronal magnetic field can be represented, allowing simulation of the detailed evolution of flare ribbons and to compare this with the observed evolution. Such detailed comparisons are the best way to evaluate whether a particular model of CME initiation is viable, and are an excellent way to study the connection between source regions on the Sun and MCs.

The following opportunities exist to compare model predictions with observations. In the pre-event corona, the presence (or absence) of filaments, and their morphology can be used, as can the nature of the EUV and X-ray emission, and vector-magnetic-field signatures in the photosphere that can be measured with vector magnetograms, for example with the SOHO – Michelson Doppler Imager (SOHO|MDI) (Scherrer *et al.*, 1995). In the CME-initiation and -eruption phase, it is useful to look at the evolution of Hα flare ribbons, the morphology of hard X-ray emission kernels as observed by, for example, the *Reuven Ramaty High-Energy Solar Spectroscopic Imager* (RHESSI) (see, *e.g.*, Dennis *et al.*, 1996), SOHO – Extreme-Ultraviolet Imaging Telescope (SOHO|EIT) (Delaboudinière *et al.*, 1995) waves (EIT waves), the inferred CME shock properties as deduced from radio measurements and energetic-particle acceleration, and *in-situ* magnetic-flux-rope properties.

The previous study of the 12 May 1997 CME event has demonstrated that the model can successfully match observations of the pre-event corona, and subsequently during the initiation phase of the CME, indicating that the model is now ready to be used on more challenging cases (subject of a forthcoming paper).

These comparisons with observations are enhanced and refined in this study of the 13 May 2005 CME. Observations will be able to be compared in greater detail, since stronger photospheric magnetic fields (approaching kG) can now be modelled. Whereas the 12 May 1997 CME simulations were limited in comparing with the morphology of Hα ribbons because of heavy smoothing of the magnetic field used in this first attempt; the 13 May 2005 CME models the structure of magnetic field at a greater spatial resolution. This enables the comparison with Hα ribbons in much greater detail.

2.2. White-Light Corona and Coronal Modelling

A new technique in coronal image processing enables the separation of dynamic features from the quiescent background corona in coronagraph observations. These are used in Section 3.1 to isolate the CME signal in SOHO – Large Angle Spectrometric COronagraph (SOHO|LASCO) (Brueckner *et al.*, 1995) C2 and C3 images. The technique is described in detail by Morgan and Habbal (2009). This technique first involves the removal of the F-corona and other stable image features (*e.g.* instrumental stray light) using the method of Morgan and Habbal (2007). The sharp radial gradient in brightness is then removed using the 'Normalizing Radial Graded Filter' (NRGF) (Morgan, Habbal, and Woo, 2006). Finally, regions of the corona not containing a CME are fitted to a polynomial function of brightness, and are removed. The final image contains isolated CME signal and noise.

NRGF images are also used as a base for solar rotation tomography (SRT), enabling qualitative maps of the coronal density structure to be built. A series of LASCO C2 images

covering a time period of half a solar rotation can be used to reconstruct a density map of the corona for that period. This is different to building a standard coronagraph Carrington or synoptic map, since tomographical techniques are used which help to resolve each line of sight (LOS). The method used is described by Morgan, Habbal, and Lugaz (2009).

2.3. Radio Bursts and Their Propagation

Radio bursts from the solar atmosphere and solar wind display a characteristic fall in frequency with an increasing distance from the Sun. This arises from the decreasing density (and thus plasma frequency) of the solar plasma at greater distance as the shock in the plasma moves outward from the Sun and into the interplanetary medium. Observations of the variation of the frequency with time as the frequency decreases can provide a measure of the velocity at which the shock is travelling outward from the Sun. The relationship between the plasma frequency, ν_{p}, and the electron density, N_{e}, can be described by Equation (1) where the plasma frequency is given in Hz:

$$\nu_{\mathrm{p}} = \sqrt{\frac{e^2 N_{\mathrm{e}}}{4\pi^2 \epsilon_0 m_{\mathrm{e}}}}\ \mathrm{Hz} = \sqrt{81 N_{\mathrm{e}}}\ \mathrm{Hz}. \tag{1}$$

Here, N_{e} is the electron number density in m^{-3}; ϵ_0 is the permittivity of free space $= 8.854 \times 10^{-12}\ \mathrm{F\,m}^{-1}$; e is the electronic charge of the electron $= -1.602 \times 10^{-19}$ C; and m_{e} is the mass of the electron $= 9.109 \times 10^{-31}$ kg. Figure 1 gives an example of the radio-burst flux of Type II and Type III radio bursts as compared with the quiet corona and that of the cosmic-microwave background (taken from Gopalswamy, 2004).

Solar radio bursts of Type II are characterised by a narrow band of intense radiation that drifts with time and distance from the Sun. Type II solar radio bursts are produced by the excitation of plasma waves in the ambient medium by a shock wave propagating outward from the Sun. These Type II emissions occur at the fundamental (F) and/or harmonic (H) of the plasma frequency, f, which is related to the square root of the electron plasma density, n, in the source region:

$$f = a\sqrt{n}; \tag{2}$$

here $a = 9$ for the F, $a = 18$ for the H, and f is measured in kHz and n in cm^{-3}.

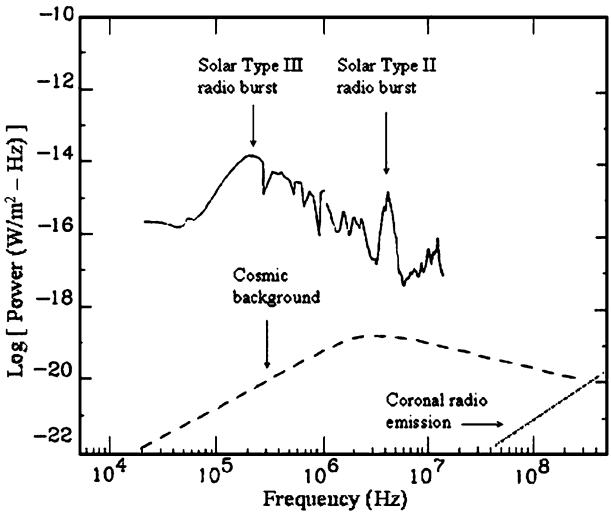

Figure 1 The level of interplanetary radio-burst flux of Type II and Type III radio bursts as compared to the quiet coronal emission and the cosmic background noise (adopted from Gopalswamy, 2004). The *in-situ* plasma frequency can be seen from the low-frequency end of the solid curve and the ionospheric cut-off at the high-frequency end of the spectrum.

Type II radio bursts are classified according to their wavelength regime: metric (m), decametric/hectometric (DH), and kilometric (km) bands. It is well established that DH to km wavelength (interplanetary) Type II radio emissions are caused by the propagation of fast CME/shocks through the interplanetary medium (Cane, Sheeley, and Howard, 1987). The frequency-drifting Type II radio emissions can, in principle, provide continuous tracking of a CME/shock from the solar corona all the way to 1 AU. Therefore, we can use radio observations to reconstruct the speed profile for a CME-driven shock.

Since the interplanetary density decreases with the square of the heliocentric distance, the CME/shock will generate radio emissions at decreasing frequencies as it propagates through interplanetary space. Reiner *et al.* (1998) showed that the radio emission from a given source region along the shock front is expected to be organised along a straight line, assuming that the speed of the shock is approximately constant. Hence, the slope of this line may be determined as:

$$\text{slope} = \frac{v}{a\sqrt{n_0}R_\odot}, \tag{3}$$

where v is the shock speed, n_0 is the density normalised to 1 AU, $R_\odot = 1.5 \times 10^8$ km, $a = 9$ if the emission is F, and $a = 18$ if the emission is H.

The observed frequency-drift rate of Type II radio emissions generated by CME-driven shocks provides a direct measurement of the shock speed. Hence the shock speed (v) is computed as:

$$v = (\text{slope})aR_\odot\sqrt{n_0}. \tag{4}$$

Type III bursts occur more frequently than Type II and are the most common flare-associated radio burst. These are narrow-band emission bursts like Type II, but are characterised by their brief duration of seconds and by their rapid change of wavelengths from decimetres to decametres. This corresponds to a decrease in frequency from around 500 MHz to 5 MHz but such Type III bursts have been observed at frequencies as low as 0.1 MHz to over 1000 MHz. Type III radio bursts can be attributed to beams of electrons thrown out from the Sun with kinetic energies of 10 keV to 100 keV and speeds of up to around half that of the speed of light. Type II and Type III bursts can occur immediately one after the other, or even simultaneously. It is generally accepted that the radio waves are emitted near the electron plasma frequency or its harmonics.

2.4. Interplanetary Scintillation (IPS) and Heliospheric Modelling

Observations of interplanetary scintillation (IPS) have been used to study the solar wind for more than 40 years (see, *e.g.*, Hewish, Scott, and Wills, 1964; Coles and Rickett, 1976; Kojima and Kakinuma, 1987; Rickett, 1992; Bisi *et al.*, 2008, 2010b). IPS arises from the scattering of radio waves by small-scale (~ 150 km) density inhomogeneities in the solar wind flowing approximately radially outward from the Sun (ΔN_e). It is a powerful tool to probe the interplanetary medium. If the variations in apparent source intensity of a distant, compact astronomical radio source (*e.g.* a quasar) as seen by two telescopes are recorded simultaneously at a time when the ray paths from the radio source to the antennas lie in a plane which passes through the centre of the Sun, then the time lag for maximum cross correlation of the signals can be used to provide a first estimate of the solar wind outflow speed (see, *e.g.*, Armstrong and Coles, 1972; Bourgois *et al.*, 1985; Breen *et al.*, 2006; Bisi *et al.*, 2006, 2010c, in this issue). This is only possible when the points of closest approach of the lines of sight from the radio source to each antenna lie close to the same Sun – Earth – source plane (see, *e.g.*, Breen *et al.*, 1996b; Coles, 1996). The point of closest approach of the

LOS to the Sun is referred to as the P-Point (or sometimes as the "impact parameter"). The accuracy to which the solar wind speed can be determined improves as the separation of the antennas projected into the plane of the sky (POS) increases (see, *e.g.*, Klinglesmith, 1997; Bisi, 2006). More sophisticated methods fitting the observed auto- and cross-correlation spectra with the results from a weak-scattering model have also been adopted for IPS data analyses (see, *e.g.*, Coles, 1996; Klinglesmith, 1997; Bisi *et al.*, 2007a; Fallows, Breen, and Dorrian, 2008).

Observations of IPS made using the radio arrays of the Solar-Terrestrial Environment Laboratory (STELab/STEL), Nagoya University, Japan at 327 MHz (Kojima and Kakinuma, 1987) have been routinely carried out for over 20 years. The mainland antennas of the European Incoherent SCATter radar (EISCAT) (Rishbeth and Williams, 1985) have been used for such observations since 1982 (see, *e.g.*, Bourgois *et al.*, 1985) at frequencies around 935 MHz, and on a regular basis since 1990 (see, *e.g.*, Breen *et al.*, 2002) at frequencies based around 928 MHz to 930 MHz, and 1420 MHz following upgrade work on two of the three sites (Wannberg *et al.*, 2002). More recently, the EISCAT Svalbard Radar (ESR) (Wannberg *et al.*, 1997) has been used for multi-frequency IPS analyses along with the mainland EISCAT telescopes (see, *e.g.*, Fallows *et al.*, 2006) operating at 500 MHz. Extremely-long baseline (ELB) IPS observations (Bisi *et al.*, 2005, 2007b; Bisi, 2006; Breen *et al.*, 2006) have also been undertaken between northern Scandinavia and the United Kingdom (UK) through the use of the Multi-Element Radio-Linked Interferometer Network (MERLIN) (Thomasson, 1986) radio telescopes based around the UK which have been operated at frequencies of around 1420 MHz, 5 GHz, and 6 GHz (see, *e.g.*, Jones, 2007) for observations of IPS (only 1420 MHz is used for the ELB IPS analyses however). The Ootacamund (Ooty) Radio Telescope (ORT) (see, *e.g.*, Swarup *et al.*, 1971) has also been used for many years for observations of IPS at 327 MHz (see, *e.g.*, Manoharan and Ananthakrishnan, 1990; Manoharan *et al.*, 2000) as well as the large Pushchino Radio Astronomy Observatory at $\sim$ 111 MHz near Moscow, Russia (see, *e.g.*, Shishov *et al.*, 2008).

ELB IPS presently uses both the EISCAT and MERLIN radio telescopes, which allow for much larger separation in observing antennas (up to $\sim$ 2000 km parallel baselines). This results in an increased ability to resolve multiple streams crossing the IPS ray path (LOS) from the antenna to the radio source on the sky. Using this technique combined with a three-mode weak-scattering IPS solar-wind model (Bisi *et al.*, 2007a; Fallows, Breen, and Dorrian, 2008) an extension of the originally-developed two-mode model (Coles, 1996), three separate velocities can be fitted and obtained for material crossing the IPS LOS. In addition, the greater-length baseline between the antennas also gives exceptional solar-wind directional information for each of the three velocity structures crossing the ELB IPS ray paths and these too can be fitted with the three-mode model (see, *e.g.*, Breen *et al.*, 2008) or with a geometrical technique (see, *e.g.*, Bisi *et al.*, 2005; Bisi, 2006).

As is done in this paper with STELab IPS data, the inner heliosphere can be reconstructed in three dimensions from observations of IPS using a time-dependent 3-D tomographic model which combines many lines of sight to undo the LOS integration (see, *e.g.*, Jackson *et al.*, 2003; Jackson and Hick, 2005). For 3-D density reconstructions however, the IPS scintillation level requires a "conversion" to *g*-level which subsequently provides a proxy for density. 3-D velocity reconstructions can be carried out from the derived IPS radial velocity values alone. Presently, the University of California, San Diego (UCSD) 3-D reconstructions incorporate a kinematic model. The resulting reconstructions are of an inner-heliosphere region typically ranging from 15 $R_{\odot}$ (the "source surface") out to approximately 3 AU. Scintillation-level measurements have been obtained using the STELab radio antenna at Kiso from 1997, and more recently (from mid-2002) from the Fuji antenna (see Jackson

and Hick, 2005; Bisi *et al.*, 2009a; and references therein). Another STELab antenna is located at Sugadaira. The newly-operating Toyokawa site will extend the STELab system to observe many more radio sources per day and is expected to be fully operational some time in 2010. STELab typically observes 20 to 40+ astronomical radio sources per day at present using the original IPS arrays, but with the old Toyokawa antenna decommissioned.

The disturbance factor (normalised scintillation level), or g-level, g, is defined by Equation (5):

$$g = m/\langle m \rangle. \tag{5}$$

Here, m is the observed scintillation level, and $\langle m \rangle$ is the mean level of scintillation for the source at the elongation at the time of observation. The scintillation-level measurements from STELab are available for each astronomical radio source as an intensity variation of the signal strength. Since density values along the LOS are not known *a priori*, the g-level proxy for density is related to small-scale density variations by Equation (6) where the small-scale density variations are assumed to have a power law dependence on heliospheric density and heliocentric distance:

$$\Delta N_{\mathrm{e}} = A_{\mathrm{c}} R^{\alpha} N_{\mathrm{e}}^{\beta}. \tag{6}$$

Here, A_{c} is a proportionality constant, R is the radial distance from the Sun, α is a power of the radial falloff, and β is the power of the density. A_{c}, α, and β are determined using best-fit comparisons with *in-situ* data at 1 AU. The values used here are as previously used for 327 MHz IPS observations: A_{c} is set equal to 1, and the two powers α and β, are -3.5 and 0.7 respectively. Further discussion of determining g-level and density can be found in Jackson *et al.* (1998, 2003), and references therein.

The 3-D reconstructions from the STELab data used here have latitude and longitude digital resolutions of $20° \times 20°$. The one-day time cadence has 6-hour interpolated increments, to yield output four times a day for the modelled structure of the inner heliosphere. The accuracy of this model is very well confirmed both in this low-resolution form, and in higher-resolution forms such as for IPS data from Ooty (see, *e.g.*, Bisi *et al.*, 2007c, 2009b) or white-light observations from the Solar Mass Ejection Imager (SMEI) (see, *e.g.*, Jackson *et al.*, 2006, 2008; Bisi *et al.*, 2008). The output of these tomographic reconstructions have successfully provided a "source surface" input into the ENLIL 3-D magneto-hydrodynamic (MHD) numerical model (see, *e.g.*, Odstrcil and Pizzo, 2002) which when propagated out through the interplanetary medium, also compares reasonably with *in-situ* measurements (see, *e.g.*, Bisi *et al.*, 2008).

Observations of IPS at 327 MHz using Ooty can probe the solar wind in the heliocentric-distance range of $\approx 10\,R_{\odot}$ to $\approx 250\,R_{\odot}$ (see, *e.g.*, Manoharan *et al.*, 2000). In the case of the CME event on 13 May 2005, the monitoring of IPS has been made on a grid of about 500 – 600 radio sources. The calibration of the temporal power spectrum of scintillation on each source provides the velocity of the solar wind and scintillation index along the LOS to the source (see, *e.g.*, Manoharan and Ananthakrishnan, 1990). Furthermore, the scintillation index of a radio source measured at a given distance from the Sun is normalised using its expected long-term average to obtain the normalised scintillation index (g), which, as mentioned previously, is directly related to the level of density turbulence in the solar wind (Manoharan, 1993). For example, the g-level value close to unity corresponds to the ambient solar wind. Whereas $g > 1$ and $g < 1$, correspond to enhanced and depleted density turbulence conditions of the solar wind respectively. This is the same as with other IPS g-level values. Therefore, a map of g-level produced in an interval of time when an ICME is crossing the IPS field of view (FOV), would result in an excessive turbulence being produced

by the ICME and its shock would likely provide the location of the ICME with respect to the Sun's centre. This is shown for Ooty data in Section 3.2.

When the separation of the receiving stations for a two-site IPS observation (*e.g.* with EISCAT) is sufficiently large (typically > 220 km), separate fast and slow peaks become resolved in the cross-correlation function (CCF) for scintillation detected at the two telescopes (Breen *et al.*, 1996b). Coles (1995, 1996) showed that these functions could be best interpreted by treating the LOS ray path for the observation as containing discrete regions of fast and slow wind, each with its own set of characteristic properties, an interpretation confirmed by the results from the *Ulysses* (Fossi, Noci, and Poletto, 1992) first orbit (see, *e.g.*, Riley *et al.*, 1997; McComas *et al.*, 1998b). By mapping the ray path ballistically back down to the corona and overlaying it on a map of white-light intensities derived from coronagraph observations over a solar rotation, it was possible to associate faster flow with those sections of the ray path overlying dark coronal regions and slow with those above bright regions, and thus use a weak-scattering model to fit for the fast and slow components separately (see, *e.g.*, Breen *et al.*, 1996a). More recently, this approach has been extended to produce a three-mode weak-scattering model (as previously mentioned), allowing stream-interaction regions (SIRs) and solar wind transients to be investigated in a more realistic manner.

In analysing the EISCAT – MERLIN ELB observation of the 13 May 2005 CME, a slightly different approach was adopted in constraining the fit of the three-mode model: instead of projecting the ray path back to a "coronal source surface" and attempting to estimate the angular extent of the CME about its presumed source region (as was done by, for example, Jones *et al.*, 2007), we took advantage of the 3-D reconstructions of solar wind normalised scintillation levels derived from STELab IPS measurements. The LOS ray path for the ELB IPS observation was overlaid on the reconstructed density in 3-D space, allowing the regions of the LOS immersed in unperturbed fast wind, fast wind near the CME boundary, and the CME itself, to be identified, and these three components of flow fitted separately (Breen *et al.*, 2008). This reduction in uncertainty in the locations of these flow components greatly improved our confidence in the accuracy of the resulting velocity estimates from the three-mode model.

2.5. Near-Earth *In-situ* (Interplanetary) Measurements

CMEs remove plasma and magnetic field from the Sun expelling them out into interplanetary space where they later become ICMEs. Measurements made by a single *in-situ* spacecraft provide some information about the local magnetic topology, and measurements of suprathermal and more energetic particles indicate the Parker spiral or a loop within the ejecta, plasma composition, and connectivity of the ICME fields back to the Sun. Even so, this information is obtained by measurements along a radial vector to the Sun as the ICME material passes over the spacecraft.

MCs, as previously mentioned in Section 1, are generally considered a subset of ICMEs (Gosling, 1990) are characterised by an enhanced magnetic-field strength, a smooth and large rotation of the magnetic-field vector, and low proton temperature. The 3-D structures of MCs have been successfully determined using flux-rope inversion models (Goldstein, 1983; Marubashi, 1986; Burlaga, Lepping, and Jones, 1990). Various *in-situ* studies with multiple spacecraft have shown that these magnetic-rope models are, however, insufficient to determine the true cross-sectional dimensions, orientation, and non-force-free nature of typical flux-rope ICMEs (Russell and Mulligan, 2002). The *in-situ* magnetic-field measurements are carried out with spacecraft instrumentation such as the *Advanced Composition Explorer* (ACE) (Stone *et al.*, 1998) – MAGnetometer (ACE|MAG) (Smith *et al.*, 1998).

CMEs are frequently associated with filament eruptions. The directions of the MC axes are found to be roughly aligned with the disappearing filaments (Bothmer and Schwenn, 1994, 1998). However, it is not so easy to quantify this association, and further developments are needed to really understand the fundamental transport mechanisms and interaction with the ambient solar wind (see, *e.g.*, the review by Démoulin, 2008). Thus, views of these structures on their way from the Sun to 1 AU are extremely important in the determination of the overall configuration of material outflow. The connection between the solar "surface" magnetic configuration of the 13 May 2005 features of this event to those at 1 AU have already been attempted by Dasso *et al.* (2009).

2.6. Magnetosphere and Ionosphere Measurements

Highly-detailed measurements of electromagnetic fields and particle distributions can be obtained from *in-situ* instrumentation aboard spacecraft. These measurements are local to each particular spacecraft. When studying the impacts of solar ejecta on the Earth's magnetosphere (and indeed any process that affects the magnetosphere on a global scale), however, a synoptic, multi-instrument approach combining space- and ground-based measurements from various sources is necessary to put those detailed measurements into context.

Here we use data from the *Geotail* (Nishida, 1994), *Cluster* (Escoubet, Schmidt, and Goldstein, 1997; Escoubet, Fehringer, and Goldstein, 2001), Los Alamos National Laboratory (LANL), and the *Imager for Magnetopause-to-Aurora Global Exploration* (IMAGE) (Gibson *et al.*, 2000) spacecraft along with ground-based data from the NORSTAR Meridian Scanning Photometer (MSP) array (Rostoker *et al.*, 1995) and geomagnetic indices derived from various ground-based magnetometers to describe the impact of the 13 May 2005 CME on the Earth's magnetosphere.

A typical measure of a geomagnetic storm's effect on the Earth is given by the Equatorial *Dst*; this is derived from the horizontal component of the magnetic variations observed at low latitudes. This is caused by the equatorial ring current which flows westward at all local times during the main phase of large geomagnetic storms.

Studies of particular relevance to the present work are those of Ebihara *et al.* (2005b, 2005a), and Hanuise *et al.* (2006). In the former study, the storm was observed and the *Dst* index, based upon the magnetic disturbance associated with the high-latitude convection pattern, reached a maximum negative excursion of -472 nT. This indicated that the anti-sunward cross-polar flow was significantly enhanced. The high-latitude convection pattern expanded equatorward to 60° MLAT. The response of the high-latitude ionosphere to an ICME was shown by Hanuise *et al.* (2006). The Auroral Electrojet (AE) index, a measure of the variation in the horizontal component of the geomagnetic field in the auroral zone increased, suggesting the presence of AEs and the polar cap potential, a measure of the electric field driving the high-latitude convection pattern also rose, which indicated enhanced convection across the polar cap.

The Polar Cap Index (PCI) is an index for magnetic activity based upon the magnetic disturbance associated with the high-latitude convection pattern (Troshichev *et al.*, 1988). This disturbance, when measured close to the pole, indicates the anti-sunward flow at all local times. Measurements of the PCI in the northern hemisphere (PCN) are made at Thule, Greenland.

The AE Indices AU and AL are derived from the variations in the horizontal component of the geomagnetic field observed in the auroral zone in the northern hemisphere. They indicate the magnitude of the AE. The AU and AL indices are intended to express the strongest current intensity of the eastward and westward AEs respectively. For each station a base

value is calculated for each month from the average of all data from the five quietest days on a global scale. This value is subtracted from each observation. AU and AL are the largest and smallest values observed at a given time after processing. The geomagnetic index, *Kp*, is derived from a global network of observatories and provides an indicator of the global geomagnetic disturbance.

3. The Observations and Measurements of the 13 – 15 May 2005 CME/ICME/MC

This section covers our observations, interpretations, and modelling of the 13 – 15 May 2005 CME/ICME/MC. It is split into three sub-sections and subsequent parts within them, in a similar context to that of Section 2. The 13 May 2005 CME was selected as the subject of an event study by a National Aeronautics and Space Administration (NASA) Living with a Star (LWS) Focused Science Team on the "CME-ICME Connection". It had good observations, an associated magnetic flux rope, and it also had a more complex photospheric and coronal magnetic field than the earlier-mentioned 12 May 1997 CME event. In addition, it is a US National Science Foundation (NSF) sponsored Solar, Heliospheric, and INterplanetary Environment (SHINE) community event which had three working group sessions during the SHINE-based Meetings in 2008, 2009 and in 2010.

We first provide a brief overview of Carrington rotation 2029 (CR2029) in which this CME occurred. There were a vast number of events during this time, which is consistent with the period being a few years into the declining phase from solar maximum. From the Association of Lunar & Planetary Observers (A.L.P.O.) Solar Section Carrington rotation commencement dates listings (http://alpo-astronomy.org/solar/rotn_nos.html), the CR2029 start date/time was 21 April 2005 07:52:27.84 UT, and the CR2029 end date/time was 18 May 2005 13:29:08.15 UT. From the Coordinated Data Analysis Workshops (CDAW) CME catalog http://cdaw.gsfc.nasa.gov/CME_list/, there were some 116 events noted as being seen in the SOHO|LASCO white-light coronagraph data. Thus, much of interplanetary space was likely dominated by transient activity throughout most (if not all) of CR2029.

Reconstructed/modelled synoptic-map overviews of CR2029 can be seen in Figures 2 and 3 using three different methods. The first (Figure 2) shows a reconstructed white-light Carrington map of SOHO|LASCO data at 4 $R_\odot$ using the technique briefly described in Section 2.2 and in detail by Morgan, Habbal, and Lugaz (2009). The density is in normalised (arbitrary) units (see Morgan, Habbal, and Lugaz, 2009). The second (Figure 3) is a comparison of 3-D reconstructed IPS results using the UCSD kinematic, time-dependent solar-wind model with STELab IPS data (top) along with a 3-D, time-dependent coronal MHD model (bottom). The MHD Model of the Solar Corona is also known as the MAS model. The top plot is produced from our IPS results at a height from the Sun of 30 $R_\odot$ and is an average of each of the individual daily reconstructions of solar wind structure in the inner heliosphere using STELab IPS data as input. The bottom plot is a velocity profile produced using the results from the MHD model, driven by the observed LOS photospheric magnetic field. The details of the algorithm have been discussed by Mikić *et al.* (1999) and Linker *et al.* (1999), and references therein. Its extension from the solar corona to the inner heliosphere is discussed by Riley, Linker, and Mikić (2001) and Riley *et al.* (2001). We computed the speed at 30 $R_\odot$ using the coronal magnetic configuration: at 1 $R_\odot$ we set the radial speed to be some value, $v_{\rm slow}$, at the boundary between open and closed field lines over a width of $\sim 6°$ (in a direction normal to the boundary) and smoothly raised it to $v_{\rm fast}$ over $\sim 3°$. We then mapped this speed profile outward along the open field lines to 30 $R_\odot$. Although this may appear somewhat *ad hoc*, it is based on the commonly-held view that fast

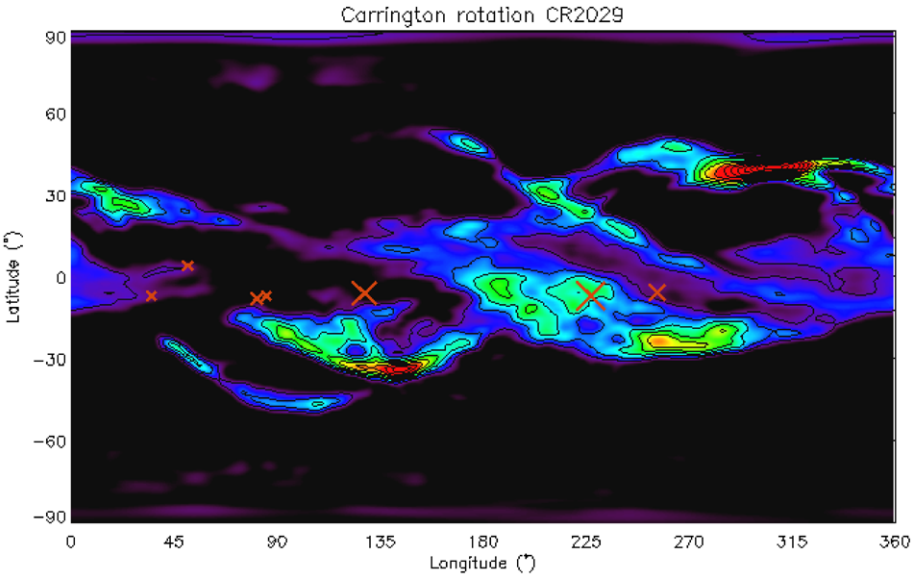

Figure 2 Reconstructed Carrington map at 4 $R_\odot$ from post-processed SOHO|LASCO imagery. This map shows the large-scale structure of the corona at this height. Sunspots are shown as red crosses superimposed on the image. The NOAA AR 10759 (Latitude N12°/Longitude 54°) lies just poleward (north) of what appears to be an edge of the streamer. The density scale gets increasingly dense from black through purple to blue, then green, and finally through yellow and orange to red for the most-dense portions in arbitrary units.

wind emanates from within coronal holes and slow wind is associated with the boundary between open and closed fields; as would be the case if closed field lines were sporadically opened through magnetic reconnection. Comparisons with *in-situ* measurements suggest that this approach is capable of reproducing the essential features of the large-scale structure of the inner heliosphere for a variety of solar conditions (Riley, Linker, and Mikić, 2001; Riley *et al.*, 2001). There are several areas where the comparison does reasonably well, but, as can be expected, there are also some significant disagreements. The STELab IPS results show speeds approaching 1000 km s^{-1} at times. This is unlikely to come from the ambient solar wind, based on *Ulysses* measurements at high latitudes (see, *e.g.*, Riley *et al.*, 1997) using the Solar Wind Observations Over the Poles of the Sun (*Ulysses*|SWOOPS) instrumentation (Bame *et al.*, 1992). These high values are likely associated with the multiple CMEs that occurred throughout CR2029. However, the structure of higher-than-*Ulysses* velocities within the fast solar wind (away from transients) has been thoroughly studied by Bisi *et al.* (2007a, 2010a) using EISCAT IPS data. The two low-speed blobs at longitudes of 240° and 330° match up reasonably well. The general sense of the low-speed band tracks well in longitude, but the IPS band is considerably thinner than the MHD solution. At the higher latitudes, the IPS results show considerably more structure.

Figure 4 shows SOHO|EIT images taken close to the initiation time of the event and then about an hour after initiation displaying a long-lived brightening of the AR and coronal dimming to the south and toward Sun centre. This in itself hints that there may have been more than one initiating event. Figure 5 shows two images from SOHO|LASCO C2 and C3 coronagraphs of the event. Further details can be found in the respective captions.

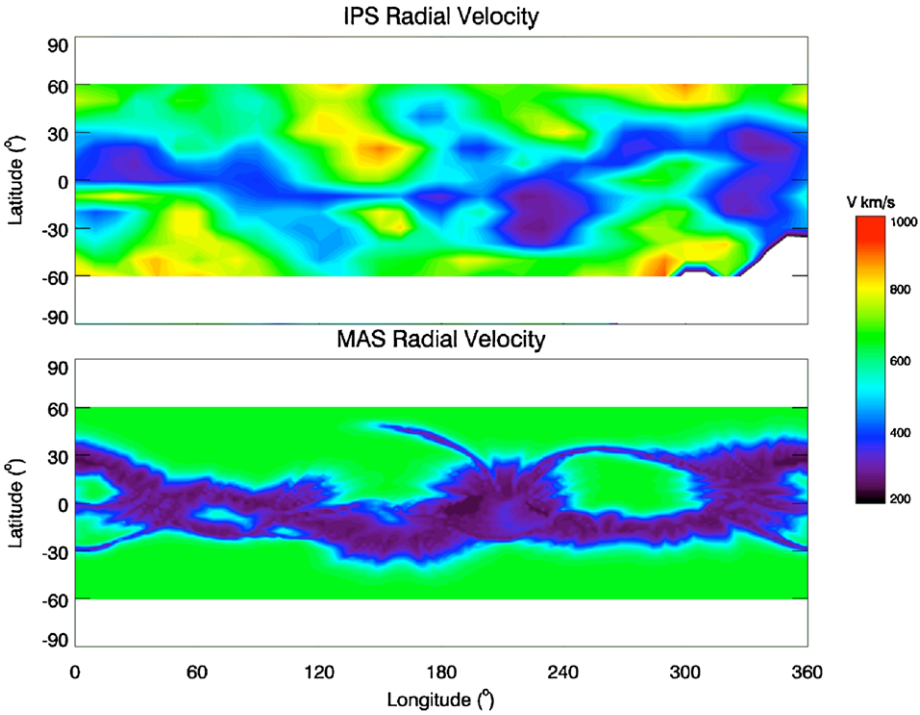

Figure 3 Reconstructed Carrington maps at 30 $R_{\odot}$ from STELab IPS observations (top) and the MAS MHD propagation model (bottom). A more complete description can be found in the text.

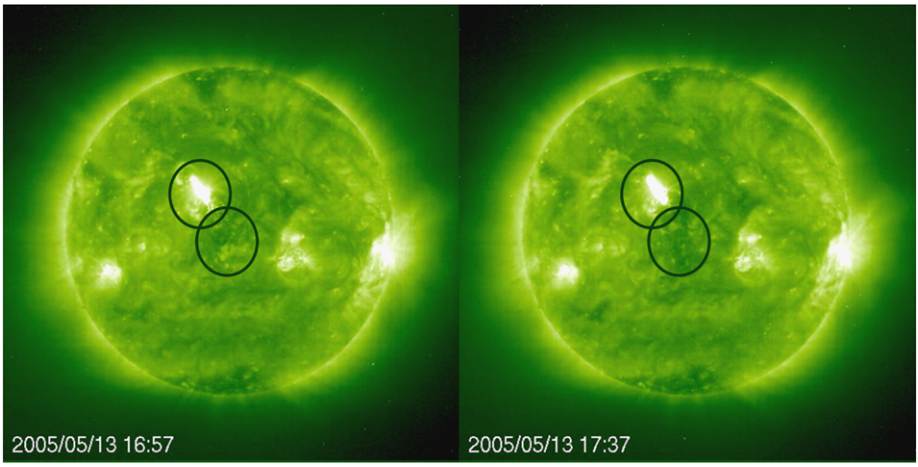

Figure 4 13 May 2005 SOHO|EIT images at 16:57 UT (left) and 17:37 UT (right), taken from Bisi *et al.* (2007b). The NOAA AR 10759 responsible for this flare/CME (bright area circled) along with associated dimming region (dark area circled). This was a relatively long-lasting period of activity for this AR. Images originally taken from the CDAW CME Catalog.

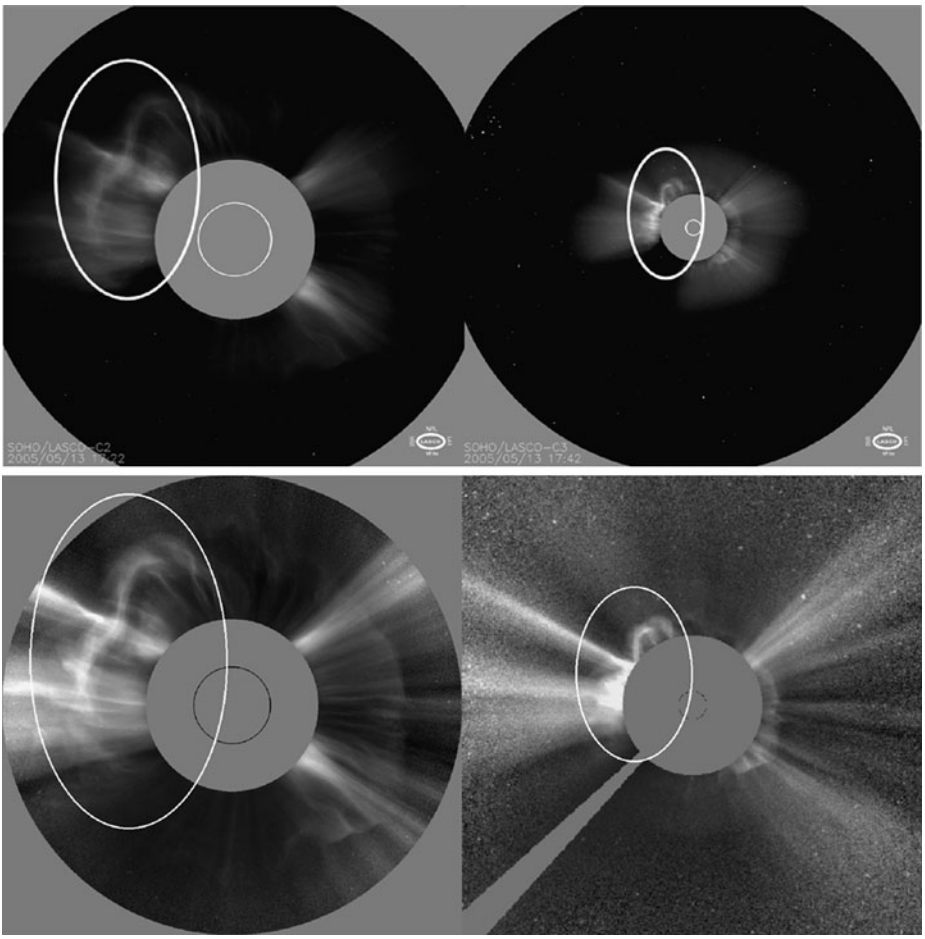

Figure 5 SOHO|LASCO images of the 13 May 2005 CME, adapted from Bisi *et al.* (2007b). The top pair of images uses the standard LASCO processing techniques and are originally taken from the CDAW CME Catalog. The bottom pair of images use the 'Normalizing Radial Graded Filter' (NRGF) post-processing as described in Section 2.2. The Halo CME pictured at 17:22 UT in LASCO C2 (left) and at 17:42 UT in LASCO C3 (right) with an estimated LASCO plane-of-the-sky (POS) speed of 1689 $\mathrm{km\,s^{-1}}$ (as stated in the CDAW CME Catalog). The CME first C2 appearance was on 13 May 2005 at 17:12:05 UT and the CME first onset at 1 $R_{\odot}$ was at 16:47:34 UT. Notice the double loop-like structure (circled) to the east of the Sun – Earth line in both sets of images and a faint near-halo feature (at all position angles in the post-processed images) seen more prominently in the C3 images. This image comparison displays the enhancement to the features due to the NRGF processing as compared with the standard processing. Further study with these improved images can be found in Section 3.1.

3.1. The Sun and Corona

As mentioned, a strong brightening can be seen in SOHO|EIT 195 Å at 16:37 UT on 13 May 2005, with many smaller precursor events throughout this day. The result was a fast CME, with an estimated POS speed of 1689 $\mathrm{km\,s^{-1}}$ leaving the Sun. It had a pre-eruption sigmoid in the NOAA *Geostationary Operational Environmental Satellites* (GOES) 12 Solar X-Ray Imager (SXI) (Hill *et al.*, 2005; Pizzo *et al.*, 2005) and dimming regions in EIT.

Table 2 Table showing a summary of the key initiating event fluxes; further details are found in the text.

Key Event Initiation Fluxes	
Description	Value
Injected magnetic flux	4.4×10^{22} Mx
Magnetic-field strength overlying filament	6 G
Drag coefficient	1.15
Flux rope ellipse eccentricity	0.87
Prominence density	2.1×10^{8} cm^{-3}

RHESSI hard X-ray data, *Transition Region And Coronal Explorer* (TRACE) (Wolfson *et al.*, 1997) data, radio, and Solar Energetic Paricle (SEP) data are also available. The source AR was well observed with both SOHO|MDI, and the Big Bear Solar Observatory (BBSO) (http://www.bbso.njit.edu/) vector magnetogram. The data from these are all presently available, thus providing an overall good magnetic coverage of the solar surface. We note, though, that the quality of the vector magnetogram is questionable for direct quantitative use.

The linear force-free model for the coronal field above AR 10759 (Abramenko and Yurchishin, 1996) has a left-handed helicity with the axis (poloidal) field oriented toward heliographic north. The eruption-process properties resemble a tether-cutting model (Moore and Labonte, 1980; Moore *et al.*, 2001) according to Yurchyshyn *et al.* (2006) and Liu *et al.* (2007). Using measurements from SOHO|LASCO, ACE|MAG, and ACE – Solar Wind Electron, Proton and Alpha Monitor (ACE|SWEPAM) (McComas *et al.*, 1998a) instrument data as boundary conditions, Yurchyshyn *et al.* (2006) fit the parameters of the Krall *et al.* (2006) erupting-flux model determining the injected magnetic flux necessary to produce the magnitude of the magnetic field at 1 AU, the overlying magnetic-field strength stabilising the filament, the drag coefficient of the solar wind, the eccentricity of the flux rope ellipse, and the initial density of the cold plasma in the prominence. These are summarised in Table 2.

To study the solar surface energetics, a background corona and solar wind with an empirical heating was first created in preparation for studies of CME initiation. Figure 6 shows a comparison between the simulated and observed EUV emission. It is a reasonable first attempt, though there are significant differences that will be improved over time. These additional refinements will likely be the subject of future publications.

We started exploring the energisation of the AR magnetic field for this event and decided to energise the AR solely by emerging transverse field from below the photosphere. No shear was applied when modelling this event, since we noticed from the 12 May 1997 study that transverse magnetic-field emergence was very effective in producing fast eruptions. The emergence was accomplished in an *ad hoc* manner by specifying the appropriate bounding electric fields using masks and functions related to traces of the photospheric neutral line, and the distance away from it. The details were presented by Z. Mikić at the 2009 SHINE Meeting working group on this event in Nova Scotia, Canada (Mikić *et al.*, 2009).

These preliminary simulations were done at high spatial resolution with kG magnetic fields using a zero-beta version of the model. This flux emergence produced highly-sheared field at the neutral line and forms a filament channel. The morphology of the filament channel is very similar to the observed Hα filament using the Improved Solar Observing Optical Network (ISOON) (http://nsosp.nso.edu/isoon/), as shown in Figure 7. This indicates that the *ad hoc* technique is reasonable. In Figure 8, the radial and transverse magnetic fields in the photosphere after the emergence are shown, and these are compared with the starting potential field. It can be seen that there is considerable shear at the neutral line. This modelled

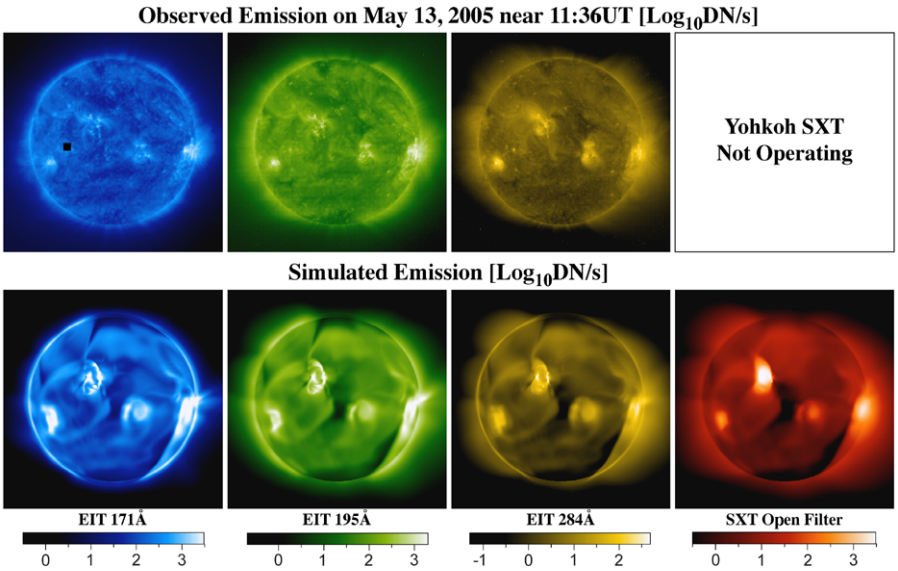

Figure 6 A quantitative comparison between observed (top) and simulated (bottom) emission for 13 May 2005. This coronal state was used for our CME-initiation studies. The parameters in the heating model may require some fine-tuning to improve the match, especially within ARs where the simulated emission is presently overly bright at all heights.

field can be compared directly with the magnetic field measured with a vector magnetogram to check how reasonable the energisation mechanism is.

The SOHO – Coronal Diagnostic Spectrometer (SOHO|CDS) (Harrison *et al.*, 1995) instrument observed and followed the NOAA AR 10759 from 13 to 15 May 2005. Observations were recorded during two time intervals on 13 May 2005: from 07:40 UT to 15:08 UT for the first set; and later from 17:56 UT to 23:29 UT for the second set. The data employed were taken using the FLARE_AR (ID 173 var. 9) observing sequence. This takes five selected wavelength ranges in the EUV portion of electromagnetic spectrum from both the Normal Incidence Spectrometer (NIS) channels. For NIS1: 359.56 Å – 361.95 Å; and for NIS2: 582.34 Å – 586.33 Å, 590.19 Å – 594.18 Å, 622.92 Å – 626.92 Å, and 627.27 Å – 631.15 Å. The sequence rasters cover an area of the Sun of 183 arc sec by 181 arc sec. Each raster takes approximately 11 minutes to complete. The first set of observations includes 39 rasters, while the second set provides an additional 30 rasters. Table 3 lists some of the observation details.

The five emission lines observed are shown in Table 4. The neutral helium line (He I) at 584.33 Å, is a strong line formed in the upper chromosphere/lower transition region. It views the coolest plasma and is in-effect a chromospheric indicator. The oxygen line (O V) at 629.73 Å, is a bright line at transition region temperatures, and the magnesium line (Mg X) at 624.94 Å, is a quite-bright coronal line. The iron line (Fe XVI) at 360.76 Å, is used to determine high-temperature plasmas and is particularly bright in ARs but not usually bright in the quiet Sun. Finally, the other iron line (Fe XIX) at 592.23 Å, identified as a magnetic-dipole transition within the ground configuration (Widing, 1978), is a typical signature of flares. The formation temperature of each line was taken from the peaks of the contribution functions calculated using the Atomic Data and Analysis Structure (ADAS) database (Summers, 2004; http://adas.phys.strath.ac.uk/). Thus in summary, the five lines

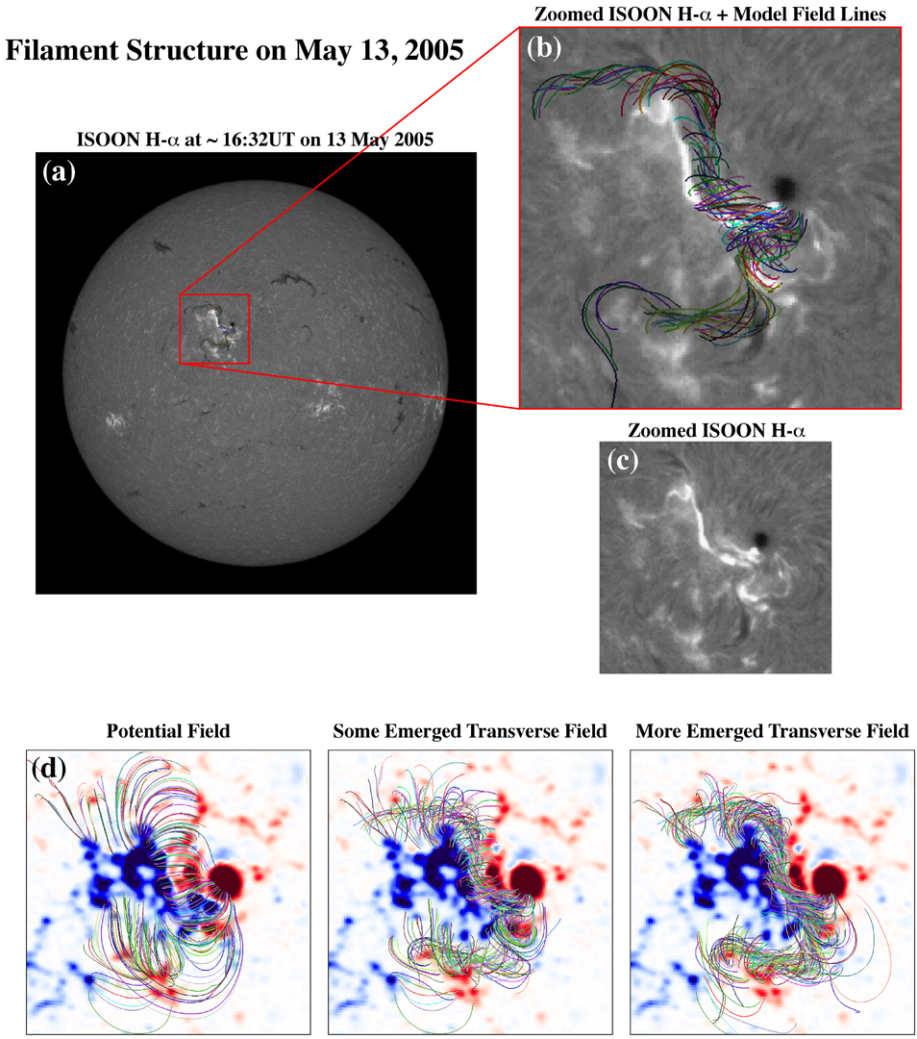

Figure 7 Comparison between an *ad hoc* generated filament and an Hα Improved Solar Observing Optical Network (ISOON) image for the 13 May 2005 CME event study. The simulation was energised by emergence of transverse magnetic field from below the photosphere in the vicinity of the neutral line. The ISOON image, which was taken about two minutes after the commencement of the flare, shows the beginning of the flare ribbons. The filament has already erupted partially, but there is good agreement between the simulated filament and the ISOON filament, and the filament channel delineated by the flare ribbons. Images (a) and (b) show the Hα image with model field lines superimposed, while (c) shows the detail of the Hα image of the AR. The panels in (d) show the development (from left to right) of the sheared field in the filament channel as the transverse field has emerged.

cover a large temperature range simultaneously (3×10^4 K to 9×10^6 K), allowing us in principle, to examine the contribution of the ejection processes of plasmas at very different temperatures in the solar atmosphere.

The SOHO|CDS data for the two sets of observations were reduced and calibrated (Lang *et al.*, 2002). Only three individual times from each set were chosen, and plots of intensity

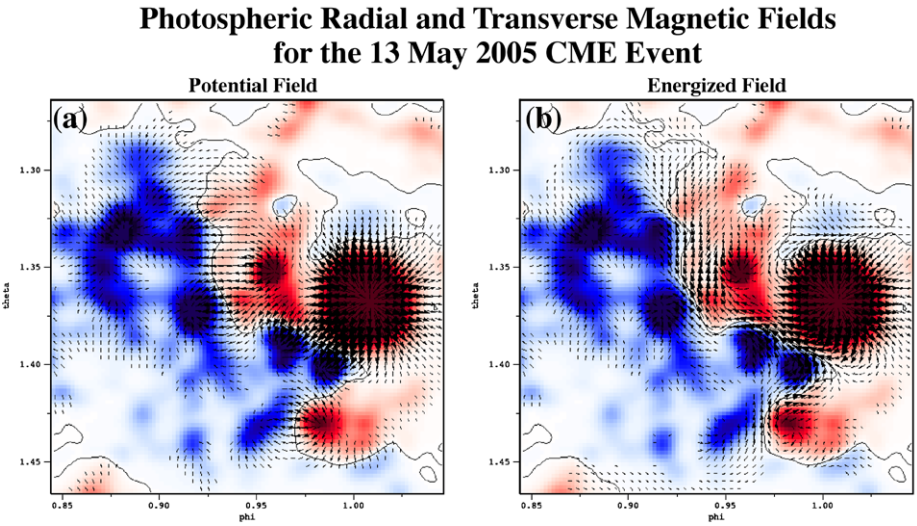

Figure 8 Simulated "vector magnetograms" showing the magnetic field in the photosphere. The radial component of the magnetic field is shown in the intensity image; red indicates positive values and blue indicates negative values. The arrows show the transverse magnetic field. The neutral line is indicated in black. The left panel (a) shows the potential magnetic field that is used to initiate the calculation. The right panel (b) shows the magnetic field after transverse field has emerged in the vicinity of the neutral line. The emerged field creates a filament channel with highly-sheared magnetic field along the neutral line.

and spectra were computed. These can be seen in Figures 9 through 12. Figures 9 and 10 give the distribution of intensity of the examined AR before the eruption, which occurred at 16:13 UT (Figure 9), and in the post-flare phase (Figure 10). The sigmoid shape (see, *e.g.*, Canfield, Hudson, and McKenzie, 1999) that characterises this AR before the flare and subsequent CME (as described in some detail by Liu *et al.*, 2007) could be seen more than eight hours before the event (images at 07:40 UT in Figure 9). The symmetric shape is well defined in the Fe XVI and Fe XIX bands (such as in the EIT images at 171 Å and 195 Å, and in the TRACE 171 Å images), but is also clearly visible in the Mg X and He I bands, where the emission is more intense near the footpoints. After the explosive M8.0 flare event, CDS observed the AR from 17:56 UT until 23:29 UT showing the evolution from the sigmoidal field to loops of an arcade (as illustrated by Figure 10). The spectra, presented in Figures 11 and 12, describe the change in the averaged intensity for each wavelength band, both in the pre-flare and post-flare state (respectively) providing a general overview of the event. In addition, the integrated intensity along the line profiles is plotted as function of time, taking into account the full sets of rasters (Figure 13). The increase of intensity just before the flare is not evident because of the lack of CDS observations when the eruption happened (between 15:08 UT and 17:56 UT). However, it is possible to detect a signature of such increase in the plot for the second set of observations, where, after a maximum value, the intensity of each line starts to decrease rapidly. An earlier detection of the smaller flare may also be possible from these spectra and plots.

These basic spectroscopic tools and qualitative information may allow for an analysis of the CME onset process and the subsequent phase by detection of plasma flows in the various temperature regimes, with supporting magnetograms and observations from coronagraphs.

Table 3 Details of the observations gathered using SOHO|CDS on 13 May 2005.

First Set							
Filename	Observation Time (UT)	Exp. s	X-cen. (arc sec)	Y-cen. (arc sec)	X-width (arc sec)	Y-width (arc sec)	Object (NOAA)
s32622r00	07:40:30	8.00	−262.4	234.2	182.8	181.4	AR 10759
s32622r02	08:01:47	8.00	−262.2	234.1	182.8	181.4	AR 10759
s32622r03	08:13:19	8.00	−262.2	234.0	182.8	181.4	AR 10759
s32622r04	08:24:51	8.00	−262.4	234.2	182.8	181.4	AR 10759
s32622r05	08:36:25	8.00	−250.1	232.9	182.8	181.4	AR 10759
s32622r06	08:47:55	8.00	−250.5	233.3	182.8	181.4	AR 10759
s32622r07	08:59:27	8.00	−250.6	233.4	182.8	181.4	AR 10759
s32622r08	09:10:58	8.00	−250.5	233.5	182.8	181.4	AR 10759
s32622r09	09:22:30	8.00	−250.6	233.3	182.8	181.4	AR 10759
s32622r10	09:34:05	8.00	−245.6	238.2	182.8	181.4	AR 10759
s32622r11	09:45:34	8.00	−245.5	238.1	182.8	181.4	AR 10759
s32622r12	09:57:07	8.00	−245.7	238.3	182.8	181.4	AR 10759
s32622r13	10:08:38	8.00	−245.9	238.5	182.8	181.4	AR 10759
s32622r14	10:20:10	8.00	−245.8	238.4	182.8	181.4	AR 10759
s32622r15	10:31:45	8.00	−239.3	231.9	182.8	181.4	AR 10759
s32622r16	10:43:14	8.00	−239.3	231.9	182.8	181.4	AR 10759
s32622r17	10:54:46	8.00	−239.3	231.9	182.8	181.4	AR 10759
s32622r18	11:06:18	8.00	−239.3	231.9	182.8	181.4	AR 10759
s32622r19	11:17:51	8.00	−239.3	231.9	182.8	181.4	AR 10759
s32622r20	11:29:24	8.00	−226.9	234.7	182.8	181.4	AR 10759
s32622r21	11:40:54	8.00	−226.8	234.6	182.8	181.4	AR 10759
s32622r22	11:52:26	8.00	−226.8	234.6	182.8	181.4	AR 10759
s32622r23	12:03:58	8.00	−226.9	234.7	182.8	181.4	AR 10759
s32622r24	12:15:30	8.00	−226.9	234.7	182.8	181.4	AR 10759
s32622r25	12:27:04	8.00	−217.5	234.7	182.8	181.4	AR 10759
s32622r26	12:38:34	8.00	−217.6	234.5	182.8	181.4	AR 10759
s32622r27	12:50:06	8.00	−217.8	234.4	182.8	181.4	AR 10759
s32622r28	13:01:38	8.00	−217.5	234.7	182.8	181.4	AR 10759
s32622r29	13:13:10	8.00	−217.6	234.5	182.8	181.4	AR 10759
s32622r30	13:24:45	8.00	−209.0	235.5	182.8	181.4	AR 10759
s32622r31	13:36:14	8.00	−208.9	235.6	182.8	181.4	AR 10759
s32622r32	13:47:46	8.00	−208.9	235.6	182.8	181.4	AR 10759
s32622r33	13:59:18	8.00	−208.9	235.6	182.8	181.4	AR 10759
s32622r34	14:10:50	8.00	−208.9	235.6	182.8	181.4	AR 10759
s32622r35	14:22:24	8.00	−204.2	230.7	182.8	181.4	AR 10759
s32622r36	14:33:54	8.00	−204.1	230.6	182.8	181.4	AR 10759
s32622r37	14:45:26	8.00	−204.2	230.8	182.8	181.4	AR 10759
s32622r38	14:56:58	8.00	−204.2	230.7	182.8	181.4	AR 10759
s32622r39	15:08:30	8.00	−204.1	230.6	182.8	181.4	AR 10759

Table 3 (*Continued*)

Second Set							
Filename	Observation Time (UT)	Exp. s	X-cen. (arc sec)	Y-cen. (arc sec)	X-width (arc sec)	Y-width (arc sec)	Object (NOAA)
s32624r00	17:56:47	8.00	−179.5	234.5	182.8	181.4	AR 10759
s32624r01	18:07:12	8.00	−179.5	234.5	182.8	181.4	AR 10759
s32624r02	18:18:04	8.00	−179.5	234.5	182.8	181.4	AR 10759
s32624r03	18:29:36	8.00	−179.5	234.5	182.8	181.4	AR 10759
s32624r04	18:41:08	8.00	−179.5	234.5	182.8	181.4	AR 10759
s32624r05	18:52:42	8.00	−168.2	232.5	182.8	181.4	AR 10759
s32624r06	19:04:12	8.00	−168.2	232.5	182.8	181.4	AR 10759
s32624r07	19:15:45	8.00	−168.1	232.6	182.8	181.4	AR 10759
s32624r08	19:27:16	8.00	−168.1	232.6	182.8	181.4	AR 10759
s32624r09	19:38:48	8.00	−168.1	232.6	182.8	181.4	AR 10759
s32624r10	19:50:23	8.00	−160.0	234.9	182.8	181.4	AR 10759
s32624r11	20:01:52	8.00	−160.1	234.7	182.8	181.4	AR 10759
s32624r12	20:13:24	8.00	−160.2	234.8	182.8	181.4	AR 10759
s32624r13	20:24:56	8.00	−160.3	234.7	182.8	181.4	AR 10759
s32624r14	20:36:28	8.00	−160.2	234.8	182.8	181.4	AR 10759
s32624r15	20:48:02	8.00	−154.2	229.4	182.8	181.4	AR 10759
s32624r16	20:59:32	8.00	−154.1	229.5	182.8	181.4	AR 10759
s32624r17	21:11:04	8.00	−154.2	229.4	182.8	181.4	AR 10759
s32624r18	21:22:36	8.00	−154.2	229.4	182.8	181.4	AR 10759
s32624r19	21:34:08	8.00	−154.1	229.5	182.8	181.4	AR 10759
s32624r20	21:45:42	8.00	−142.6	233.6	182.8	181.4	AR 10759
s32624r21	21:57:12	8.00	−142.5	233.5	182.8	181.4	AR 10759
s32624r22	22:08:44	8.00	−142.7	233.7	182.8	181.4	AR 10759
s32624r24	22:31:48	8.00	−143.2	234.2	182.8	181.4	AR 10759
s32624r23	22:20:16	8.00	−142.8	233.8	182.8	181.4	AR 10759
s32624r25	22:43:22	8.00	−135.8	234.4	182.8	181.4	AR 10759
s32624r26	22:54:52	8.00	−135.8	234.4	182.8	181.4	AR 10759
s32624r27	23:06:24	8.00	−135.8	234.4	182.8	181.4	AR 10759
s32624r28	23:17:56	8.00	−135.8	234.4	182.8	181.4	AR 10759
s32624r29	23:29:28	8.00	−135.8	234.4	182.8	181.4	AR 10759

The front edge of the 13 May 2005 CME event is observed by the SOHO|LASCO C2 coronagraph at 17:22 UT, then by the C3 coronagraph at 17:42 UT. Both these observations are shown using appropriate post-processing (as described in Section 2.2) in Figure 14. Unfortunately, due to a special observing program running during this day, and due to an emergency stop in observations as SOHO was being bombarded by SEPs, these are the only decent images available of this CME. This seriously limits the amount of information that can be gained about the CME close-in to the Sun.

As mentioned previously, the source of the CME is AR 10759, situated at latitude 12° north and longitude 54° (or 11° east of the meridian). If the CME propagates along a close-to-radial path from the AR, this can explain why the brightest parts of the CME as

Table 4 Summary table of the SOHO|CDS emission lines observed during 13 May 2005.

Transition Region Lines			
Ion	λ (Å)	log(T_e (K))	Atomic Transition
He I	584.33	4.45	$1s^2\,{}^1S_0 - 1s2p\,{}^1P_1$
O V	629.73	5.30	$1s^22s^2\,{}^1S_0 - 1s^22s2p\,{}^1P_1$
Coronal Lines			
Ion	λ (Å)	log(T_e (K))	Atomic Transition
Mg X	624.94	6.05	$1s^22s\,{}^2S_{1/2} - 1s^22p\,{}^2P_{1/2}$
Fe XVI	360.76	6.35	$2p^63s\,{}^2S_{1/2} - 2p^63p\,{}^2P_{1/2}$
Fe XIX	592.23	6.95	$2s^22p^4\,{}^3P_2 - 2s^22p^4\,{}^2D_2$

seen in the LASCO image are inclined somewhat to the north-east corona. Despite being a halo CME, it is not centred directly along the Sun – Earth direction. Most clearly seen in the C2 image of Figure 14 (left), there are two main parts to this halo CME. The first part is a leading edge which completely surrounds the Sun, resembling a skirt with nearly constant brightness at all angles, with the exception of a faint region to the south. The second part is a far brighter edge limited to the north-east sector. In the C2 image, the bright edge is distinct from the leading fainter front. In the C3 image, the bright edge has caught up with the outer edge. Other structural details of interest are the large voids leading and following the north-east bright edge, and a very complicated, tangled, small-scale structure within the main body of the CME.

It is difficult to determine a speed for such a complicated structure as this CME. The fact that only two images show the CME with any clarity does not help. Different parts of the CME seem to travel with different speeds, and the analysis is limited by the biggest problem in coronal observations, the LOS. The true 3-D extent of the CME in the inner corona cannot be determined from these two images taken from the same direction, therefore the true velocity of the CME cannot be determined accurately. By measuring the apparent speed of various structures within the CME, we can provide a safe lower limit to the CME velocity. Figure 15 shows the profile of the processed LASCO brightness at four different position angles marked on the images of Figure 14. The profiles taken along position angles 35° and 75° in the C2 image are dominated by the bright inner edge close to a height of 4 $R_\odot$. For both these profiles, there is an enhancement on the leading (largest height) part of this bright peak. This is the position of the fainter outer skirt of the CME. The other two profiles at 220° and 280° show the fainter outer skirt of the CME at a similar height of 4.5 $R_\odot$. In the LASCO C3 plot of Figure 15 (bottom plot), the bright edge in the north-east has overtaken the fainter skirt at position angle 35° and a height of 6.5 $R_\odot$. At 75°, the bright edge has nearly caught up with the outer skirt near a height of 5.7 $R_\odot$. From comparing the profiles for C2 and C3, we calculate an apparent (or POS) speed of around 840 km s^{-1} for the fainter outer skirt, and around 1000 km s^{-1} for the inner brighter front. Since we know that the CMEs are not propagating in the POS, the true speed is considerably higher. These values are also significantly lower than the CDAW CME Catalog POS speed of 1689 km s^{-1} (as also used later in this paper for velocity-profile studies).

Are the two distinct structures a single CME structure or two separate CMEs which happen to coincide in the LASCO images due to their different speeds? Lugaz *et al.* (2009) talk of CMEs which propagate at different speeds cannabilising each other in interplanetary space, and maybe the same is happening in this case – the faster, brighter CME in the north-east catches up with the slower, fainter halo CME and interacts. Jones *et al.* (2007) also dis-

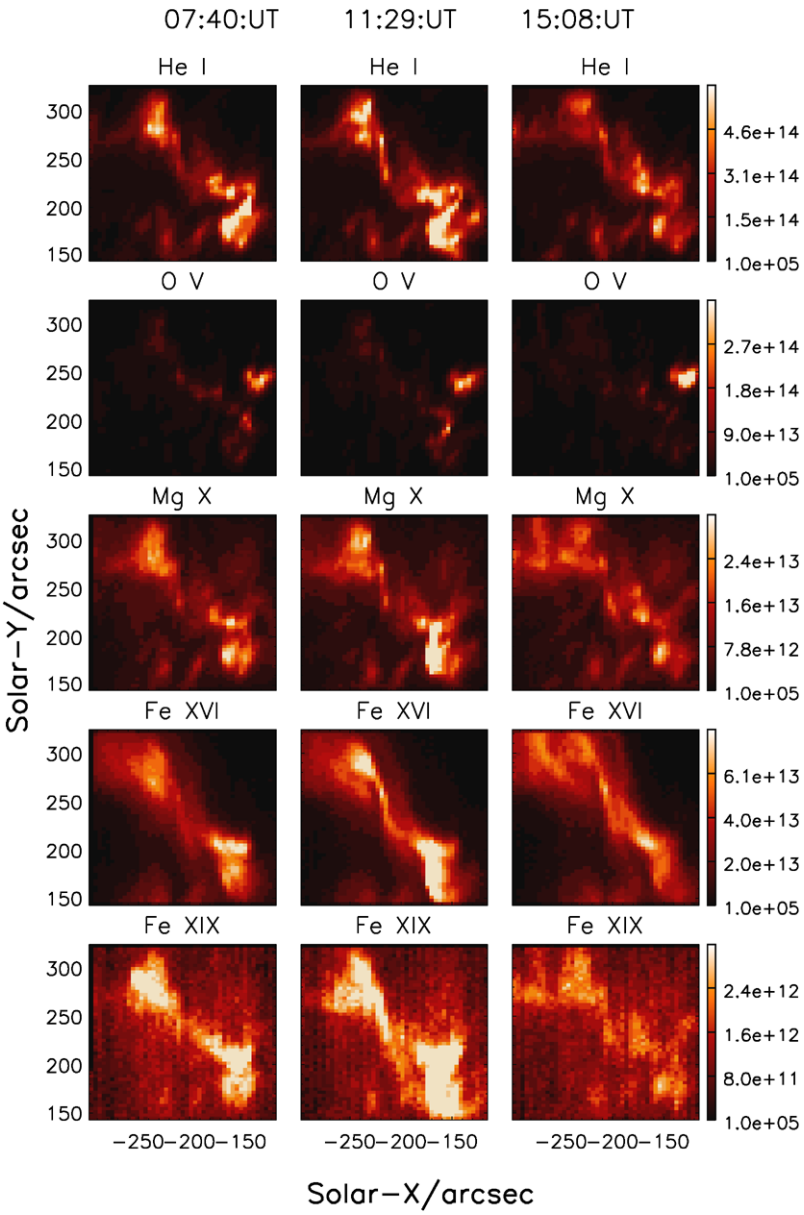

Figure 9 A sequence of 182.8 – 181.4 arc sec images of the NOAA AR 10759 taken by SOHO|CDS on 13 May 2005 before the M8.0 eruptive flare event which occurred at 16:13 UT the same day. Here, three different times have been selected: 07:40 UT, 11:29 UT, and 15:08 UT. These pre-flare EUV images exhibit a very symmetric S-shape (called sigmoid) structure related to a magnetic configuration with a high probability of eruption to produce flares and possible associated CMEs (Canfield, Hudson, and McKenzie, 1999). Such a shape is well defined in the Fe XVI and Fe XIX band images, but also clearly visible in the Mg X and He I bands; even if the emission is more intense near the footpoints, which can be better localised by the help of the O V images.

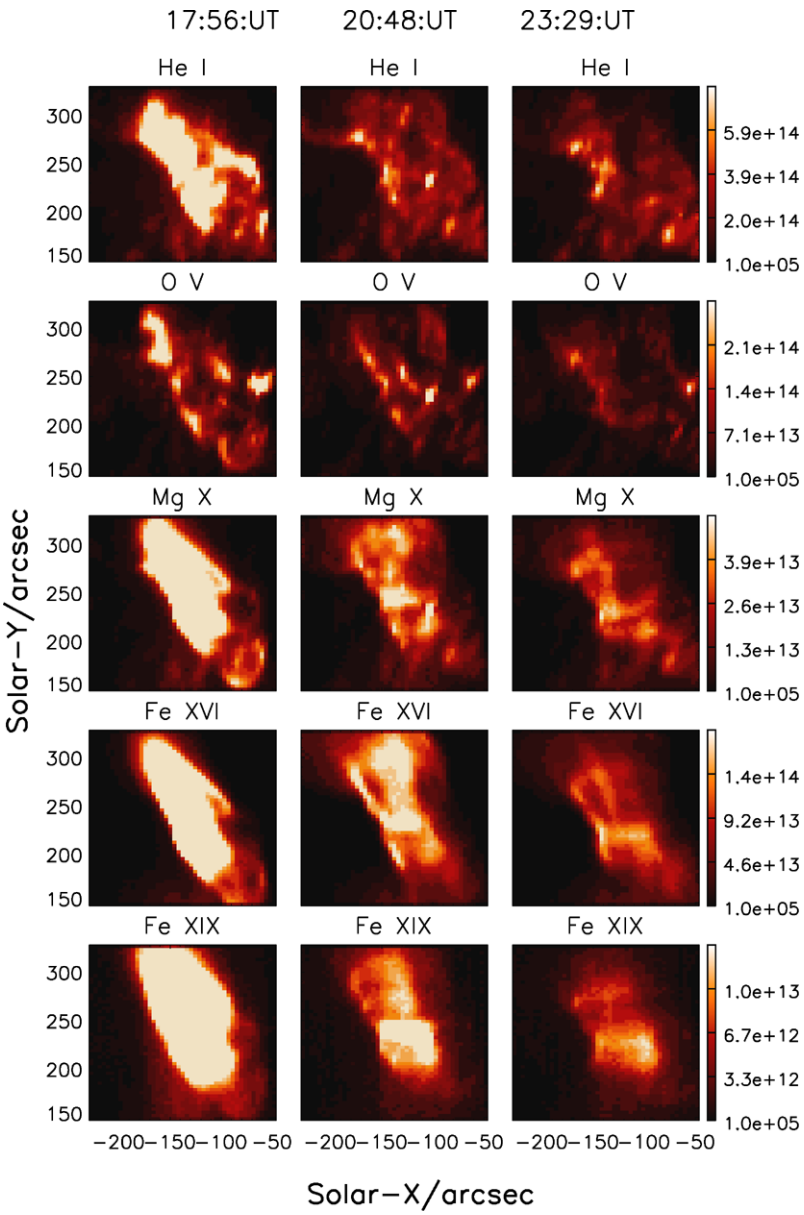

Figure 10 As in Figure 9, but at different times. Again, another three times have been selected: 17:56 UT, 20:48 UT, and 23:29 UT. These SOHO|CDS image sequences, taken following the explosive M8.0 flare event, show the evolution from the sigmoidal field (Figure 9) to loops of an arcade.

cuss this possibility of CME/ICME cannibilisation through detailed studies of CMEs/ICMEs using EISCAT observations of IPS. In support of this latter scenario is the fact that the faint outer CME seen in Figure 14 is a pure halo CME, only slightly skewed to the north-east (consistent with a CME propagating along latitude 12° north and longitude 10° east, radial from AR 10759). The second brighter CME appears only in the north-east, and is different

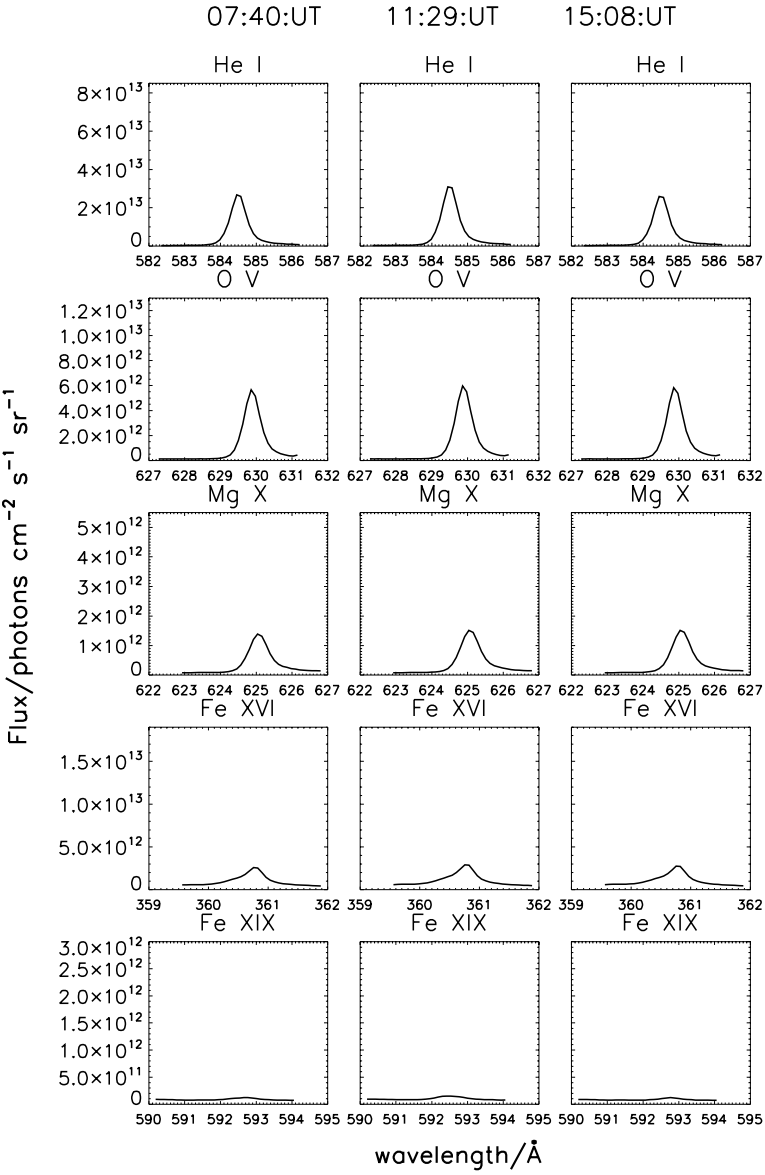

Figure 11 A sequence of averaged spectra derived from the first set of SOHO|CDS observations (see Figure 9 caption). The plots use the same y-range scaling for each line both in the first (here) and in the second set of observations (Figure 12). It more clearly shows how the line intensities change during the 13 May 2005 events. A very small increase in the 11:29 UT flux may suggest very faint and early signs of the C1.5 flare which occurred at 12:54 UT.

in appearance to a halo CME. The bright front edge extends down towards the Sun at both ends, which is inconsistent with a halo CME. AR 10759 is very dynamic throughout much of 13 May 2005; EIT was observing every 20 minutes or so in the 195 Å bandpass. Figures 16 and 17 show a series of images of the AR and surrounding area. The main "culprit" for the

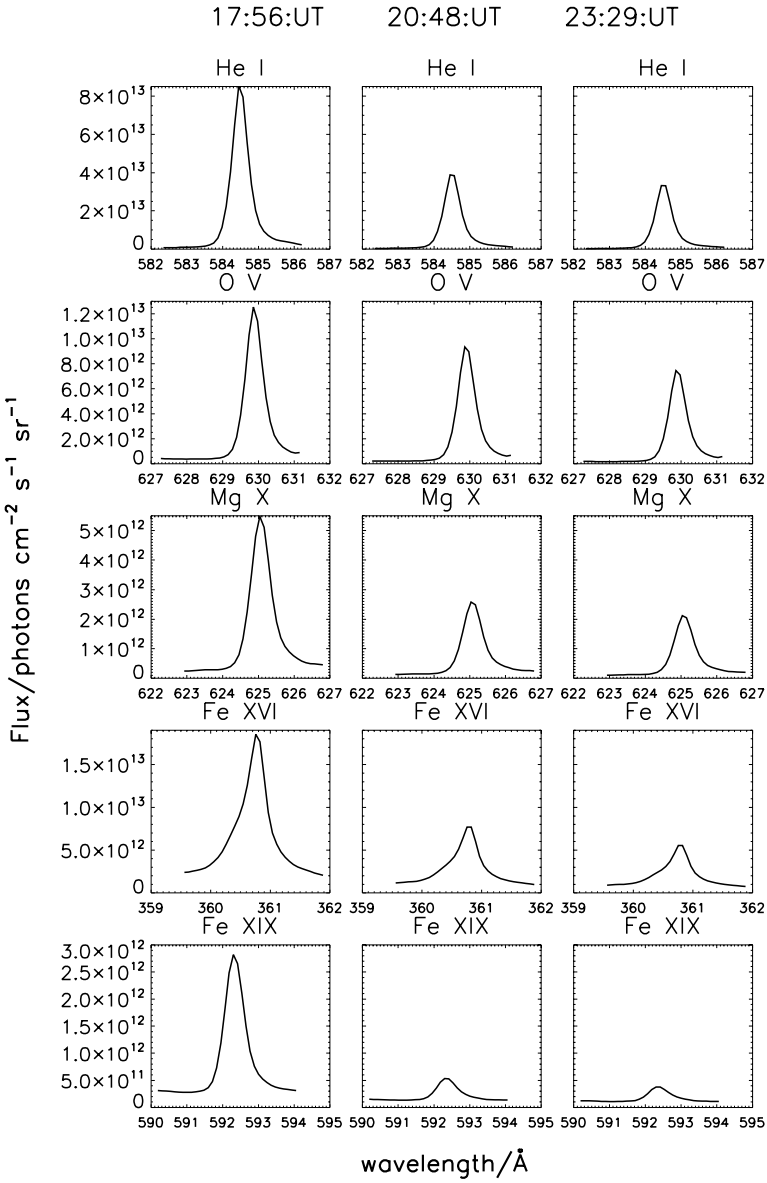

Figure 12 A sequence of averaged spectra derived from the second set of SOHO|CDS observations (see Figures 10 and 11). The big increase in the average intensity at 17:56 UT compared to the set shown in Figure 11 especially in the highly-ionised Fe XIX band, which is the signature that a huge explosive event occurred (in this case, the M8.0 flare). The post-flare phase is indicated by the intensity decay for all the wavelength bands at the subsequent times.

CME event is the activity after 16:00 UT shown in Figure 17. A bright flare dominates the AR at this time. If this event, at around 16:15 UT, results in the CME seen in LASCO C2 at 17:22 UT, the average apparent (or POS, or minimum) speed of the CME will be around 500 – 600 km s^{-1}. However, earlier in the day at 11:25 UT, the same AR ejects material.

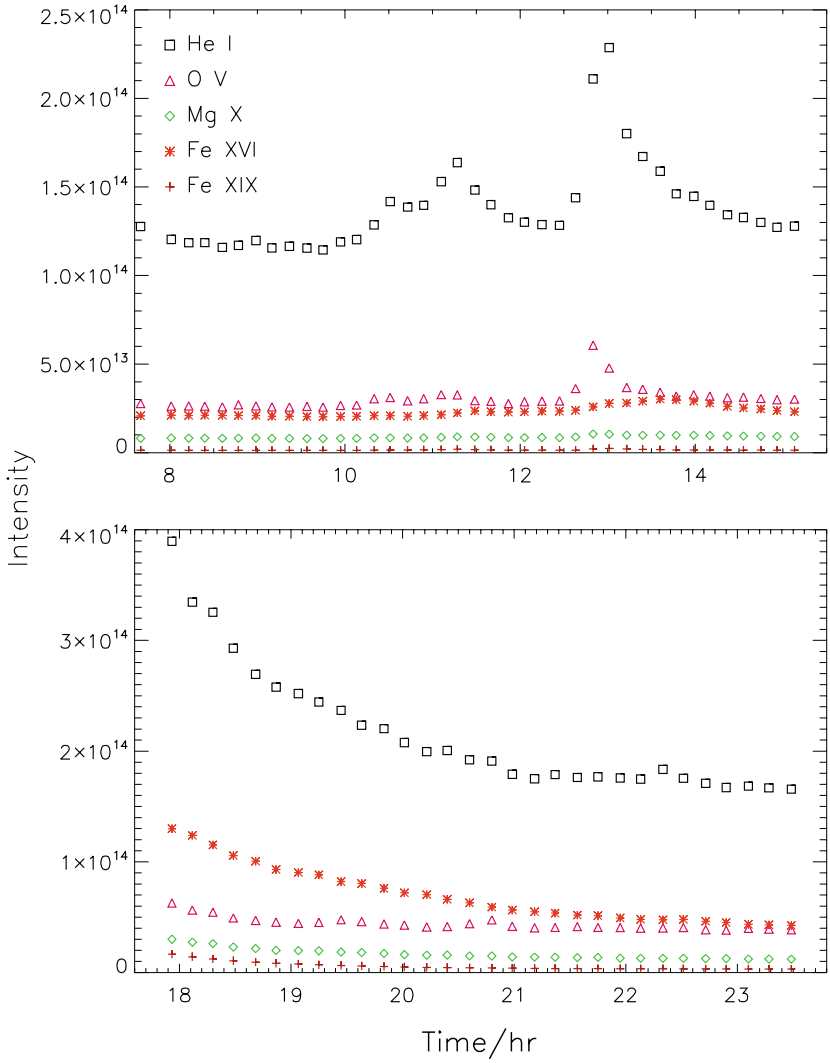

Figure 13 Intensity – time curves for the emission lines observed by SOHO|CDS (first set of observations: upper plot; second set of observations: lower plot). The intensity is in photons s^{-1} cm^{-2} sr^{-1}. The time is in hours starting from 00:00 UT on 13 May 2005. The upper plot of the earlier observations seems to show a small increase of emission for the majority of the lines, which coincides with the timing of the C1.5 flare and could be as a result of that flare around 12:54 UT.

There is no evidence of any CME activity in the LASCO data until the 17:22 UT observation. Therefore, the first eruption from the AR at 11:25 UT does not result in a CME, or the CME is narrow and is heading directly towards Earth (so is not seen past the occulting disks of LASCO). It is highly unlikely for this first eruption from the AR to have resulted in the CME activity viewed by LASCO at 17:22 UT. This does not negate the possibility that the earlier brightening is not related to the C1.5 flare however.

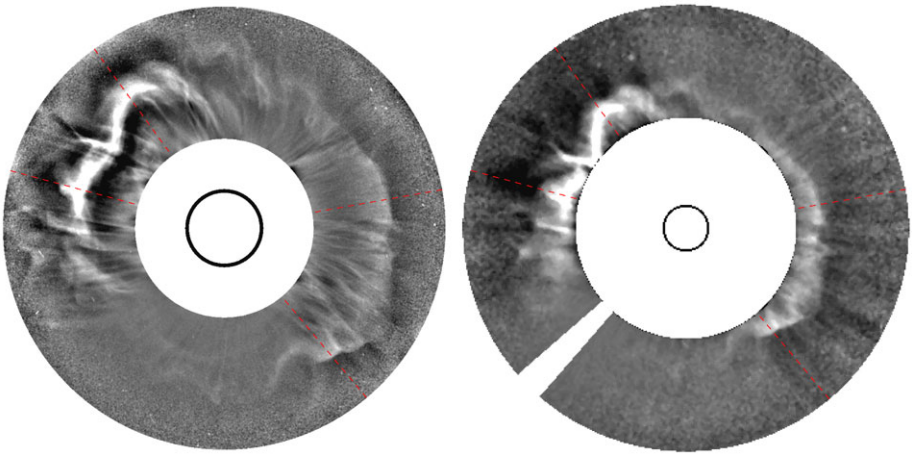

Figure 14 (Left) Post-processed LASCO C2 image of 13 May 2005 at 17:22 UT and (right) LASCO C3 image taken at 17:42 UT on the same day. The C2 field of view (FOV) shown here extends from 2.5 $R_\odot$ to 5.95 $R_\odot$, whilst the C3 FOV extends from 5 $R_\odot$ to 10 $R_\odot$. The inner black circles toward the centre of each image show the position of the Sun's limb. Processing details can be found in the text. The dashed red lines at position angles 35°, 75°, 220°, and 280° are the lines along which profiles are plotted later in Figure 15 and described in the text.

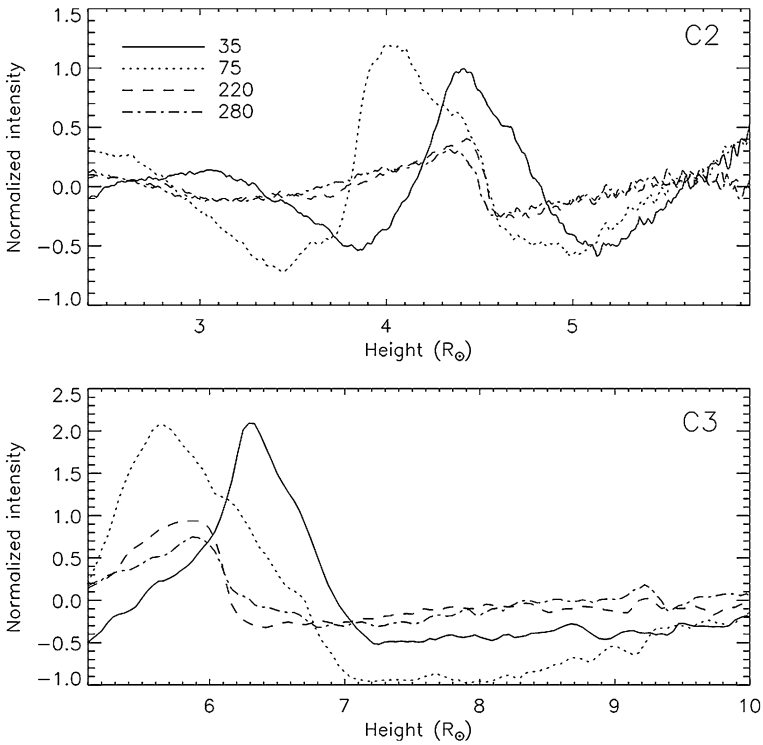

Figure 15 Profiles of normalised brightness along the dashed red lines shown in Figure 14. The top plot is for LASCO C2 at time 17:22 UT, the bottom for C3 at 17:42 UT (both on 13 May 2005). From these plots it is possible to estimate an approximate POS speed for the CME(s) as described in the text.

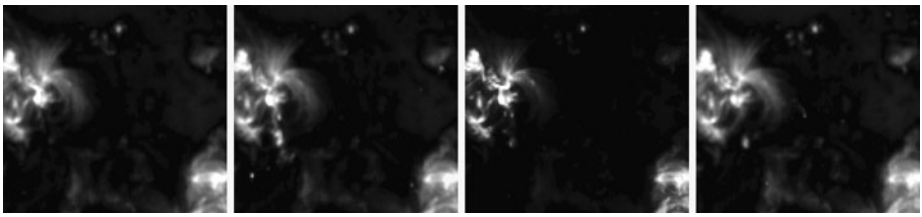

Figure 16 Four consecutive zoomed-in images of the region close to AR 10759 as observed by the EIT telescope in the 195 Å bandpass. The four observations are made at times (from left to right) of 11:05 UT, 11:25 UT, 11:42 UT, and 12:05 UT. AR 10759 sits in the top left of these images. The second image shows a tongue of material ejected out from the AR towards the bottom of the image. In the third image, there is still ejecta material apparent. The third image also shows signs of dimming. Again, signs of the earlier C1.5 flare perhaps.

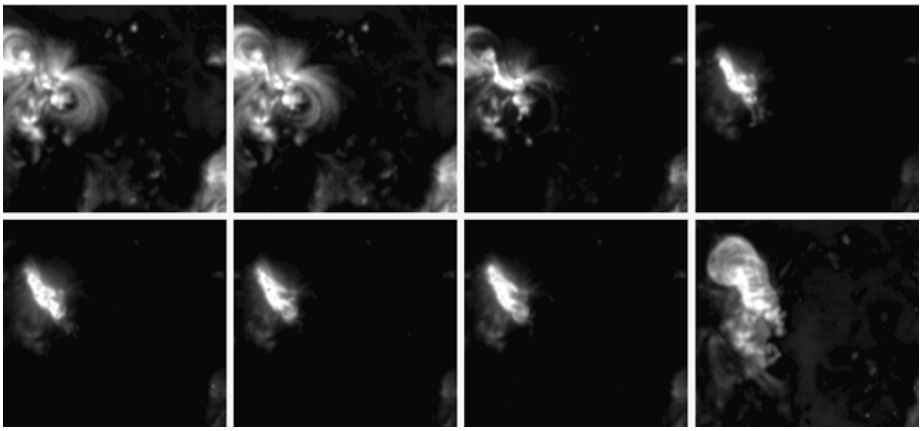

Figure 17 As with Figure 16 but for times (from left to right across the top followed by left to right across the bottom) of 16:09 UT, 16:26 UT, 16:37 UT, 16:57 UT, 17:07 UT, 17:27 UT, 17:37 UT, and 22:57 UT. A bright flare dominates the AR in the third image until the seventh. The last image at 22:57 UT shows the result of the dramatic reconfiguration of the coronal magnetic structure during this day.

3.1.1. A Brief Overview of the Sun and Corona Observations and Measurements

The post-processed LASCO coronagraph images show a halo-like structure coming toward the Earth, but with a bias to the north-east quadrant. This holds some strength to the possibility that there was a secondary eruption, which quickly merged with the first in the low corona. This is also a possible agreement with the two MCs detailed in Dasso *et al.* (2009).

With regards to the possible earlier C1.5 flare having involvement with the CME/ICME initiation, this is indeed possible (Dasso *et al.*, 2009 also touch on this). From the SOHO|CDS data, three peaks could be seen in the time series of intensities (Figure 13), especially in the oxygen-line and helium-line intensities. The first two, before 12:00 UT, with the biggest around 13:00 UT, may be peaks which tell us something about the flare – the upper plot of the earlier set of observations is a good signature of the C1.5 flare that happens at 12:54 UT. Of course, these data show clearly the latter parts of the much larger M8.0 two-ribbon flare, and this is seen in the lower time series plot of intensities in this same figure.

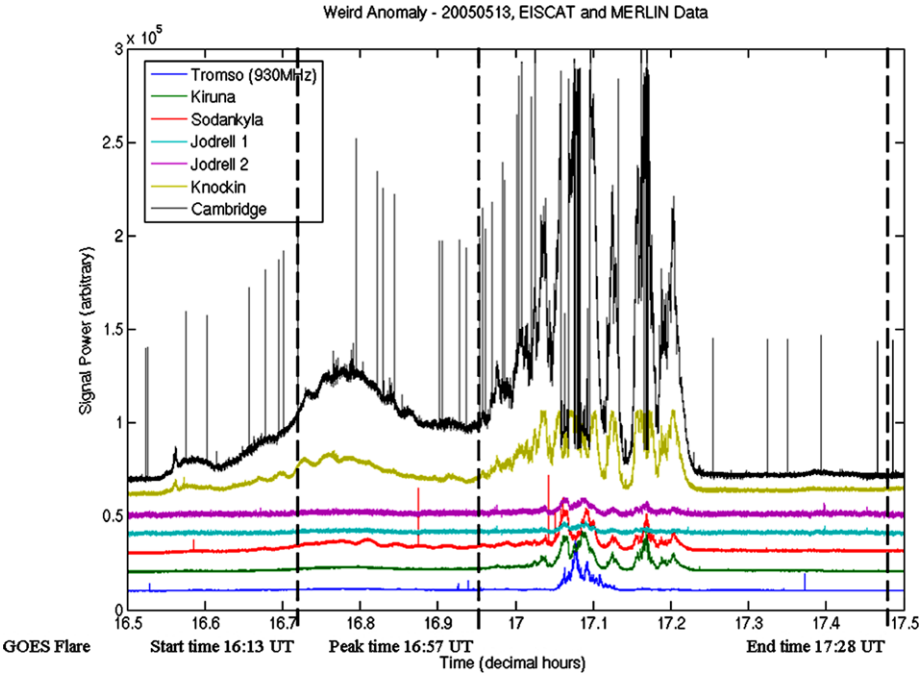

Figure 18 Observations of radio signals from EISCAT and MERLIN showing the anomalous signal-strength enhancement on 13 May 2005 due to the flare/CME and associated coronal radio burst overwhelming the IPS signal as taken from Jones *et al.* (2006). All EISCAT and MERLIN observations took place at 1420 MHz with the exception of one (as marked here in the figure).

3.2. The Inner Heliosphere

Here, we discuss the 13 – 15 May CME/ICME/MC event as the ICME and associated shock/sheath were detected and progressed through the inner heliosphere from outside of coronagraph fields of view through radio-burst tracking and observations of IPS, to near its measurement *in situ* around the Sun – Earth L_1 point.

3.2.1. Coronal Radio Bursts

The coronal radio burst associated with the 13 May 2005 flare/CME was first detected by the EISCAT and MERLIN antennas while conducting observations of IPS (Jones *et al.*, 2006) as shown in summary in Figure 18. An off-axis response created an enhancement in power received at each of the antennas. Recordings were made simultaneously with the GOES-12 satellite and the PHOENIX-2 radio spectrometer (Messmer, Benz, and Monstein, 1999) as seen in Figure 19. Also marked on Figure 18 are the start, peak, and end times of the GOES-detected flare showing very good correlation with the detections made by EISCAT and MERLIN. These are assumed to be the initial detections of the Type III radio burst as a result of the flare/CME eruption. Precise details on how this result was concluded can be found in Jones *et al.* (2006).

The direct radio observations discussed here were acquired by the *Wind* – Radio and Plasma Waves Experiment (*Wind*|WAVES) (Ogilvie and Desch, 1997; Bougeret *et al.*,

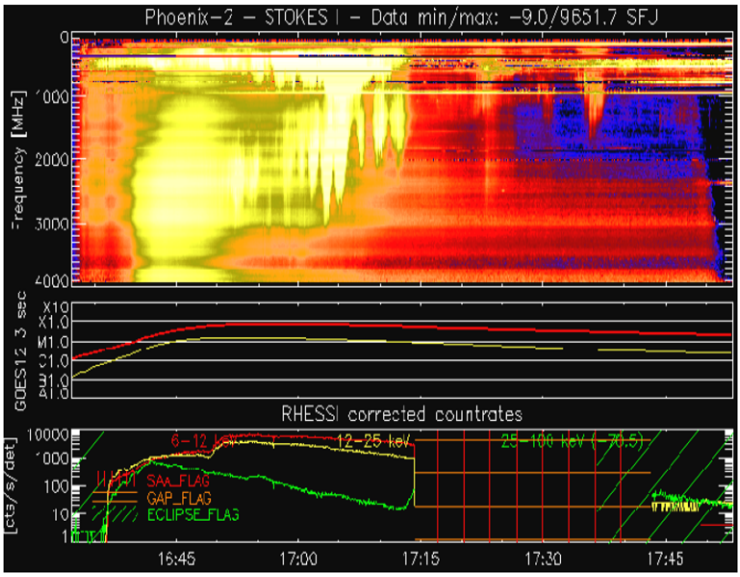

Figure 19 Figure displaying the PHOENIX-2 radio spectrogram recorded on 13 May 2005 from 16:30 UT onwards as taken from Jones *et al.* (2006). The clear onset of enhanced emission at lower frequencies from 16:35 UT can be seen in the image, which later led to a strong radio burst from 16:45 UT. The evolution from high-frequency to lower-frequency emission is a characteristic of a coronal radio burst as the resultant blast wave from the explosive event, in this case a flare/CME, moves outward from the Sun through the corona. This is explored further in the text.

1995). The *Wind*|WAVES experiment has several sensitive radio receivers: Radio Receiver Band 1 (RAD1), Radio Receiver Band 2 (RAD2), and the Thermal Noise Receiver (TNR); these cover a frequency range from 4 kHz to ~ 14 MHz. One-minute resolution data from the RAD1 receiver were analysed and a new analysis technique, using the frequency drift of DH-km-Type-II (DH-km-TII) spectra obtained by the RAD1, applied to infer, at some adequate intervals, the propagation speed of the IP shock associated with the ICME. The technique is explained in detail elsewhere (Aguilar-Rodriguez *et al.*, 2005; Gonzalez-Esparza and Aguilar-Rodriguez, 2009).

On 13 May 2005 at 17:12 UT, SOHO|LASCO observed a fast (POS $v = 1689\ \mathrm{km\,s^{-1}}$) halo CME as previously described. This CME was associated with the M8.0 soft X-ray flare. The flare region was localised close to the centre of the disk, at N12 E11. Near the Sun, a metric Type II burst was seen in radio emission detected by the *Wind*|WAVES experiment (Figure 20a) and reported as fundamental/harmonic emission by the Radio spectrometer of Astrophysikalisches Institut Potsdam, starting on 13 May 2005 at $\sim 16{:}38$ UT and ending the same day at $\sim 16{:}50$ UT, covering a frequency range of ~ 350 MHz to 40 MHz (see Figure 20b). The event was observed at $\sim 17{:}00$ UT on 13 May 2005 at 5 MHz, drifting slowly down to 40 kHz at 02:10 UT on 15 May as reported in the *Wind*|WAVES online list (http://lep694.gsfc.nasa.gov/waves/waves), maintained by M.L. Kaiser.

We began the analysis by isolating the Type II event from the RAD1 dynamic spectrum by setting to zero any emission outside the Type II burst feature. Figure 21a shows this RAD1 spectrum along with 21b showing the Type II burst isolated from the dynamic spectrum with a vertical line indicating a time cut (23:29 UT). Then each RAD1 spectrum was analysed to obtain its spectral properties. Figure 21c shows the flux density *versus* the fre-

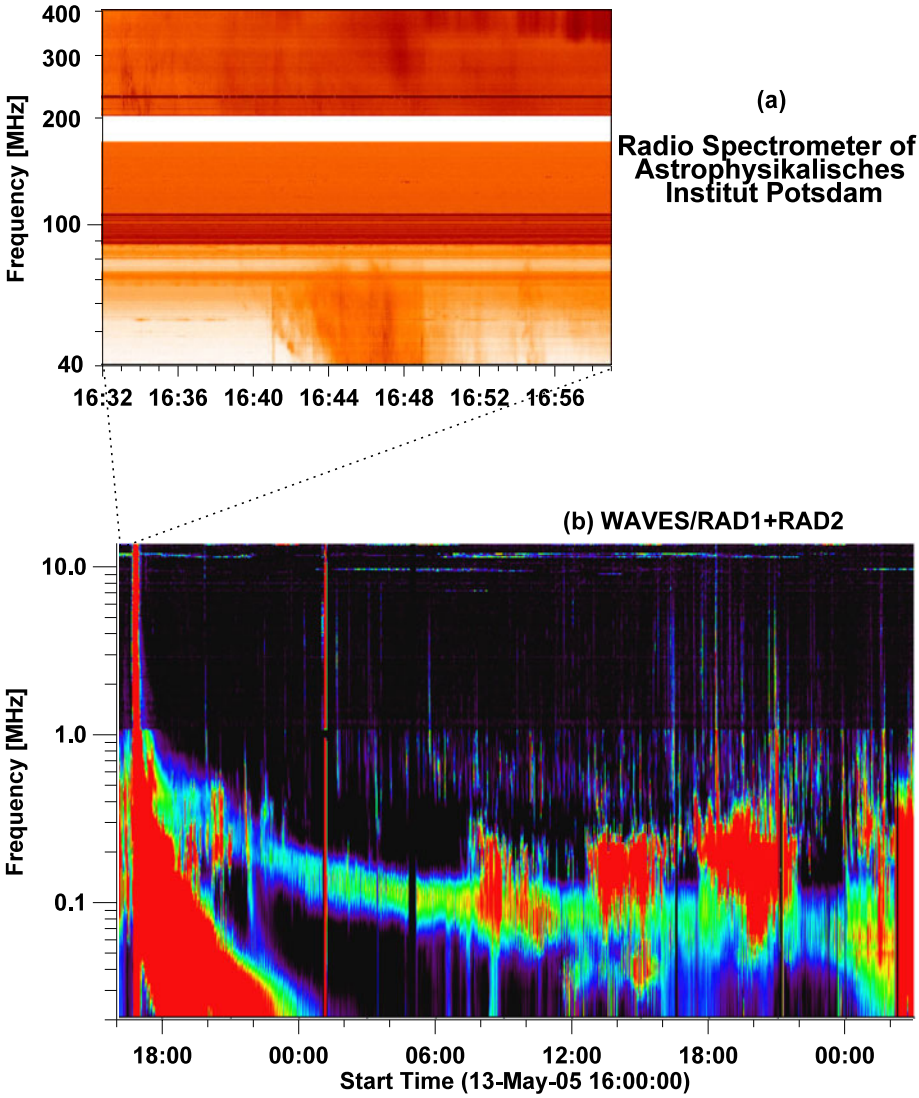

Figure 20 (a) Metric Type II radio burst observed by the Radio spectrometer of Astrophysikalisches Institut Potsdam on 13 May 2005. (b) Interplanetary counterpart of the Type II radio burst detected by the *Wind*|WAVES experiment using the RAD1+RAD2 receivers.

quency of the Type II radio burst at 23:29 UT (marked using asterisks') and a Gaussian fit to the flux-density distribution (dashed line). This Gaussian approximation to the flux-density distribution gives us, when there was a good fit, the central frequency (dashed – dotted line), which is the fundamental emission line in the radio spectrum at the given time. This procedure cleans the data from emission contamination. Once the central frequency emissions were obtained, the frequency drift associated with the DH-km-TII radio emission was studied. Figure 21d shows the central emission frequency *versus* time for the CME on 13 May 2005. The time interval is about 21 hours. Although the frequency shows a tendency to de-

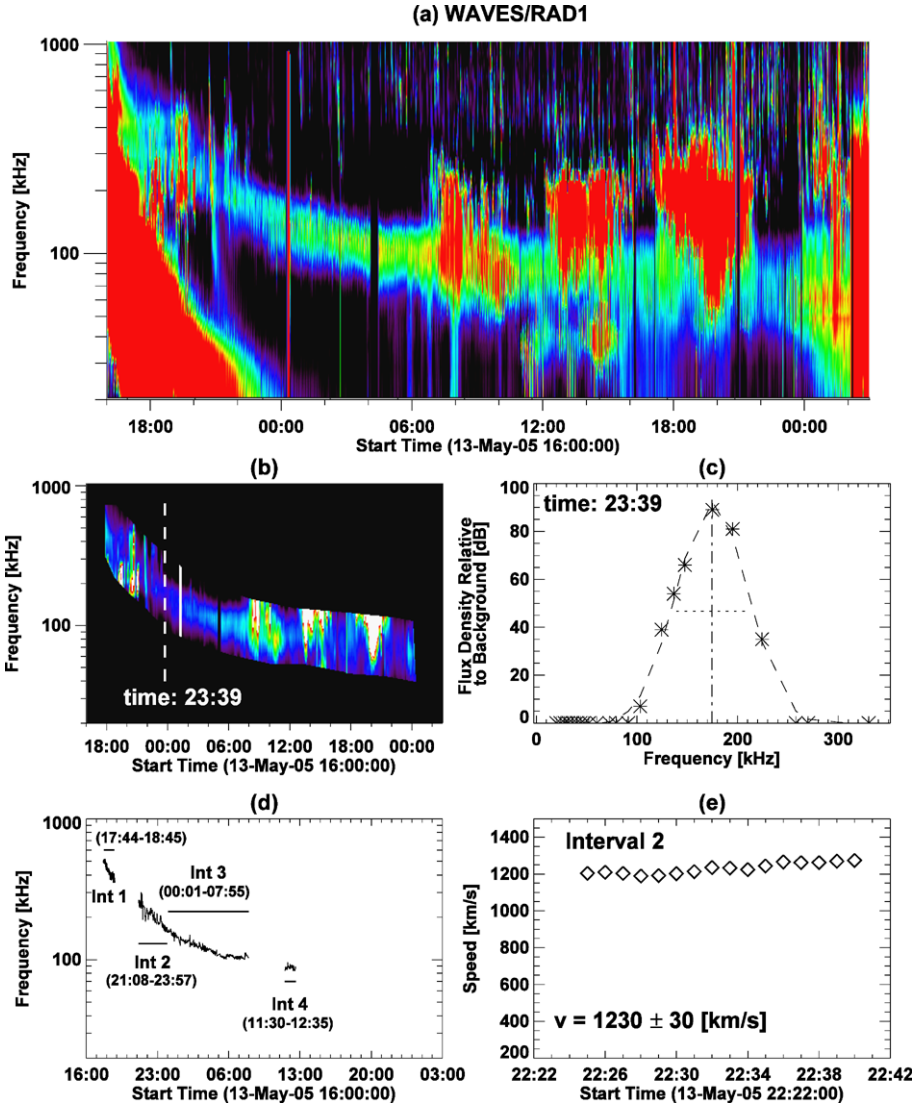

Figure 21 Central frequency drift and shock speed deduction. (a) WAVES/RAD1 dynamic spectrum associated with the propagation of the CME/shock. (b) Isolated Type II solar burst (dotted line) temporal cut to perform the central frequency analysis. (c) Flux density versus frequency for 1-min RAD1 spectrum at 23:29 UT. The Gaussian fit gives the central frequency. (d) Central frequency versus time. The horizontal lines show the four intervals to perform the Type II slope analysis. (e) Shock speed results applying the Type II slope analysis in all the sub-intervals within interval 2. The shock speed and its uncertainty are given by the mean value and the standard deviation of the distribution of speed values.

crease with time, the drift is not smooth and there are regions where the frequency increases. We selected four intervals with a well-defined drift to infer the slope of the frequency and using Equation (3) (previously described in Section 2.3), choosing a value for n_0 and if it is the F or H emission, we obtained the shock speed. The frequency slope was obtained by applying a linear fit to the central frequency points in the interval. The slope was then

Table 5 Summary table of the primary observations of IPS for the 13 – 15 May 2005 CME/ICME/MC event.

Individual observations of IPS for the 13 – 15 May 2005 CME/ICME/MC			
IPS Observing System	Source Observed	Frequency of Observation	Dates Observed
EISCAT	J0319+415	928 MHz/1420 MHz	13 – 14 May 2005
MERLIN	J0319+415	1420 MHz	13 – 14 May 2005
Ooty	J0319+415	327 MHz	14 May 2005
Ooty	J0352-071	327 MHz	14 May 2005
Ooty	J0158-141	327 MHz	15 May 2005
Ooty	J0447-220	327 MHz	15 May 2005
Pushchino	J0137+331	111 MHz	13 – 16 May 2005
Pushchino	J0043+520	111 MHz	14 – 16 May 2005
STELab	J0323+053	327 MHz	13 – 14 May 2005
STELab	J0336+322	327 MHz	13 – 14 May 2005
STELab	J0431+204	327 MHz	14 May 2005
STELab	J0534+193	327 MHz	13 – 14 May 2005

calculated for every set of 60 (90 – 120) consecutive central frequency points in the interval. This gives an ensemble of speed solutions associated with all the sub-intervals. Figure 21e shows the speed solutions for interval 2. The distribution of points shows that, in this case, the speed solutions tend to converge towards the maximum value. We define the DH-km-TII shock speed (1230 $\mathrm{km\,s^{-1}}$) as the mean of the distribution, and its associated uncertainty (30 $\mathrm{km\,s^{-1}}$) as the standard deviation of the distribution.

3.2.2. Observations of IPS

A summary of the primary individual IPS radio sources observed relating to the 13 – 15 May 2005 CME/ICME/MC can be seen in Table 5. Also shown are the IPS-observing systems that each radio source was observed along with the observing frequency, date of the observations, and also the source name in J2000 coordinates. One of the most-well-known IPS sources, as observed here by EISCAT, MERLIN, and Ooty, is that of J0319+415 (3C 84).

The individual STELab observations of IPS seen in Figure 22 show velocity sky maps across the top panels and *g*-level sky maps across the bottom. These are summaries on the sky with the Sun at the centre and angles measured outward in all directions (fisheye projections); the first marker out from the centre corresponds to 0.5 AU ($= \sin 30°$), and the second corresponds to 1 AU ($= \sin 90°$). No completely-clear signature is seen in the *g*-level values for the 13 – 15 May 2005 ICME, but there are clear enhancements in the velocity values. Several observations showed velocities over 800 $\mathrm{km\,s^{-1}}$ with marked increases in the same (or similarly-located IPS sources on the sky) observed from the 13 May 2005 through 14, some of which continued again on the 15 and 16 May. Although some *g*-level values are greater than unity (and hence suggesting increased turbulence and/or relatively increased density), none can be directly associated with the ICME. This is where the 3-D reconstruction technique can improve on this, as discussed later in this section and described in Section 2.4.

Time series of the Ooty velocity observations around this period can be seen in Figure 23. Similarly, the Ooty *g*-level observations of IPS can be seen in Figure 24 as plots on the sky displaying the regions where enhanced scintillation can be seen (otherwise known as *g*-map displays).

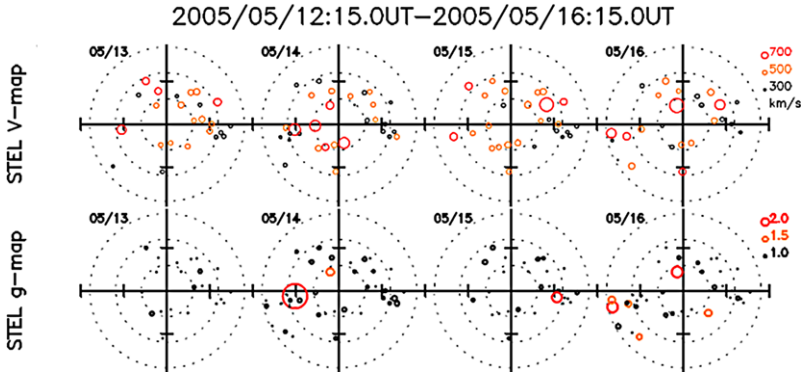

Figure 22 The STELab velocity (top) and *g*-level (bottom) results of IPS observations displayed as sky maps, as if the Sun is at the centre of each for 13 through 16 May 2005 (from left to right). There are several high-velocity values during this time, particularly around 14 – 15 May covering nearly all of the sunward sky, plus a large *g*-level increase to the East on 14 May. Although this is not conclusive evidence alone, it does suggest that a higher-velocity flow (which is possibly more highly-turbulent material) is coming toward the Earth from the Sun and may be biased in magnitude East of the Sun – Earth line. Further explanations are found in the text with regards to how these plots fit into the other supporting IPS observations of this ICME.

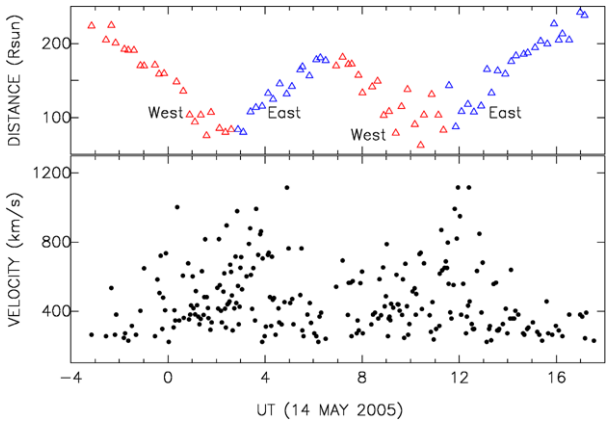

Figure 23 Ooty velocity estimates are plotted as a function of time for observations taken on 13 and 14 May 2005. The upper and lower plots are of the same data. However, in the upper plot only a 15-minute average of the P-Point distance of the observations is displayed. The west and east points shown by red and blue colour-coded triangles indicate observations that have been taken to the western and eastern sides of the Sun – Earth line respectively. As can be seen by this figure and also by Figure 24, the SOHO|LASCO halo CME's ICME is slightly oriented to the east side of the Sun. This is consistent with the STELab results and also the 3-D reconstructed STELab IPS data displayed later in Figure 29. In addition, this agrees with the earlier-discussed SOHO|LASCO post-processing analysis in Section 3.1.

At Ooty, on 14, 15, and 16 May 2005, four scans of the sky were observed per day, *i.e.* two scans to the west and two to the east of the Sun, all in a distance range of $\approx 10\ R_{\odot}$ to $250\ R_{\odot}$. Figure 23 displays velocity estimates obtained from Ooty on 13 – 14 May 2005. Each value on the lower plot indicates the IPS observation corresponding to a radio source. The P-Point distance of the LOS is plotted in the upper plot. As shown in the figure, the observations from Ooty in a day from the morning to late night (*i.e.* in the UT time range 20:00 UT on 13 May

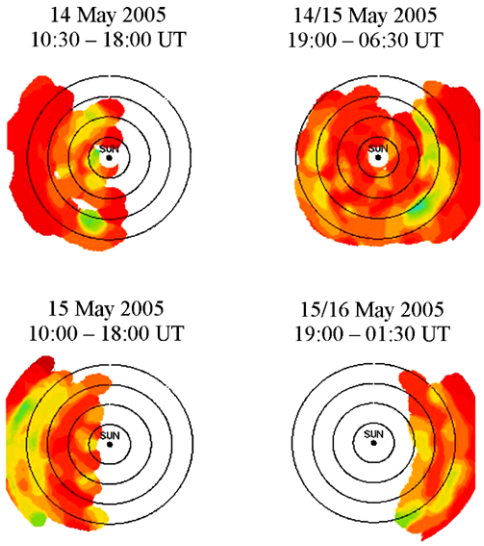

Figure 24 This figure includes *g*-maps from Ooty observations of IPS on 14, 15, and 16 May 2005 for the indicated time periods. In these "position angle – heliocentric distance" plots, the Sun is at the centre. The concentric circles are of distance of 50 $R_\odot$, 100 $R_\odot$, 150 $R_\odot$, and 200 $R_\odot$. As can be seen, the halo ICME is expanding in the east – west direction. In each plot, the time increases from west to east (refer to Figure 23). For example, in the top-left plot, the halo ICME onset can be seen at the east of Sun, in the heliocentric-distance range of 100 $R_\odot$ – 125 $R_\odot$ from north to south latitude range. In the next time-range observations (top-right plot), the ICME has moved outward as seen in the western side of the Sun at about 175 $R_\odot$. As a greater number of sources are observed from west to east of the Sun, the ICME can be seen in east of the Sun more strongly. On the same day, at later time (bottom-left plot). Now, the ICME has moved to > 200 $R_\odot$ distance range. In the last plot (bottom-right plot), the ICME goes beyond Earth's orbit.

2005 to 18:00 UT on 14 May 2005) scan the interplanetary medium twice, from west of the Sun to the east. Before the ICME onset in the IPS window, ∼ 20:00 UT on 13 May 2005, the speed range was between 300 km s^{-1} and 450 km s^{-1}; thus indicating the background solar wind speed present. When the ICME crossed the IPS FOV (IPS sources in the transition region from the west of the Sun to the east), the velocity for sources passing through the ICME increased to between 900 km s^{-1} and 1100 km s^{-1} during the time interval 01:00 UT to 04:00 UT on 14 May and in the distance range of 80 $R_\odot$ to 90 $R_\odot$. The next west – east scan (07:00 UT to 18:00 UT time range), which included different sources, also showed nearly similar conditions for the ICME crossing. The nose of the ICME is oriented to the east of the Sun and it is consistent with the CME onset seen in the SOHO|LASCO FOV. On the next day, ∼ 06:00 UT on 15 May 2005 (see Figure 24), the ICME moved to ∼ 150 $R_\odot$ and in this distance range, the velocity dropped to between around 800 km s^{-1} and 1000 km s^{-1}. On 16 May 2005, the ICME had crossed the IPS FOV and the velocity estimates went back to the background solar-wind values of around 300 km s^{-1} to 500 km s^{-1}.

Figure 24 shows the *g*-maps of different IPS fields of view between 14 and 16 May 2005. In these "PA – Distance" images on 14 May 2005, the onset of the ICME can be seen in the heliocentric-distance range of about 100 $R_\odot$ to 125 $R_\odot$. The halo shape of the ICME can be clearly seen in the west – east direction of the Sun around 150 $R_\odot$ on the image for the time interval of between 19:00 UT and 06:30 UT on 14 – 15 May 2005. In the next consecutive image, 10:00 UT to 18:00 UT on 15 May 2005, the ICME has propagated to a heliocentric

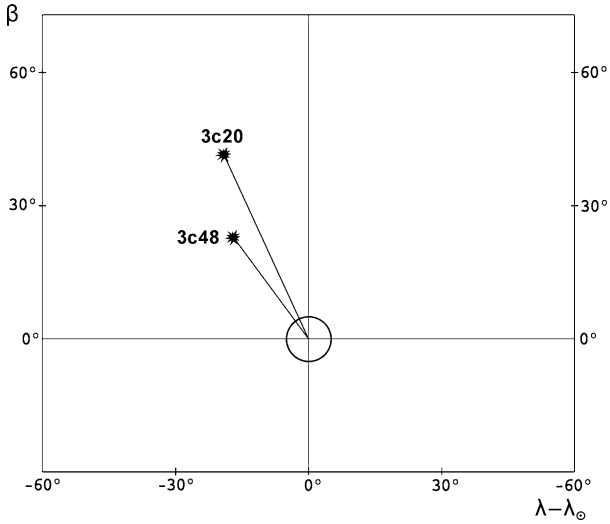

Figure 25 Positions of the J0137+331 (3C 48) and J0043+520 (3C 20) radio sources in ecliptic coordinates as observed by the Pushchino Radio Astronomy Observatory.

distance of $\sim 200\,R_\odot$ and is more dominant to the east. In the last scan, the ICME has already moved out of the Earth's orbit and beyond the Ooty IPS FOV.

The Pushchino Radio Astronomy Observatory was used at the frequency of 111 MHz and a sampling rate of 0.1 s with a frequency bandwidth of 600 kHz for IPS observations of several distant radio sources during May 2005. The most-interesting data obtained were for two of these observed sources: J0137+331 (3C 48, B0134+329, CTA 15) and J0043+520 (3C 20, B0040+517, CTB 6). The ecliptic coordinates of the sources are equal to $\lambda_{48} = 36°$, $\beta_{48} = 23°$, $\lambda_{20} = 34°$, and $\beta_{20} = 43°$ for J0137+331 and J0043+520, respectively. The longitude of the Sun on 14 May 2005 was $\lambda_0 = 53°$, correspondingly $\lambda_{20} - \lambda_0 = 17°$, $\lambda_{48} - \lambda_0 = 19°$. The locations of the sources relative to the Sun are shown in Figure 25. One can see that two observations were sampling the solar wind plasma in close proximity. However, due to the strong difference in angular sizes of the sources, the IPS signals are sensitive to plasma turbulence at different regions of the solar wind. The radio source J0137+331 having angular size about 0.1 arc sec at this frequency, can be considered as a "point source". The region of effective radio-wave intensity modulation on the LOS to this source is defined by the inequality in quiet conditions:

$$0.6\ \text{AU} = 1\ \text{AU}(\cos\varepsilon_{48} - 0.6\sin\varepsilon_{48}) < z < 1\ \text{AU}(\cos\varepsilon_{48} + 0.6\sin\varepsilon_{48}) = 1.2\ \text{AU}. \quad (7)$$

Here, z is the distance from the observer to the irregularities, $\varepsilon_{48} \approx 25°$ is the source elongation angle on 14 May 2005, the LOS P-Point was located at the heliocentric distance of around 0.4 AU, and lower and upper slab boundaries correspond to the 1/2 turbulence level in comparison with that of the P-Point. Radio source J0043+520 is extended; its angular size is several arc sec. Large angular size results in suppression of the contribution from the distant region and approaching the effective region to the observer. The effectively modulating region of the turbulent plasma is bounded in quiet conditions by

$$0 < z < 1\ \text{AU}\cos\varepsilon_{20} \approx 0.7\ \text{AU}. \quad (8)$$

Here, $\varepsilon_{20} \approx 45°$ is the elongation angle on 14 May, and the LOS P-Point is located at heliocentric distance of about 0.7 AU. The geometry of the IPS experiment at 111 MHz in the heliocentric coordinate system can be seen in Figure 26.

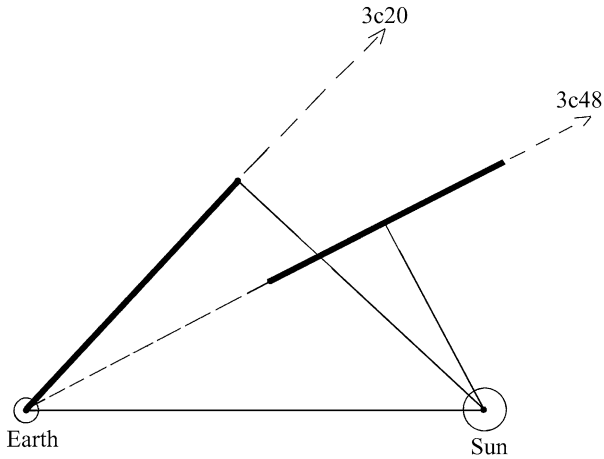

Figure 26 Geometry of lines of sight from the observations of IPS of radio sources J0137+331 (3C 48) and J0043+520 (3C 20) by the Pushchino Radio Astronomy Observatory. Effectively modulating regions are marked by the solid thicker portions of each LOS.

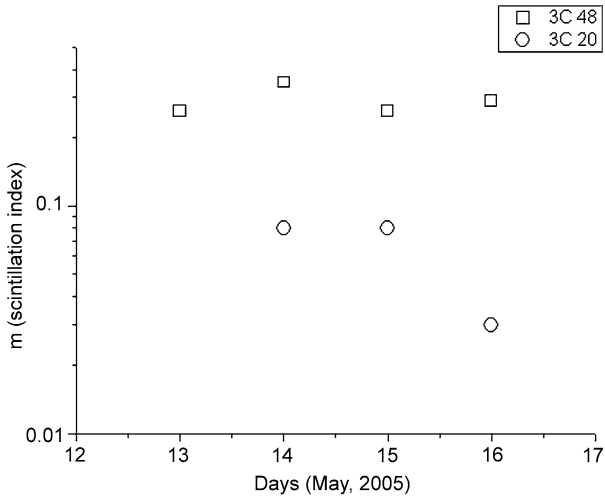

Figure 27 Daily scintillation indices for the two IPS sources J0137+331 (3C 48) and J0043+520 (3C 20) observed by the Pushchino Radio Astronomy Observatory.

Calculated values of scintillation indices for source J0137+331 (3C 48) – root mean square (rms) source flux fluctuations normalised to the mean flux – are shown in Figure 27 in logarithmic scale. A weak increase of about 1.5 times in scintillation index was observed on 14 May for source J0137+331. Corresponding temporal scintillation spectra are presented on the left-hand side of Figure 28. It follows from the comparison of the three spectra that no significant variations of the spectrum width, and correspondingly, of the moving scintillation pattern speed were observed. The source J0137+331 observed at 12:20 UT on 14 May was nearly at closest approach to the Sun, its LOS P-Point was projected to the north solar hemisphere at latitude of about 50° and at nearly 60° to the east from central meridian. Weak IPS increase for this source shows that a disturbance passed through the LOS at the very periphery of the effective slab, marked in Figure 26, or even closer to the Earth. This is similar to the EISCAT – MERLIN observations of J0319+415. Absence of a distinct increase in the plasma velocity is explained by the projection effect, because only transversal to the LOS component of the velocity produces the IPS pattern motion. Using

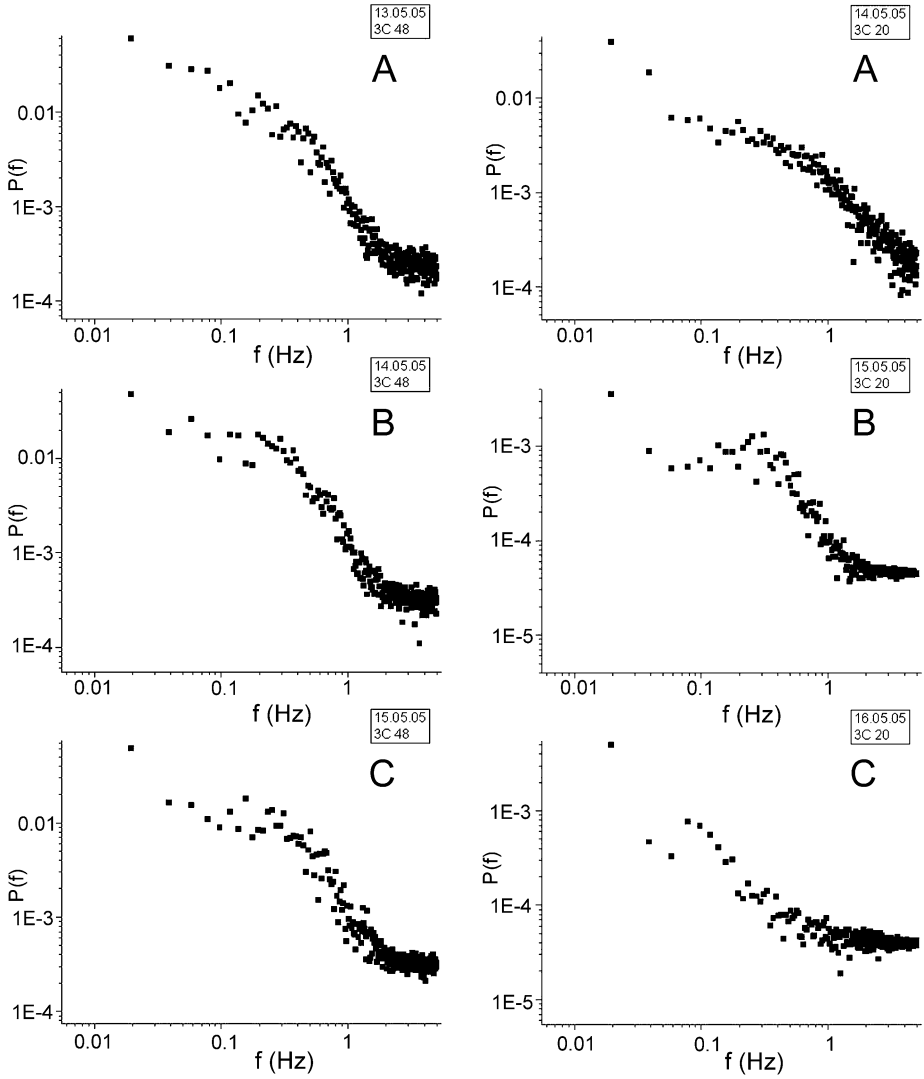

Figure 28 Temporal IPS power spectra of the source J0137+331 (3C 48 – left) and J0043+520 (3C 20 – right) as observed using the Pushchino Radio Astronomy Observatory.

the time delay between the event in the corona and the J0137+331 IPS observation, one can obtain only the lower estimate of the mean ICME speed $\approx 800\ \mathrm{km\,s^{-1}}$.

In quiet conditions for source J0043+520 (3C 20), the IPS response is usually weakly scintillating with a scintillation index typically around 0.03. Figure 27 shows that strong, about three times that, enhancements of IPS caused by the 13 May 2005 CME were observed for the source J0043+520 on 14 and 15 May 2005. This source is sensitive to large-scale disturbances in the sector of heliographic longitudes of 0° to 45° to the east from central meridian. The value of scintillation index on 16 May again corresponds back to a quiet IPS signal. Temporal IPS power spectra of J0043+520 are presented in the right-hand panels of Figure 28.

The weak IPS increase for J0137+331 and considerable increase for J0043+520 in the geometry of the presented observations (Figure 26) allows us to draw the conclusion that the ICME disturbance in the eastern part of the northern hemisphere was strong only within the angle about 50°. The IPS spectrum on 16 May 2005 is typical for the big source with angular size about 3 – 5 arc sec in quiet solar-wind conditions (Shishov and Shishova, 1979). A combination of radial dependence of turbulence power and the source-size truncating effect, results in the same scintillation spectra as scintillations on a statistically quasi-uniform extended slab adjacent to the observer (Shishov and Shishova, 1979). Temporal IPS spectrum on 14 May is qualitatively similar to that on 16 May, but has about 10 times increased integral power and has shifted to higher scintillation frequencies. Frequency shift corresponds to a three times increase in the local plasma speed. The temporal scintillation power spectrum measured on 15 May (as in Figure 28) is similar to the spectrum of a point source and differs strongly from the spectra on 14 and 16 May, especially in the steep high-frequency region for source J0043+520. Such a spectrum of an extended source, as well as scintillation index increase and typical scintillation time decrease, are explained by a narrow slab with enhanced turbulence located within the distance 0.2 AU from the observer. Local plasma velocity was approximately the same as in undisturbed conditions. The approaching of the effective slab to the Earth results in reduction of the source-size influence on the scintillation parameters and their similarity to the parameters of a point source. IPS data for the source J0043+520, observed on 14 May at 13:20 UT, show that the ICME front passed the distance more or about 0.7 AU for 21 hours with the mean speed $\approx 1300\ \mathrm{km\,s^{-1}}$. The same value of the local plasma speed is needed for explanation of three times typical IPS time decrease by the passing ICME. Near the Earth, a slab with enhanced turbulence on 15 May at 13:20 UT is associated evidently with the tail part of ICME because the front part has already reached the Earth at around 03:00 UT resulting in the large geomagnetic storm. Time delay of about 13.5 hours between J0043+520 on 14 May 2005 and the event in the Earth magnetosphere corresponds to the mean ICME speed $\approx 900\ \mathrm{km\,s^{-1}}$ between 0.7 AU and 1 AU heliocentric distances, showing that the ICME decelerated inside 1 AU. These are in agreement with the other IPS results and those discussed in Section 3.2.1 on the radio-burst propagation, and more strongly show that the ICME was perhaps more biased in the north-east quadrant.

Next we look at the EISCAT – MERLIN cross-correlated observations of IPS source J0319+415 (3C 84) in the context of the 3-D tomographic reconstruction of the inner heliosphere from the STELab IPS data, before moving on to looking at the reconstruction itself in greater detail. Figure 29 shows the 3-D reconstructed ICME on 14 May 2005 at 03:00 UT using the methods described in Section 2.4 and taken from Breen *et al.* (2008). The fast solar wind to the north of the ICME received a strong perturbation non-radially northward in the meridional direction due to the interplanetary transit of the 13 – 15 May 2005 ICME (Bisi, 2006; Breen *et al.*, 2008). Non-radial flows of, and possibly due to CMEs/ICMEs, have also been noted by Owens and Cargill (2004) through other methods. In Figure 29, the 3-D reconstructed density structure from the STELab observations (during CR2028-CR2030) on 14 May 2005 at 03:00 UT can be seen along with the EISCAT – MERLIN ELB IPS LOS ray path passing through the reconstructed volume. The LOS is immersed in three different structures in the heliosphere from very near the Earth (equatorial intermediate/fast solar wind) through towards the P-Point (the ICME itself) and passed the P-Point out to around 2 AU from Earth (the polar fast solar wind stream). It is the latter of the three that dominate this observation of IPS with the ICME only producing a small contribution to the received scintillation pattern at the EISCAT and MERLIN receivers on 14 May 2005 (as described in greater detail in Breen *et al.*, 2008). The fast polar wind stream is also nearest to, and intersecting the largest portion around (particularly on the source end), the LOS P-Point, which

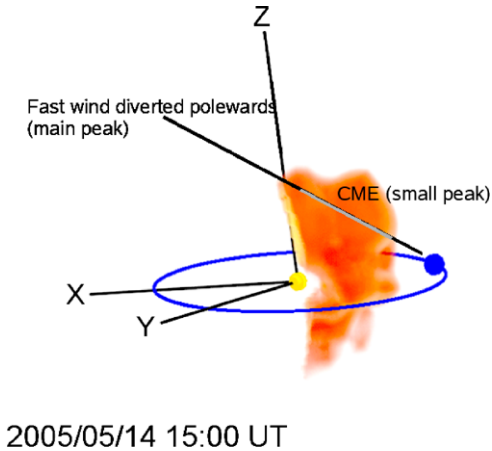

Figure 29 3-D reconstruction of the distribution of reconstructed solar-wind density upwards of 8 e^{-} cm^{-3} (brighter colours toward yellow mean increasing density) at 15:00 UT on 14 May 2005 as derived from STElab IPS data. All non-ICME-related features have been removed for clarity of viewing when displaying the 3-D volume. The axes are heliographic coordinates with X-axis direction pointing toward the vernal equinox, and Z-axis directed toward solar heliographic north. An r^{-2} density fall-off has been removed from the analysis to better-show structures further out from the Sun, which in this image, is represented by the central yellow/orange sphere and the Earth by the blue sphere (not to scale). The EISCAT – MERLIN IPS LOS ray path observation of J0319+415 (3C 84) on 14 May 2005 is shown as a line going from the Earth towards the upper-left section on the image. This is cutting through the reconstructed Earth-directed 13 – 15 May 2005 ICME. The density structures intersecting and crossing the IPS LOS, which the three-mode weak-scattering model fit suggests, are associated with the main, second, and third peaks in the observed CCFs (as described in the text), and are marked as "fast wind diverted polewards (main peak)", second peak is unlabelled but is caused by the solar wind at the Earth end of the LOS nearest the ecliptic, and "CME (small peak)" respectively. Further details on the EISCAT – MERLIN fit can be found in the text along with the relevant references. Adapted from Breen *et al.* (2008), reproduced by permission of the American Astronomical Society (AAS).

is where the greatest amount of scintillation power is created (see, *e.g.*, Fallows, 2001). It is also this stream which is highly perturbed meridionally northward by $\sim 8° - 15°$ because of the passage of the ICME.

The EISCAT – MERLIN velocities were obtained from the observations of J0319+415 on 13 and 14 May 2005. This source is a relatively-high-latitude source to the east of the Sun – Earth line (where the CME/ICME appears to dominate both in the SOHO|LASCO images, in the 3-D reconstructed results from the STELab IPS data, and in the other observations of IPS already described).

The EISCAT – MERLIN observations on 13 May 2005 showed a clear fast-wind velocity up until 16:20 UT – 16:30 UT, when strong radio interference (interpreted by Jones *et al.*, 2006 as a coronal noise burst, detected in the side-lobe response of the telescopes as mentioned briefly and shown in Section 3.2.1) swamped the IPS signal. For the usable observations (13:15 UT – 16:20 UT), the P-Point lay 84 $R_{\odot}$ off the east limb of the Sun, at a heliographic latitude of 57° north. When the observations of IPS from before 16:20 UT on 13 May 2005 were fitted using a three-mode weak-scattering model using boundaries between different regions of flow determined from the 3-D density STELab tomographic reconstruction (as previously mentioned), they were found to be dominated by fast wind with an outflow speed of 753 km s^{-1}. The precise error bound for this speed is hard to quantify in the current three-mode model, but it lies in the region of ± 20 km s^{-1}. The slow-wind contribution to

the observation was small, and no attempt was made to fit a slow-wind speed (an outflow speed of 350 km s^{-1} was assumed when fitting for fast-wind speed). Skew in the CCF peak suggested the presence of slower fast-wind outflow near the slow-wind boundary layer (see, *e.g.*, Bisi *et al.*, 2007a) and fitting indicated an outflow speed of 650 ± 50 km s^{-1} for this mid-latitude component of the solar wind. J0319+415 was again observed by EISCAT and MERLIN on 14 May 2005 from 14:00 UT, when the P-Point lay 84 $R_{\odot}$ off the east limb of the Sun at a latitude of 58° north. For the first five minutes of the observation, the results were very similar to those from the previous day: a fast-wind speed of 760 km s^{-1} for the main fast stream and ~ 650 km s^{-1} for the low-latitude fast wind near the slow-wind boundary. Owing to the short integration time, error bounds were larger than the previous day, being of the order of ± 35 km s^{-1} for the main fast stream and ± 75 km s^{-1} for the low-latitude fast wind. From 14:05 UT to 14:10 UT, the form of the CCFs changed abruptly, with the emergence of a third peak at shorter time lags. Considerable temporal evolution of the CCFs was obvious, although it is difficult to determine how much of this is temporal change in solar wind parameters and how much is a result of the geometry of the observation changing with time, maximising sensitivity to outflow at slightly different meridional angles (Moran *et al.*, 1998; Bisi, 2006; Breen *et al.*, 2008).

The sudden change in the form of the CCFs and spectra indicated the onset of a transient event in the solar wind, while the appearance of a bay of negative correlation flanking the peak of maximum cross correlation between the scintillation patterns suggested field rotation (Klinglesmith, Grall, and Coles, 1996; Canals, 2002; Jones, 2007). Jones *et al.* (2007) showed that the time of appearance of this transient was consistent with it being an interplanetary extension of the CME seen in SOHO|LASCO on the previous day. When the observations were fitted again, by Breen *et al.* (2008), the results showed that the main peak of the CCF corresponded to fast wind near the boundary layer of the ICME, deflected polewards by $\sim 8° - 15°$, and with an outflow speed of 719 km s^{-1}. This was also consistent with preliminary off-radial findings by Bisi (2006) for the general structures at the time. The low-latitude fast wind appeared as a distinct peak at longer lags, with an outflow speed of ~ 650 km s^{-1}, while the "new" small peak at shorter lags corresponded to the ICME and had an outflow speed of 1075 km s^{-1} (Breen *et al.*, 2008). Error bounds are of the order of ± 15 km s^{-1} for the deflected fast stream, ± 40 km s^{-1} for the low-latitude fast stream, and ± 100 km s^{-1} for the ICME. The relatively-small contribution made by the ICME to the observed scintillation pattern is a result of much of the structure lying relatively near to the Earth in the LOS (as mentioned previously and seen on close inspection in Figure 29). As a result, not all the phase scintillations introduced by refraction by small-scale irregularities within the ICME had been converted to amplitude scintillation by the time the signal reached the telescopes.

Figure 30 shows the mass determination (left panels) using the STELab IPS density-reconstruction results along with the reconstructed-velocity structure surrounding the mass (right panels) at each of the times shown. As in Figure 29, all non-ICME associated features have been removed. The dates and times showing the propagation of the ICME through the interplanetary medium from near the Sun to around 1 AU are (top, going downward) 14 May 2005 at 03:00 UT and 15:00 UT (interpolated), and 15 May 2005 at 03:00 UT and 15:00 UT (interpolated). The excess mass above an assumed background of 5 cm^{-3} obtained from each of the four times during the ICME propagation are approximately constant, varying little, with an excess mass of the ICME of around 6.4×10^{15} g, an energy fluctuating between 2.9×10^{31} erg and 4.7×10^{31} erg, encompassing a volume increasing from 0.045 AU^3 to 0.204 AU^3 throughout the period of interest as shown. The excess mass obtained here is somewhat consistent with the modelled (assumed) values used by Lara and Borgazzi (2009)

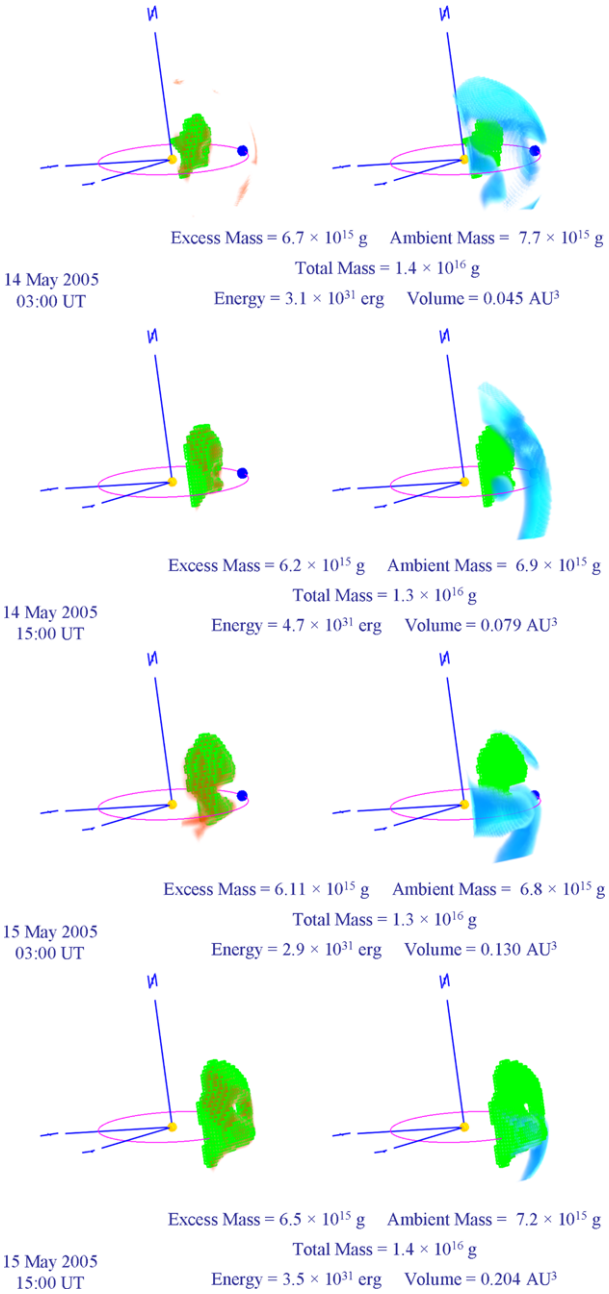

Figure 30 As in Figure 29 for the most part, but this time showing the developing and changing reconstructed structure of the 13 – 15 May 2005 ICME as it makes its way to the Earth at the times shown. The left-hand images are those of density but highlighted with cubes to encompass the reconstructed volume of the mass portion of the ICME. This same highlighted volume is shown on the right-hand side displaying the reconstructed portions of very high velocity around the denser ICME. Each image is labelled with the corresponding date and time as reconstructed along with the masses, volume, and energy values in each.

in their attempts to model using hydrodynamic theory the ICME transport with associated Type II bursts. Their assumed value for a typical CME, and used for this event, is $\sim 10^{16}$ g: around 50% more than we compute here.

An overall summary of observations of IPS from the IPS-capable systems discussed here can be seen in Table 6. Here, the separated portions of the EISCAT – MERLIN (E – M) LOS

Table 6 Summary results table of observations (Obs.) of IPS for the 13 – 15 May 2005 CME/ICME/MC event. A "–" value means this is either not possible to be measured or currently not available. Velocity values stated are the radial components of velocity as measured by each IPS system. EISCAT – MERLIN observations are shortened to "E – M".

IPS Results Summary Organised by Date/Time								
IPS Obs. System(s)	Source Observed	Date of Obs.	Time of Obs. (UT)	Feature – Sun Dist. ($R_\odot$)	Rad. Vel. (km s^{-1})	Rad. Vel. Err. (km s^{-1})	*g*-level Value	Off-Rad.° (poleward)
STELab	J0323+053	13 May 2005	02:49	≈ 48	500	± 28	0.978	–
	J0336+322		02:58	54	564	± 71	0.903	–
	J0534+193		04:45	115	940	± 92	–	–
Pushchino	J0137+331		12:20	≈ 86	> 800 (fast wind)	–	≈ 1.0	–
E – M	J0319+415		15:00 – 18:00	84 – 119	753 (fast wind)	± 20	–	0°
Ooty		14 May 2005	11:00	≈ 120	750	–	–	–
	J0352-071		11:16	97	870	–	–	–
STELab	J0323+053		02:42	≈ 50	1086	± 192	1.30	–
	J0336+322		02:54	≈ 52	810	± 48	1.95	–
	J0431+204		03:38	≈ 60	1093	± 20	1.23	–
	J0534+193		04:42	≈ 112	1161	± 54	5.24	–
Pushchino	J0137+331		12:20	≈ 86	> 800	–	≈ 1.3	–
	J0043+520		13:20	≈ 151	≥ 1300	–	≈ 2.5	–
E – M	J0319+415		Before 14:10	83 – 129	760 (fast wind)	± 35	–	∼ 0°
			After 14:10	83 – 129	719 (non-radial fast wind)	± 15	–	∼ 8° – 15°
				88 – 166	1075 (ICME)	± 100	–	∼0°
Ooty	J0158-141	15 May 2005	01:14	137	949	–	–	–
	J0447-220		04:03	153	910	–	–	–
Pushchino	J0137+331		12:30	≈ 86	≈ 700 (fast wind)	–	≈ 1.3	–
	J0043+520		13:30	≈ 170	≈ 400 (slow wind)	–	≈ 2.5	–
	J0137+331	16 May 2005	12:30	≈ 86	–	–	≈ 1.0	–
	J0043+520		13:30	≈ 150	–	–	≈ 1.0	–

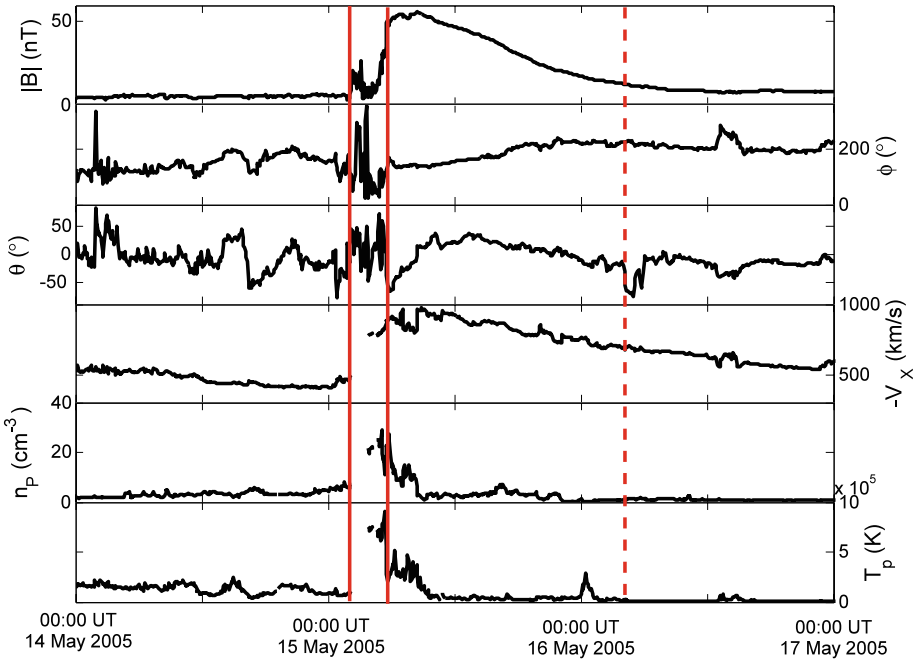

Figure 31 An overview plot of ACE solar wind measurements around the Sun – Earth L_1 point. A full description of the parameters shown can be seen in the text.

are labelled dependent on what values are quoted in the table such as the fast solar wind or the ICME itself. The EISCAT – MERLIN values are taken from Breen *et al.* (2008), but some of the error values have now been re-evaluated and shown in greater detail here.

3.2.3. Near-Earth In-Situ Measurements

Figure 31 shows the *in-situ* magnetic-field and plasma measurements from the ACE spacecraft just upstream of Earth. The panels, from top to bottom, show the magnetic-field magnitude, the in- and out-of-ecliptic magnetic-field angles, the proton bulk speed, the proton density, and the proton temperature. The first solid line shows the IP shock, the second solid line the ICME leading edge (and southward magnetic-field orientation); a possible location of the ICME trailing edge is shown by the dashed line.

When an ICME/MC has a very high velocity (as with this ICME), it significantly compresses the solar wind plasma ahead of it and forms a "collisionless" shock, as shown schematically in Figure 32 taken from Tsurutani *et al.* (2003). The shock wave (caused by the ICME/driver gas) is formed downstream of the ICME/driver leading edge, which not only compresses, but also heats and accelerates the ambient solar-wind plasma ahead of it. In the sheath region between the shock and the ICME leading edge, the magnetic field "piles up" (Siscoe and Odstrcil, 2008) while the plasma is deflected about the obstacle to the flow (Owens and Cargill, 2004; Bisi, 2006; Breen *et al.*, 2008).

The ICME itself is strongly characterised by a smooth rotation in the magnetic-field direction, signifying the passage of a magnetic flux rope (see, *e.g.*, Burlaga, Behannon, and Klein, 1987; Lepping, Burlaga, and Jones, 1990; Burlaga, Lepping, and Jones, 1990). Attempts to model the flux rope and reconstruct the large-scale topology of the ICME are

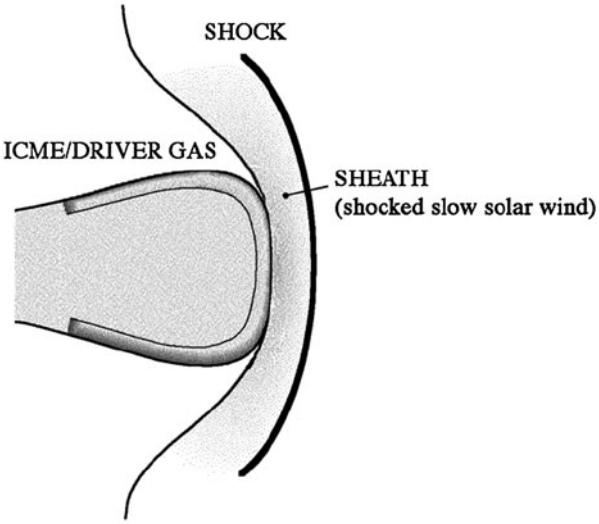

Figure 32 Schematic showing the general overall configuration of a fast CME/ICME/driver and its downstream sheath and subsequent shock (adopted from Tsurutani *et al.*, 2003).

discussed later in this section and also in Section 3.2.2 respectively. Dasso *et al.* (2009) modelled the ICME as two separate MCs using two different models (both different from the one we use here) due to the large size of the overall ICME and the possible double source (the two flare signatures for example). The ICME also exhibits a declining velocity profile (as discussed in Section 3.2.4), indicative of the structure expanding as it passes over the spacecraft (see, *e.g.*, Owens *et al.*, 2005), consistent with the low proton temperature and density within the flux rope.

Since fast CMEs/ICMEs generate IP shocks as they press into the slower solar wind downstream (sticking with the previously-defined convention in Section 1 of "upstream" being in the direction back to the Sun), using the observed photospheric magnetic field as a boundary condition, the steady-state solar wind around the time of the 13 May 2005 CME was reconstructed with the Enlil MHD model (see, *e.g.*, Odstrcil and Pizzo, 2002; Odstrcil, Pizzo, and Arge, 2005). The SOHO|LASCO white-light observations were fit with a "cone" model of a CME (Xie, Ofman, and Lawrence, 2004), which enables determination of the source location, time of eruption, CME angular width and radial speed from the plane-of-sky data. An over-dense plasma bubble with the same characteristics was then inserted into the simulated ambient solar wind in order to predict the ICME-arrival time and speed at Earth (Xie, Ofman, and Lawrence, 2004; Odstrcil, Pizzo, and Arge, 2005). The arrival time was approximately four hours off, and the speed was approximately the same as measured *in situ* (~ 1000 km s^{-1}) (Xie, Gopalswamy, and St. Cyr, 2009). This is a good result, given the various difficulties in modelling such a complex event, but the uncertainties with this simulation seem very large indeed. Our overall findings do not disagree with those of Xie, Gopalswamy, and St. Cyr (2009).

Using the shock travel time from the Sun to the Earth (33 h) and its arrival velocity at 1 AU (~ 1097 km s^{-1}), Lara and Borgazzi (2009) fit the parameters for linear and turbulent drag to the Type II burst spectrum to determine the viscosity (linear) and drag coefficient (turbulent) of the downstream solar wind. Their model assumes the velocity varies linearly from the Sun to the Earth allowing for the position of the CME to be determined in time. The downstream solar wind density decreases by the factor r^{-2}, thus allowing the determination of the plasma frequency at that position as a function of time. The CME driving the shock

Table 7 Table showing a summary of CME and shock characteristics.

Key Characteristics of the 13 May 2005 CME and Associated Shock	
Description	Value
Initial velocity near the Sun	POS 1689 km s^{-1}
Radius stretch factor	0.77
Assumed CME mass	10^{16} g
Downstream solar wind velocity	415 km s^{-1}
Viscosity (laminar)	1.03×10^{21} cm^2 s^{-1}
Drag coefficient (turbulent)	3.94×10^4
Shock *in-situ* (average of laminar and turbulent calculations)	~ 1111 km s^{-1}

is allowed to expand radially giving the cross-sectional area across which the drag forces are acting. Table 7 shows the results of their fits. We find the drag coefficient determined by this method $\approx 4 \times 10^4$ to be remarkable (some 4 – 5 orders of magnitude different) in comparison to the coefficient determined by the model used in Yurchyshyn *et al.* (2006) of just 1.15. This discrepancy is worth further study considering the positive outcomes of both lines of investigation.

The onset of the event *in-situ* is marked by the co-occurrence of a spike in both the density and velocity and typically is where the shock commences. These can be seen in Figure 33 using hourly-averaged data from Sun – Earth L_1 *in-situ* instrumentation: the SOHO – Charge, Element and Isotope Analysis System (SOHO|CELIAS) (Hovestadt *et al.*, 1995); the *Wind* – Solar Wind Experiment (*Wind*|SWE) (Ogilvie *et al.*, 1995); and ACE|SWEPAM. The end of the shock event is marked by the return of the density value near that just before the shock event. The baseline of the density is then determined by the average of the density just before and after the event. The normalised density peak is the maximum density that occurs for the duration of the event with the baseline subtracted out. The value given at the bottom of each figure is the summed particle count that passed by the spacecraft throughout the duration of the shock. The ACE and *Wind* count are approximately the same, but for some reason, the SOHO count is about 50% more than that of the other two spacecraft results. SOHO also saw a much more varied velocity structure. It is possible that the *Wind* and ACE spacecraft were seeing very similar parts of the ICME/MC shock/sheath, but SOHO was perhaps crossing through a slightly-differing region from *Wind* and ACE.

The baseline of the velocity is determined only by the value just before the onset of the shock event. Unlike with density, the velocity takes much longer to reduce back to baseline value due to the radially-extended size of the ICME – shock – sheath combination. The normalised velocity peak is the peak velocity, coinciding with the peak in density, and with the baseline velocity subtracted out. Note however, that the peak velocity is not necessarily the maximum velocity achieved during the entire event but at the commencement of the shock. A summary of these values is given in Table 8.

The particles are counted using the density with the density baseline subtracted out over the duration of the event as we have defined here. The actual velocity is used, no baseline is subtracted out. This can be justified due to the fact that the measured velocities are much more consistent among the different spacecraft instrumentation, in general, as compared with the density values (which for other events has been seen to vary by factors of two to four from instrument-to-instrument measurements), which is not quite the case here however. Unfortunately, a comparison with the IPS using the technique of Jackson *et al.* (2010) with

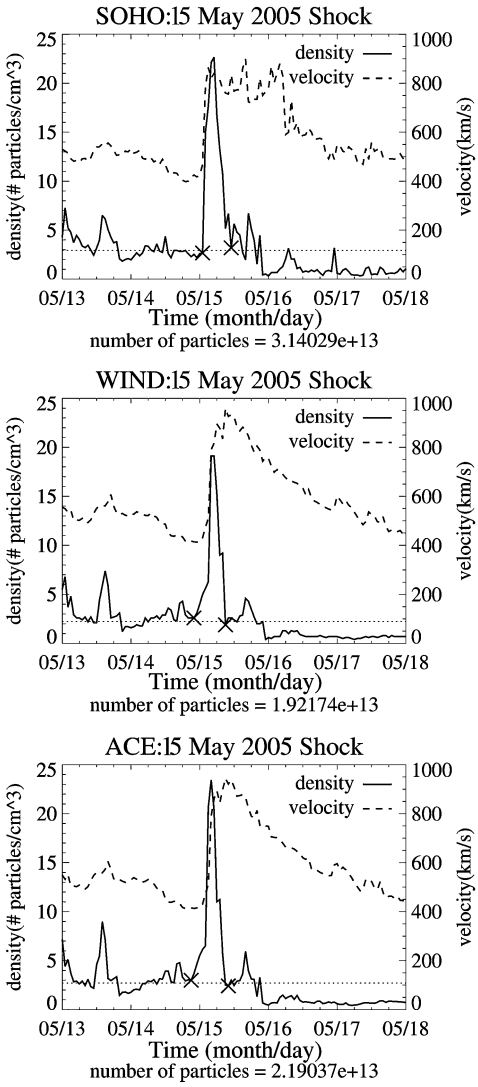

Figure 33 Solar-wind hourly-averaged velocity (dashed line) and density (solid line) profiles of the near-Earth solar-wind plasma for the 14 – 15 May 2005 ICME shock/sheath event measured by SOHO|CELIAS (top), *Wind*|SWE (middle), and ACE|SWEPAM (bottom). The three instruments show a density enhancement of approximately 16.9 cm^{-3} to 20.7 cm^{-3} from the baseline (horizontal dotted line) and a peak velocity of approximately 864 $km\,s^{-1}$ to 953 $km\,s^{-1}$.

SMEI (and STELab IPS velocity combined) reconstruction results is not possible for this event.

Figure 34 shows the electron (top) and proton (bottom) fluxes measured by the Electron, Proton and Alpha Monitor (EPAM) (Gold *et al.*, 1998) aboard the ACE spacecraft. These energetic-particle measurements clearly delineate the events previously identified in this study. The flare onset (a) is associated with an immediate electron enhancement and a delayed proton enhancement. Post flare, the electron and proton fluxes steadily rise, peaking with the arrival of the shock at L_1 (b). Thus, the shock front continued to act as the site of strong electron and proton acceleration throughout its journey from the Sun to the Earth. Particle fluxes dropped sharply with the arrival of the MC leading edge, suggesting particles from the intense magnetic fields and closed structure associated with the magnetic flux rope. Small enhancements of protons within the cloud, however, suggest that secondary flares may

Table 8 Summary results table of the hourly-averaged *in-situ* data from SOHO|CELIAS, *Wind*|SWE, and ACE|SWEPAM solar-wind plasma measurements for the 14 – 15 May 2005 ICME shock/sheath.

Summary results from *in-situ* spacecraft measurements										
Source	Start Date/Time (UT)	End Date/Time (UT)	Time Span (h)	Density Baseline (# cm^{-3})	Dens. Peak (# cm^{-3})	Norm. Den. Peak (# cm^{-3})	Velocity Baseline ($km\,s^{-1}$)	Vel. Peak ($km\,s^{-1}$)	Norm. Vel. Peak ($km\,s^{-1}$)	Particle Count (#)
SOHO	15 May 01:00	15 May 11:00	10	2.93	22.64	19.71	398.9	864.1	465.2	3.14×10^{13}
Wind	14 May 22:00	15 May 09:00	11	2.25	19.10	16.85	414.0	952.7	538.7	1.92×10^{13}
ACE	14 May 21:00	15 May 10:00	13	2.71	23.44	20.73	415.1	946.3	531.2	2.19×10^{13}

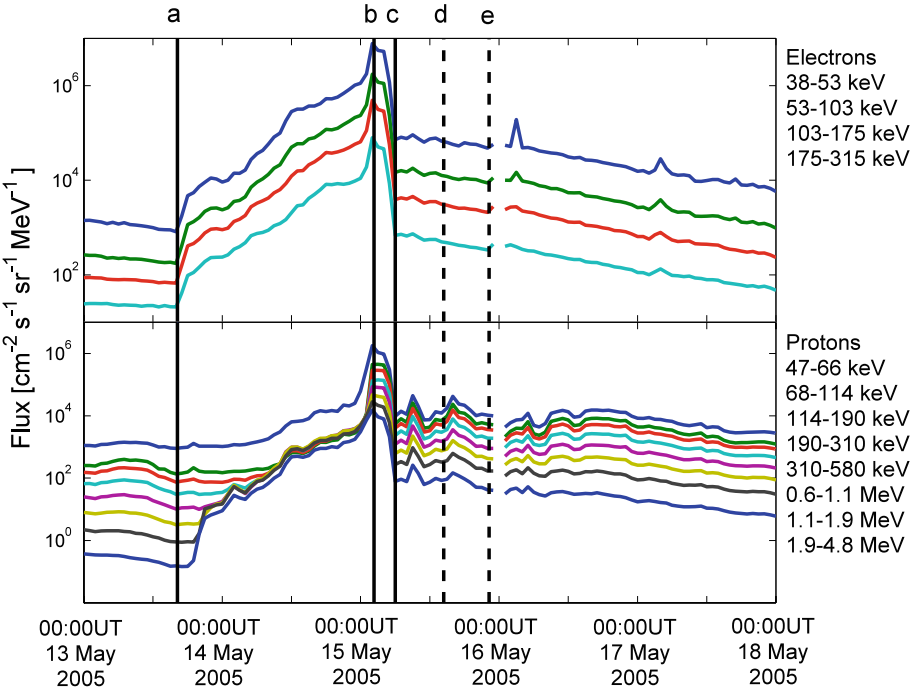

Figure 34 Electron (top) and proton (bottom) fluxes measured by the ACE|EPAM instrument. The solid vertical lines show (a) the EIT flare onset, (b) the observed shock arrival at L_1 and (c) the MC leading edge. The dashed vertical lines show the MC trailing edge, as inferred from (d) the end time of "ideal" *in-situ* magnetic-field measurements (see later in Section 3.2.4 of the text for explanation), and (e) the force-free model.

have injected particles into the ICME itself (see, *e.g.*, Larson *et al.*, 1997). Finally, we note that, as with other interplanetary signatures, the trailing edge of the MC is more difficult to identify: lines (d) and (e) show the "ideal" *in-situ* magnetic-field measurements end time (see Section 3.2.4) and the force-free predictions, respectively.

3.2.4. A Brief Overview of the Inner-Heliosphere Observations and Measurements

Table 9 combines the shock speed values obtained from the DH-km-TII analysis with coronagraph white-light observations, observations of IPS, and *in-situ* measurements, in order to study the temporal speed evolution of the CME/ICME/shock. Column 1 shows the date and Column 2 the time of the measurement as a fraction in UT. Column 3 shows the speed along with its uncertainty in Column 4. Column 5 identifies the instrument/technique used to determine the speed measurement. Since the four IPS-capable systems (EISCAT, MERLIN, STELab, and Ooty) have different receiver/antenna types, the determination of radial velocity ($V_{\rm ips}$) is undertaken using different methods. The ICME was detected *in-situ* by the *Wind* spacecraft. The local shock speed ($V_{\rm shock}$) inferred from *Wind in-situ* data by employing the Rankine – Hugoniot relations. The last two rows of the Table show the shock ($\overline{V_{\rm shock}}$) and ICME transit speed ($\overline{V_{\rm icme}}$), from taking the LASCO – CME observations as the initial time and the shock and *Wind* – ICME observations as the final time. These values show a clear deceleration of both disturbances: the transit speeds are faster than the local ones (*Wind in-situ*).

Table 9 Results of speed determinations by different instruments of the 13 – 15 May 2005 CME/ICME/shock. EISCAT – MERLIN observations are noted as "E – M" and Ooty results are an overall summary of multiple observations. When an "a" is marked next to the date, this denotes when the solar wind was sampled and not that of the CME/ICME/shock; a "–" marks where these values are not available/not measured.

13 – 15 May 2005 CME/ICME/Shock Speeds				
Date (2005)	Hour (UT Fraction)	Speed ($km\,s^{-1}$)	Error in Speed ($\pm km\,s^{-1}$)	Instrument or Technique used
13 May	17.2	(POS) 1689	–	LASCO (CME)
13 May	18.2367	1176	40	WAVES – RAD1
13 May	22.5417	1230	30	WAVES – RAD1
13 May[a]	13.6667 – 16.3333	753	20	E – M IPS (high-lat. wind)
13 May[a]	13.6667 – 16.3333	650	50	E – M IPS (mid-lat. wind)
14 May	2.5	1050	150	Ooty IPS (ICME)
14 May	2.7	1086	192	STELab IPS (ICME)
14 May	2.9	810	48	STELab IPS
14 May	3.75862	826	206	*Wind* – RAD1
14 May	3.8	1093	20	STELab IPS (ICME)
14 May	4.7	1161	54	STELab IPS (ICME)
14 May	12.0	1050	150	Ooty IPS (ICME)
14 May	12.15	916	92	WAVES – RAD1
14 May[a]	14.0 – 14.0833	760	35	E – M IPS (high-lat. wind)
14 May[a]	14.0 – 14.0833	650	75	E – M IPS (low-lat. wind)
14 May[a]	14.1667 – 18.0	719	15	E – M IPS (high-lat. wind)
14 May[a]	14.1667 – 18.0	650	40	E – M IPS (low-lat. wind)
14 May	14.1667 – 18.0	1075	100	E – M IPS (ICME)
15 May	2.25	1100	–	*Wind*|SWE (shock)
15 May	6.0	950	–	*Wind*|SWE (ICME)
15 May	6.0	900	100	Ooty IPS (ICME)
15 May	17.0	900	100	Ooty IPS (ICME)
15 May	2.25	1261	0	transit speed (shock)
15 May	6.0	1132	0	transit speed (ICME)

The interplanetary velocity changes through the progression of the 13 – 15 May 2005 CME/ICME/shock can be seen in Figure 35. This figure shows the interplanetary velocity evolution of the ICME/shock associated with the 13 May 2005 CME. The combination of all the CME/ICME/shock speed determinations show a gradual deceleration as it propagates toward 1 AU, but probably not overall linearly close-in to the Sun.

This comparison of speed determinations should be done carefully. In general, we assume that the Type II radio emission is coming from the region around the ICME/shock nose, but sometimes it may come from other regions along the ICME/shock front. The near-Sun POS LASCO-CME speeds, the shock speeds from the km-TII slope analysis, the sheath region speeds from IPS observations, and the *Wind*-shock and ejecta speeds from *in-situ* magnetic and plasma data do not refer to the same structure but are related to the same phenomena (CME/ICME/shock event).

The Type II radio-burst tracking technique can be summarised as follows. Intervals where the DH-km-TII emission was not contaminated by another kind of emission (*i.e.* Type III

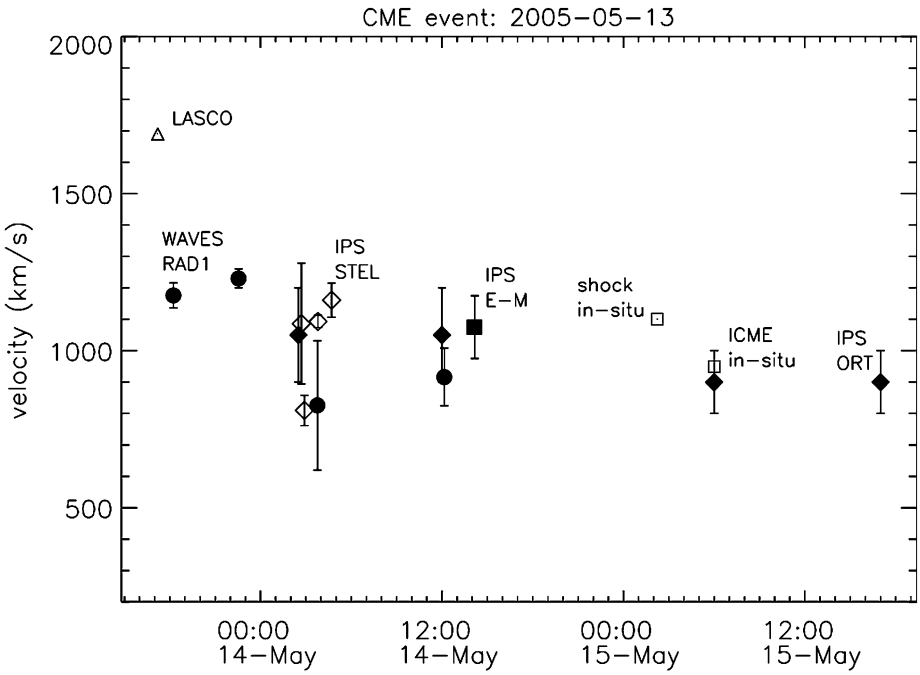

Figure 35 Speed temporal heliocentric evolution of the 13 May 2005 LASCO CME. Combination of speed determinations by different instruments: white-light SOHO|LASCO (open triangle); shock speed obtained from the analysis of the radio km Type II burst drifts (solid circle); IPS STEL/STELab (open diamond); IPS ORT/Ooty (solid diamond); IPS EISCAT-MERLIN/E-M (solid square); and *in-situ Wind* plasma measurements (open square).

radio bursts which occur during this flare/CME event, auroral kilometric radiation – AKR, *etc*.) were identified. The DH-km-TII emission was then isolated and a Gaussian fit (for all spectral data) to the profile of the flux density versus frequency applied to obtain its spectral properties (central frequency, width, and intensity). We only considered those spectra with a well-defined central frequency. Next, the slope of the central frequency drift was obtained by applying a linear fit at some arbitrary interval. Using Equation (3) and the slope of the central frequency emission, the shock speed was then estimated and then these steps repeated at different contiguous intervals to obtain a shock speed distribution. Finally, the mean value of the shock speeds is found and its standard deviation quoted as the associated error. With comparison to the other velocity determinations from near the Sun through to near Earth, we see that there is a strong deceleration curve (not linear near the Sun – suggesting rapid deceleration close to the Sun – but possibly linear deceleration in interplanetary space and out to the Earth) and that our various data sets compare reasonably well with this picture (as shown in Figure 35). There is some discrepancy and question over the originally-quoted-and-regularly-used SOHO|LASCO POS velocity of 1689 $\mathrm{km\,s^{-1}}$ determination in comparison with our much lower bounds (for the two separate fronts before their apparent "merging") using the new technique as seen in Section 3.1 specifically relating to Figure 14.

The overall STELab results show an enhanced turbulence and velocity in the vicinity of the ICME as it propagates out from the Sun. Although the enhanced g-level value (turbulence/density increase) was inconclusive, the velocity distribution shown by the STELab

observations of IPS consistently show an Earth-directed halo-type transient, but with some bias to the north and east. These are somewhat consistent with the SOHO|LASCO analyses.

The overall Ooty results show the passage of the ICME very well on the 14 and 15 May 2005. The observations are also widely spaced in terms of solar elongation (and thus P-Point distance from the Sun). The ICME crosses the distance of around 100 $R_\odot$ to 150 $R_\odot$ on the 14 May with velocities in the range of 750 km s^{-1} to 1150 km s^{-1}. By 15 May, a halo-like ICME can be seen in the Ooty data, which seems to be primarily moving around 10° – 20° east of the Sun – Earth line despite a greater number of IPS radio sources being observed to the west (as with the largest of the mass portions seen in the SOHO|LASCO images and in the STELab 3-D reconstructions). The ICME appears to start to cross the Earth's orbit (solar elongation of 90°) around 06:00 UT – 12:00 UT on 15 May. This is consistent with the timing of near-Earth *in-situ* measurements inside the Earth's magnetosphere for the ICME/MC and the shock/sheath arrival/impact. On 16 May 2005, the ICME passes 250 $R_\odot$ and moves away from the Ooty IPS FOV. However, late on 15 May 2005, there are some ICME signatures around 225 $R_\odot$. These observations are in good agreement with the measurements made by the *Wind* spacecraft instrumentation in the interplanetary medium near Earth.

The ability of ELB IPS observations to detect meridional velocities (see, *e.g.*, Moran *et al.*, 1998; Bisi *et al.*, 2007a) revealed significant polewards deflection of the fast wind near the ICME boundary north of the ICME. This is consistent with over-expansion of the ICME into the fast wind, offering a possible explanation for the north – south feature and lower drag coefficient suggested by Yurchyshyn *et al.* (2006).

The excess mass, as determined from the 3-D tomographic reconstruction of STELab IPS observations, show a fairly consistent and stable value in the region of 6.4×10^{15} g, with energy values between 2.9×10^{31} erg and 4.7×10^{31} erg. The volume increased during its interplanetary transit (as shown in Figure 30) from 0.045 AU^3 to 0.204 AU^3. Lara and Borgazzi (2009) assumed a value for a "typical" CME, when modelling this event, of $\sim 10^{16}$ g: around 50% more than we compute here as an excess mass. However, it should be noted that we are measuring only the excess mass above the ambient. If the ambient were to be added as a total mass for modelling purposes, then the mass would be (our computed total mass values) around 1.4×10^{16} g; this is about 40% more than what was used as an assumption by Lara and Borgazzi (2009) for their modelling. It is likely that the actual mass of the ICME is indeed $\sim 10^{16}$ g, which is consistent with what we calculate here and what was used during the Lara and Borgazzi (2009) modelling.

The 13 May 2005 CME had a smoothly-varying magnetic field, a low proton temperature, and a well-defined counter-streaming-electron flow, indicating that magnetic-field lines in its structure remained connected to the photosphere (Gosling *et al.*, 2006). The orientation of the magnetic flux rope within the ICME was roughly the same at 1 AU as the inferred orientation of the CME based on the density enhancements from its legs in the SOHO|LASCO measurements (Yurchyshyn *et al.*, 2006). However, there is the likelihood of the CME having a double source due to the two flares quite close together in time (the more powerful of the two being the second flare) and also a possibility of there being two MCs within the ICME as it passes over the Sun – Earth L_1 point (as modelled by using two different models, one for each of the two suspected MCs, by Dasso *et al.*, 2009). Table 10 summarises the parameters used to fit the ACE data here using the Lepping, Burlaga, and Jones (1990) magnetic-flux-rope model (see http://lepmfi.gsfc.nasa.gov/mfi/mag_cloud_pub1.html).

Plots of the fit to the flux rope detected in ACE *in-situ* measurements using the method of Lepping, Burlaga, and Jones (1990) can be seen in Figure 36. The Lepping fit, shown with the blue curves, indicates that a force-free solution with no expansion of the rope as it passes

Table 10 Table showing a summary of ACE ICME fitted parameters.

Key Fitted Parameters from ACE ICME Measurements		
Description	Force-Free	Ideal
Start time	15 May 2005 05:42 UT	15 May 2005 05:42 UT
End time	15 May 2005 22:18 UT	15 May 2005 22:18 UT
Axis direction (GSE) longitude and latitude	94° and 67°	90° and 0°
Average solar wind speed	843 km s^{-1}	–
Radius	0.195 AU	–
Axial field magnitude	70.6 nT	70.6 nT
Handedness	Left	Left
Square-root of chi-squared of fit	0.123	–
Asymmetry factor	0.5%	–
CA (of axis relative to the Earth)	75%	80%
Axial magnetic flux	82.5 Mx	82.5 Mx
Axial current density	4.6 μA km^2	4.6 μA km^2
Cone angle	92°	90°
Quality of fit (1 = best; 3 = bad)	2	–

the Earth is too simple for the 15 May 2005 ICME. The fit illustrates two characteristics that indicate the orientation is in error: the magnitude of the total field decreases throughout the time interval, and the strong rotation in the B_z magnetic field from negative to positive is not included in the fit. The B_z rotation indicates that the orientation of the axis is at a lower latitude. ACE data are also shown, and are in black. To test this theory, we set the trailing edge of the structure at the point where the velocity fields in the GSE Y and Z directions dropped to zero; this indicated a change in the dynamics within the ICME structure. The red curves in the figure show the ideal *in-situ* magnetic-field measurements that would be observed by a flux-rope oriented along the GSE Y-axis with an impact parameter at 80% of the radius and a 65 nT magnetic-field magnitude. Clearly the ICME is oriented in the east-west direction; therefore, we conclude that the Yurchyshyn *et al.* (2006) white-light density enhancement in the north-south direction is uncorrelated with the orientation of the ICME. This may be consistent with the two MC structure described by Dasso *et al.* (2009) within the ICME near Earth along with the bias in density to the north and east as seen in the post-processed LASCO imagery and the overall IPS and 3-D reconstruction results.

Also of interest are the two highly-different drag coefficients used by Yurchyshyn *et al.* (2006) and Lara and Borgazzi (2009) being 1.15 and $\sim 4 \times 10^4$ respectively, but still resulting in similar and perhaps suitable results as compared with near-Earth *in-situ* data. As mentioned in Section 3.2.3, this certainly merits further investigation.

3.3. The Earth and its Environment

Here, we describe the effects on the Earth environment and study in detail the magnetospheric response to the 13 – 15 May 2005 CME/ICME/MC event. During the interval studied in the proximity of Earth (15 May 2005 – 00:00 – 12:00 UT), the *Geotail*, four *Cluster*, and Double Star TC2 spacecraft were all initially located in the dayside magnetosphere and were thus ideally placed to observe the effects of the impact of the ICME/MC, and the shock and sheath preceding it on the dayside magnetosphere. Unfortunately, there were no spacecraft located in the magnetotail during this interval. Spacecraft locations plotted in the GSE

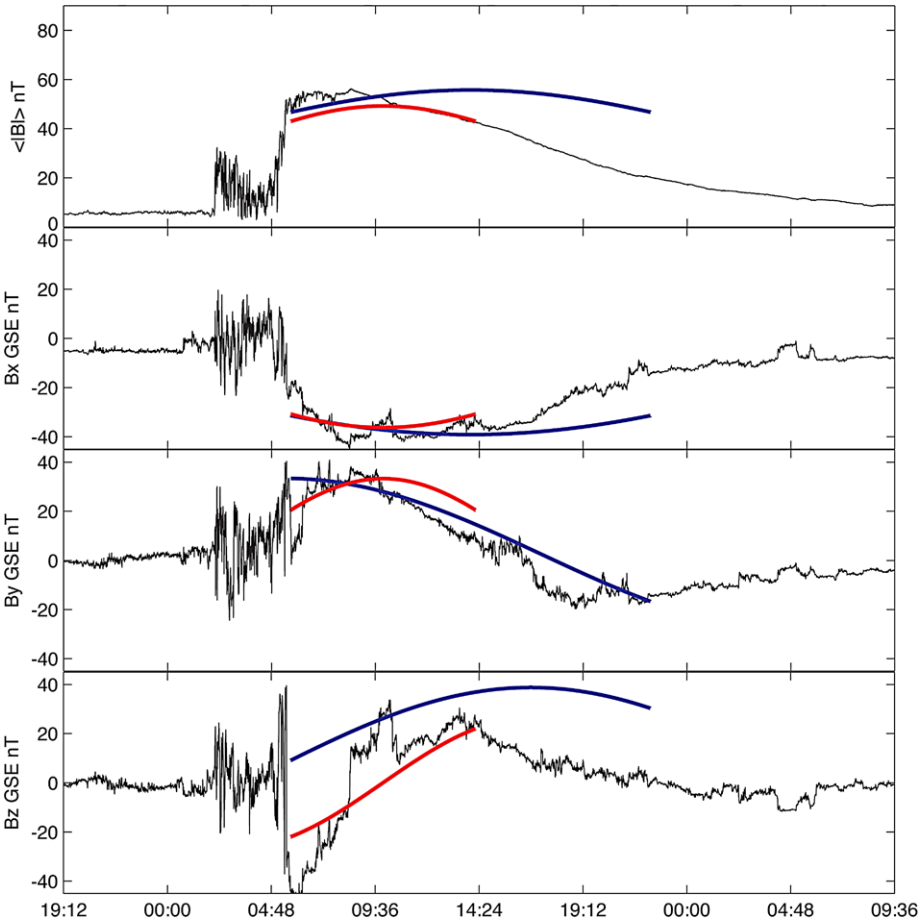

Figure 36 The Lepping fit (dark blue curve) to the ICME ACE *in-situ* measurements (black) along with an ideal curve (in red) that would be measured if the flux rope were oriented along the GSE Y-axis. Full details can be found in the text.

coordinate system (where X points along the Earth – Sun line, positive towards the Sun; Y opposes the orbital motion of the Earth, positive towards dusk; and Z points out of the plane of the ecliptic, positive northwards), can be seen in Figure 37, where distances are in $R_{\oplus}$.

3.3.1. Multi-spacecraft Measurements and Ground-Based Observations of the Effects on the Earth'S Magnetosphere and Ionosphere

At 00:00 UT on 15 May the *Geotail* spacecraft was located on the dawnward flank of the magnetosphere, moving towards perigee close to the location of a model magnetopause. Magnetic-field data from *Geotail*'s Magnetic Field Investigation (MFI) instrument (Kokubun *et al.*, 1994) and ion moments from the Low-Energy Particle (LEP) experiment instrument (Mukai *et al.*, 1994) are plotted in Figure 38. Where multiple vector components are plotted in one panel, the X component is red, Y green, and Z blue. At 02:40 UT (marked by the first dashed line) the spacecraft crosses the magnetopause into the magnetosheath (as evidenced by a sharp increase in the magnetic-field strength, ion density and ion velocity,

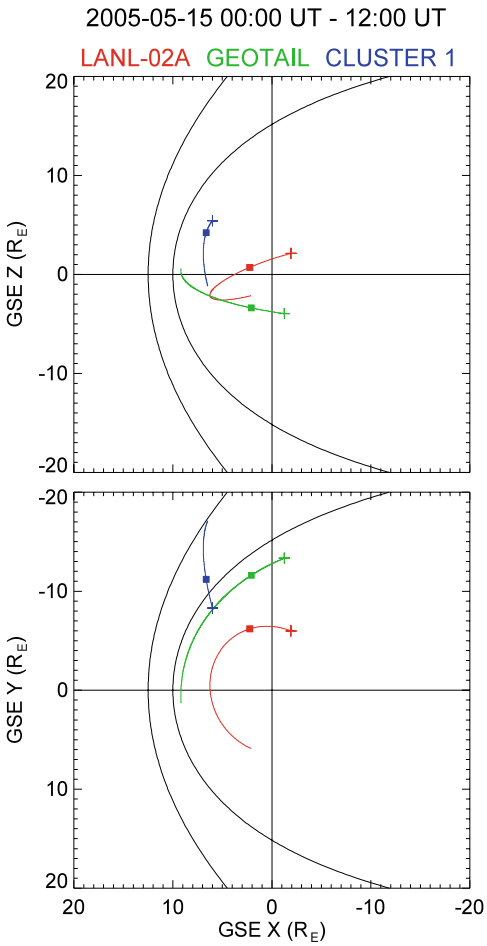

Figure 37 *Geotail* (green) is skimming the dayside magnetosphere, close to the location of a model magnetopause. *Cluster* (blue) is outbound from the magnetosphere into the dawnside magnetosheath. LANL-02A (red) is in a geosynchronous orbit. Spacecraft locations at 00:00 UT are marked by pluses, spacecraft locations at 02:40 UT are marked by solid squares.

and decrease in ion temperature). This turbulent sheath plasma and magnetic field were measured by the spacecraft until ∼06:00 UT (marked by the second dashed line), when the Z component of the magnetic field abruptly turned southward and the field and ion velocity became much less variable. Note that spacecraft data are plotted in GSM coordinates, which are given by a rotation of GSE about the X-axis such that the GSM $X-Z$ plane contains the Earth's magnetic-dipole axis, rather than the normal to the plane of the ecliptic.

The orbit of the *Cluster* spacecraft (only data from *Cluster* 1 will be discussed here) was such that the spacecraft crossed the magnetopause and moved from the magnetosphere into a "normal" undisturbed magnetosheath at 02:00 UT before *Geotail* moved into the magnetosheath. Several *Cluster* instruments were used for this investigation. The magnetic-field data from the Flux Gate Magnetometer (FGM) (Balogh *et al.*, 2001), ion moments from the *Cluster* Ion Spectrometry – Hot Ion Analyser (CIS – HIA) (Reme *et al.*, 2001), and an electron energy-time spectrogram from the Plasma Electron And Current Experiment (PEACE) (Johnstone *et al.*, 1997), are plotted in Figure 39. The 02:00 UT crossing of the magnetopause by the *Cluster* 1 spacecraft, marked by the first dashed line, can be seen as the change from higher energetic magnetospheric electrons to colder magnetosheath electrons of higher flux at that time. At 02:40 UT (marked by the second dashed line) however, the

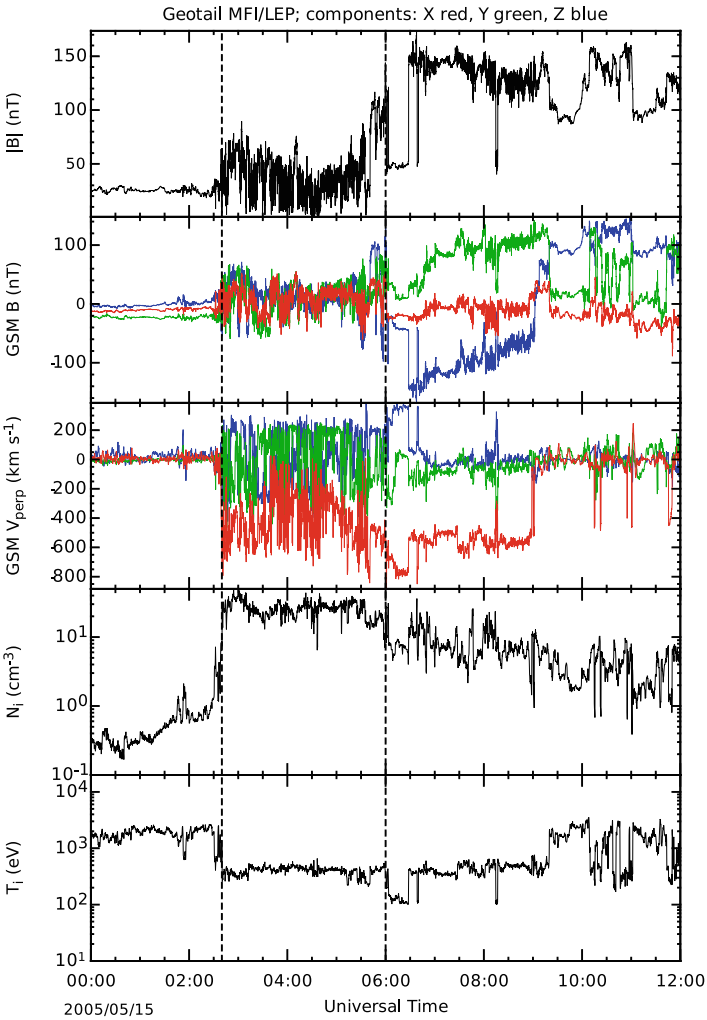

Figure 38 From the top, the panels show magnitude and GSM components of magnetic field, GSM components of $v_\perp$, ion number density, and ion temperature, as measured by the *Geotail* spacecraft.

spacecraft measured a change in the electron distribution, accompanied by an increase in the ion velocity and slight increase in the ion temperature. This hotter, faster sheath plasma continued to be observed until $\sim$ 06:00 UT (marked by the third dashed line) when, like *Geotail*, the *Cluster* spacecraft measured a change in B_Z to a southward direction, accompanied by a decrease in electron fluxes and temperatures.

The change in B_Z to a southward direction (*i.e.* a negative value of θ) was also detected by the *Wind* spacecraft, and by the ACE spacecraft at $\sim$ 05:30 UT at the transition between the sheath of the ICME and the MC flux-rope structure (see Figure 31 showing the ACE data, third panel down, second vertical line). It is our interpretation of the *Geotail* and *Cluster* 1 data therefore, that the IP shock associated with the leading edge of the ICME impacted the Earth's magnetosphere at 02:40 UT, compressing the dayside magnetopause and hence causing *Geotail* to move from the magnetosphere to the magnetosheath. The change in the

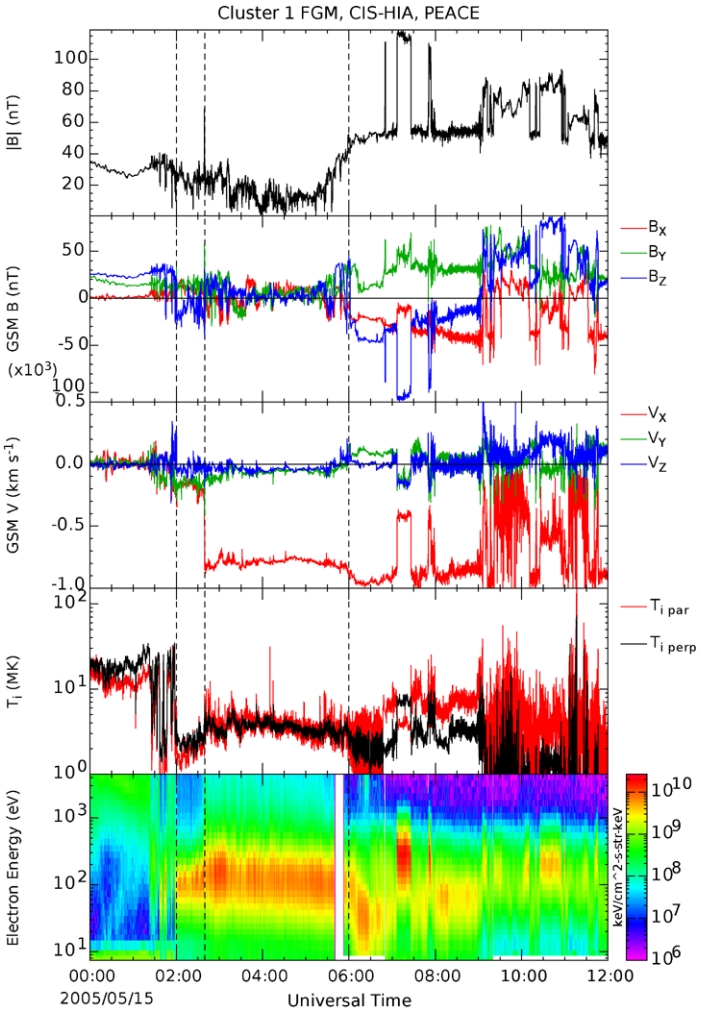

Figure 39 From the top, the panels show magnitude and GSM components of magnetic field, GSM components of ion velocity, ion temperature parallel and perpendicular to the magnetic field, and an energy – time spectrogram plotting omnidirectional differential energy flux of electrons. Dashed lines mark the crossing of the spacecraft from the magnetosphere into the magnetosheath, from undisturbed magnetosheath into the sheath of the MC and finally into the MC itself.

plasma measured by *Cluster* 1 at this time from "normal" magnetosheath to hotter plasma is also consistent with the leading edge of the ICME sheath crossing that spacecraft at this time.

If the *Geotail* data are plotted with various geomagnetic indices (sym-H, AU, AL), an indication of the effect of the IP shock and MC on the magnetosphere – ionosphere system can be ascertained (see Figure 40). First considering sym-H, which is broadly equivalent to *Dst* but at a one-minute resolution (see, *e.g.*, Wanliss and Showalter, 2006), a sharp increase in sym-H can be observed at 02:40 UT, when the IP shock impacted the magnetosphere and *Geotail* was pushed into the magnetosheath. The increase in sym-H is consistent with the

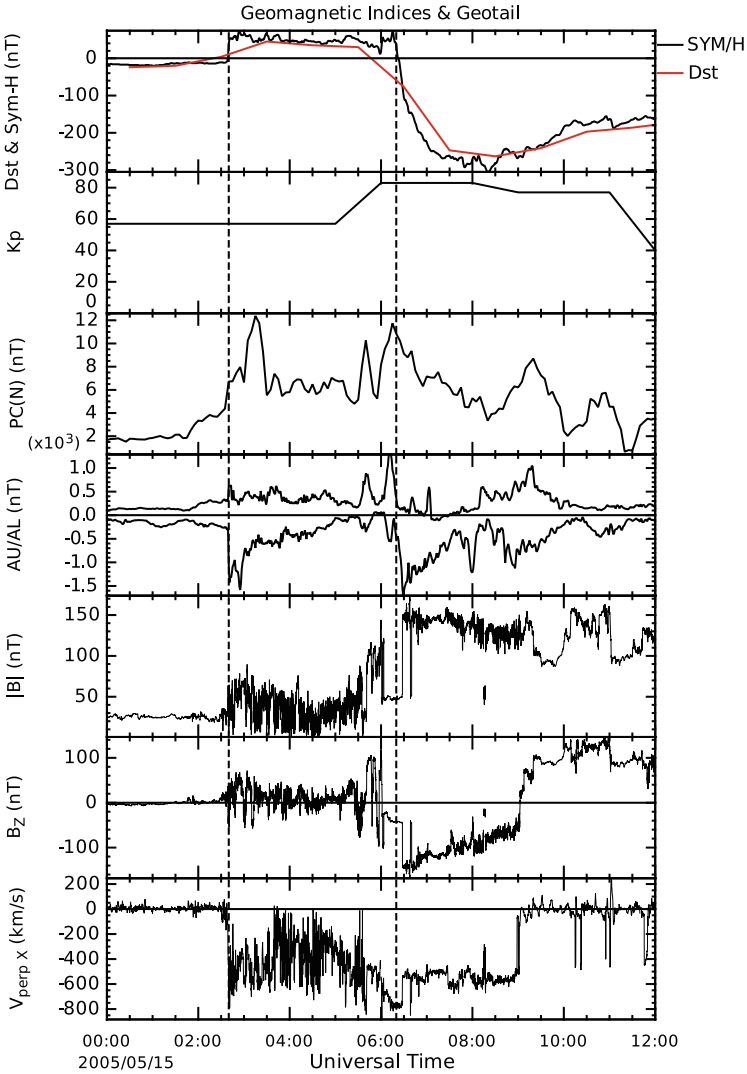

Figure 40 From the top, the panels show the sym-H index (black) along with the *Dst* index (red), *Kp*, PCN, AU and AL indices, the magnitude of magnetic field as measured by *Geotail*, GSM B_Z from *Geotail*, and GSM $v_{\perp X}$ also from *Geotail*.

initial phase of a geomagnetic storm and is caused by an increase in the magnitude of the magnetopause current resulting from the increase in solar wind dynamic pressure (Gonzalez *et al.*, 1994). The IMF in the ICME sheath was predominantly directed northward (Figure 31 third panel) so one might not expect increased dayside reconnection rates during the initial phase of the storm. The main phase of the geomagnetic storm, identified as the decrease in sym-H, began at ∼ 06:00 UT and was coincident with the southward turning of the IMF seen by *Geotail* (Figures 38 and 40) and upstream by ACE some thirty minutes earlier (Figure 31) as the MC itself impacted the magnetosphere. The recovery phase of the storm, identified

as the increase sym-H to quiet-time values, began at ∼ 08:00 UT and continued throughout the day.

The AU and AL indices (Davis and Sugiura, 1966), a measure of the strength of the AEs, showed a transient (∼ 1 h) increase beginning at 02:40 UT; consistent with substorm activity being triggered by the pressure pulse associated with the ICME sheath (see, *e.g.*, Keika *et al.*, 2009). The PCN index also showed a sharp increase from 5.0 nT at 02:30 UT to 11.1 nT at 03:15 UT. It fell to ∼ 6.0 nT between 03:30 UT and 05:45 UT before a second peak value of 10.9 nT occurred at 06:15 UT. Subsequently, it fell to ∼ 3.0 nT at 12:00 UT; although there was significant variation within this decline. The enhanced values between ∼ 03:00 UT and ∼ 08:00 UT suggest enhanced anti-sunward convection within an expanded polar cap. The *Kp* index showed a maximum value of 83 at 06:00 UT before falling to lower values around 40 at 12:00 UT. The *Dst* index fell sharply around 06:00 UT, took a minimum value of −263 nT at 08:00 UT, and then began to recover over several hours. These both indicated geomagnetic disturbances on a global scale occurring a few hours later than the disturbances at high latitudes.

The geomagnetic indices suggest that the ionospheric response to the ICME/MC was consistent with that previously reported by Hanuise *et al.* (2006) on the May 2003 CME events and the response to an associated storm (Ebihara *et al.*, 2005b, 2005a). The disturbances in the AU, AL, and PCN indices were coincident with the impact of the ICME/MC at Earth and indicated the response of the high-latitude ionosphere; namely enhancements in the AEs and the anti-sunward cross-polar transport of plasma. Disturbances in the *Dst* and *Kp* indices occurred some hours later, indicating a delay in the global response to the ICME/MC.

Unfortunately, no auroral data are available until after the geomagnetic storm had begun. Global auroral images from IMAGE Far Ultraviolet Imager – Wideband Imaging Camera (FUV – WIC) (Mende *et al.*, 2000) are available from ∼ 04:50 UT. These images, representative samples of which are plotted in Figure 41, show enhanced auroral brightness visible above the background airglow on the dayside beginning as soon as the data become available and continuing throughout the interval. Unfortunately, the nightside aurora are not in the FOV of the WIC camera until 06:00 UT. However, data from the NORSTAR MSP at the Gillam observation site in Canada (Figure 42), which measures auroral emission at several wavelengths over a narrow longitude range but a wide range of latitude, are available from ∼ 03:30 UT and show the equatorward edge of the nightside aurora moving to lower latitudes. This is consistent with the expansion of the ionospheric polar cap caused by enhanced reconnection at the dayside magnetosphere producing more open magnetic flux (Milan *et al.*, 2006). This is interesting because the predominantly northward-directed IMF in the ICME sheath would not usually be expected to produce such significant open magnetic flux. Component reconnection involving the Y-component of the IMF may be responsible for this; however, recent work by Milan *et al.* (2009) also suggests that the strengthening of the ring current associated with the geomagnetic storm also has the effect of expanding the radius of the auroral oval.

Both the IMAGE FUV and Gillam MSP data show enhanced auroral activity on both the dayside and nightside, where the aurora were much more active than for a typical auroral substorm, as the main phase of the geomagnetic storm began at 06:00 UT. However, the dayside reconnection rate was significantly higher than the nightside, as evidenced by a further expansion of the ionospheric polar cap, visible in the FUV data, as more and more open magnetic flux was added to the magnetosphere. This is entirely consistent with the southward turning of the IMF detected by both *Geotail* and ACE (as previously mentioned) at the transition between the ICME sheath and the MC itself, providing further evidence that

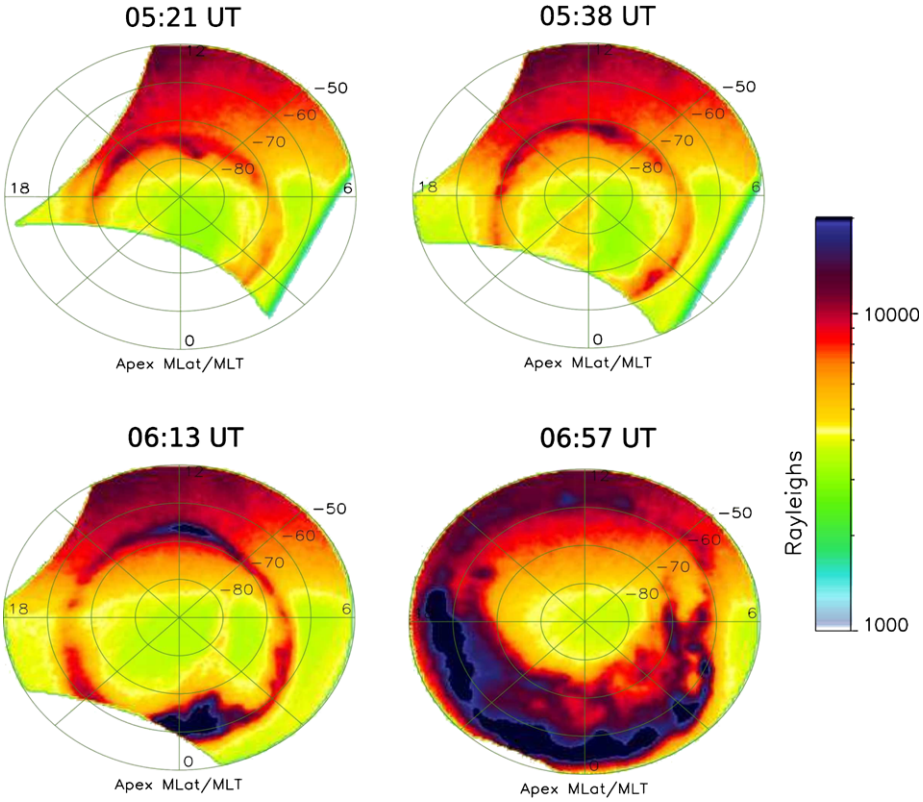

Figure 41 Selected southern hemisphere global auroral images taken by the FUV-WIC camera on board the IMAGE satellite. The images are in a geomagnetic latitude/longitude coordinate system and are plotted such that noon is at the top of each image and midnight at the bottom.

the main phase of this geomagnetic storm was associated with the MC, and the initial phase with compression of the magnetosphere caused by the impact of the IP shock and ICME sheath.

The response of the high-latitude convection pattern and the Birkeland current system in the terrestrial ionosphere to this ICME has been discussed by Eriksson *et al.* (2008). The plasma convection, the Birkeland current system, and the auroral flux were observed by the IMAGE, Thermosphere Ionosphere Mesosphere Energetics and Dynamics (TIMED) (see, *e.g.*, Yee, Cameron, and Kusnierkiewicz, 1999), and US Defense Meteorological Satellite Program (DMSP) satellites. Taken collectively, these showed that a field-aligned current system developed at the poleward edge of the dusk auroral oval when the IMF was directed southward. When the IMF turned northward, a flow channel of sunward-directed plasma in the northern hemisphere was observed between upward and downward field-aligned currents and this structure drifted dawnward across several hours. The upward field-aligned current was coincident with a drifting transpolar arc in the northern hemisphere, but there was no counterpart observed in the southern hemisphere.

The five Los Alamos geosynchronous satellites also detected effects of the impact of the ICME/MC on the magnetosphere. At 02:40 UT, an increase in energetic electron fluxes (not shown here) was detected, consistent with adiabatic heating of the existing electron popula-

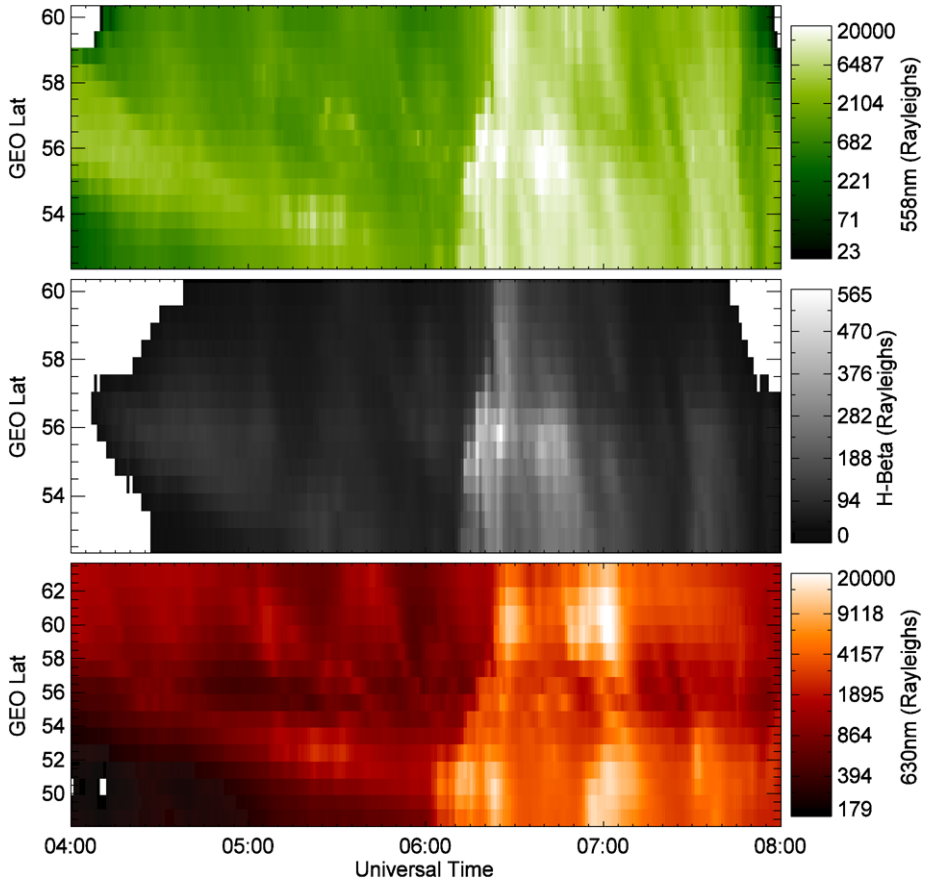

Figure 42 Keograms of auroral emission in three wavelengths as measured by the Gillam NORSTAR MSP. This figure shows the temporal evolution of the latitude of the auroral oval along a narrow longitude range.

tion caused by the compression of the magnetosphere, as was a new injection of energetic particles in the midnight sector. This is consistent with the substorm activity triggered by the magnetospheric compression. By 06:00 UT, the closest LANL spacecraft to local noon was LANL-02A. This spacecraft crossed into the magnetosheath at $\sim$05:50 UT as evidenced by the change in the thermal and suprathermal electron and ion spectra measured by the Magnetosphere Plasma Analyzer (MPA) instruments (Bame *et al.*, 1993) and plotted in Figure 43 (where the first dashed line marks the transition between the magnetosphere and magnetosheath), from a magnetospheric population to a sheath population. The effect of the ICME/MC then, was to compress the dayside magnetosphere to within geosynchronous orbit. This of course may likely have affected nearby geosynchronous satellites.

Double Star TC2 was moving towards its apogee of $\sim 6\ R_{\oplus}$. The spacecraft recorded increased electron fluxes and a dipolarisation (*i.e.* an increase in B_Z) at 02:40 UT. At 05:30 UT, the spacecraft recorded a more variable, turbulent magnetic field, and a change in the electron population to a lower energy distribution dominated by field-aligned and anti-field-aligned particles. At 06:00 UT, the spacecraft observed a southward turning of B_Z, presumably related to the MC passing over the spacecraft. At this time, the bi-directional elec-

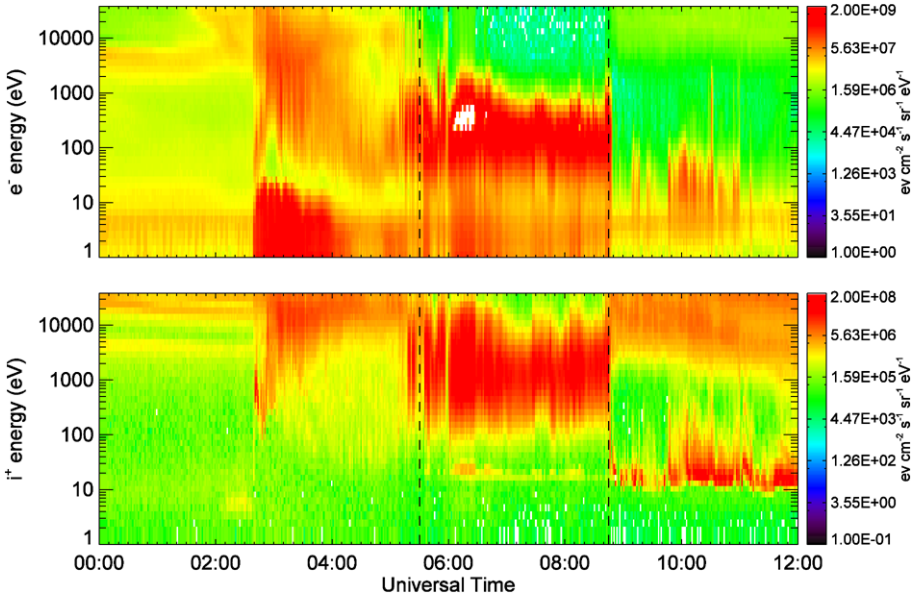

Figure 43 Energy – Time spectrograms plotting omnidirectional differential energy flux as measured by the MPA instruments on LANL-02. This confirms that the spacecraft drops into the sheath at ∼ 06:00 UT.

tron population disappeared and a slightly lower energy isotropic distribution was recorded. These interesting data require further analysis before they can be properly interpreted in the context of the ICME and MC and will likely become subject of a forthcoming paper.

3.3.2. A Brief Overview of the Earth and its Environment Observations and Measurements

The magnetospheric response was large and widespread with the magnetosphere being compressed into geosynchronous orbit. The initial phase of the compression was caused by the impact of the IP shock and ICME sheath, but the main phase of the geomagnetic storm was caused by the southward-turning IMF (and hence associated with the MC features). The ICME/MC effects measured at the Sun – Earth L_1 point quickly progressed onto affecting the Earth's local magnetic environment. A good connection has been made between features seen first measured *in-situ* around L_1 and those a little later seen at the Earth. This was the largest geomagnetic storm of 2005 and its effects were seen throughout the Earth's magnetosphere – ionosphere system.

Enhancements in the AEs, anti-sunward cross-polar plasma transport, and large geomagnetic disturbances all occurred as a result of this storm. The geomagnetic indices suggest that the ionospheric response to this ICME/MC was consistent with that previously reported on the May 2003 CME events by Hanuise *et al.* (2006) and that this also resulted in a similar response to an associated storm (Ebihara *et al.*, 2005b, 2005a).

The detailed response of the high-latitude plasma convection pattern and the Birkeland current system have been discussed by Eriksson *et al.* (2008). When the IMF was directed southwards, a field-aligned current system developed at the poleward edge of the dusk auroral oval. Once the IMF turned northward, a flow channel of sunward-directed plasma in the northern hemisphere was observed between upward and downward field-aligned currents, and over several hours, this flow channel drifted dawnward.

4. Summary and Conclusions

The results discussed here reveal the complexity of this event, but also point towards some conclusions – some specific to this event – and some of more general relevance to CME/ICME/MC studies – as well as certain outstanding questions to be addressed in future studies.

The object of this paper was to draw together as much data as possible concerning the initiation of the 2005 solar eruption, the development of the mass ejection, its propagation through the interplanetary medium and its impact on the Earth, and to attempt to draw some preliminary conclusions about the development of the event. We believe that we have not only succeeded in these aims, but have been able to go beyond them in terms of drawing some general conclusion about the evolution of solar storms and their planetary impact. We also believe that the results described in this paper point towards some important questions to be addressed in future studies.

In relation to the EUV and AR magnetic-field modelling, based on these encouraging results from the vector-magnetic field study on this event, we are now preparing to repeat this study with the full MHD model. The SOHO|CDS intensity measurements show clear signs of the larger flare eruption and also some signs of the earlier, weaker flare (which could also have played a role in the early development and structure of this flare/CME eruption). Using the new method for looking at the SOHO|LASCO coronagraph imagery, we detect a much lower minimum velocity (POS) for a possible two separate and "merging" CME fronts, but further study on this aspect of the event is needed before any significant conclusions can be drawn. It does indicate however, that this new post-processing method by Morgan, Habbal, and Lugaz (2009) could become very useful for other CMEs when a more detailed investigation is warranted.

This paper significantly highlights the importance of observations of interplanetary scintillation (IPS). They show us the grand-scale propagation of the ICME through the interplanetary medium, its changing structure and distribution in the heliosphere, and also gives us insight into the relatively-large non-radial poleward flows of the fast wind to the north as a result of the ICME's passage allowing us to look at the interaction between a travelling ICME and the background solar wind more closely than any other method currently available. No other technique is able to do this on such a scale except for white-light observations using the SMEI instrument (Eyles *et al.*, 2003; Jackson *et al.*, 2004), which unfortunately was not operational during the time of the 13 – 15 May 2005 CME/ICME/MC due to technical problems. Other heliospheric-type imagers could possibly provide improved large-scale results provided an adequate FOV were available (for example, at least the sunward hemisphere of the inner heliosphere in its entirety).

The post-processed LASCO coronagraph images, observations of IPS, 3-D density reconstruction of STELab IPS data, and MC flux-rope fits all show a halo-like structure coming toward the Earth, but all with a bias to the north-east quadrant. This gives some strength to the possibility that there was a secondary eruption which quickly merged with the first in the low corona – this is possibly why both a near-symmetric halo-type structure was seen in coronagraph imagery as well as a north-east dominance later – particularly through the interplanetary environment. This is also a possible agreement with the two separate MCs detected and discussed in some detail by Dasso *et al.* (2009) in the interplanetary medium near the Earth.

We suggest that one of the most important results to emerge in this work is the non-uniform nature of the event, both in the initial CME through the corona and in the ICME in interplanetary space. The ELB IPS results show that the ICME was perturbing the

background fast wind, driving a northward flow, and this is strongly suggestive of ICME over-expansion into the fast wind. This would provide an explanation for the variations in ICME velocities inferred from different observations in interplanetary space, in particular the higher velocity seen in the relatively-high-latitude ELB IPS observation compared with some at lower latitudes. The relative importance of initial velocity structure and subsequent interaction with the solar wind in determining the morphology of the ICME at Earth orbit is an important question which has emerged during this study, and we consider this to be one of the most important contributions of this work to the overall field of Sun – Planet connections. This is (to our knowledge) the most comprehensive speed analysis of an ICME-shock event. We are combining speed determinations by six different instruments illuminating some aspects of the interplanetary evolution of the ICME-shock system.

The magnetospheric effects in summary, along with *Cluster*, *Geotail*, and geomagnetic indices, all give the time of impact of the IP shock and MC sheath on the magnetosphere as 02:40 UT; while the MC itself impacted the magnetosphere at $\sim$ 06:00 UT. The initial phase of the geomagnetic storm was caused by the dynamic pressure increase associated with the ICME sheath, while the storm's main phase was caused by the MC itself. The impact of the ICME/MC compressed the dayside magnetopause in such a way that it was located within geosynchronous orbit, and enhanced reconnection at the dayside caused massive substorm activity seen in ground- and space-based auroral data.

The complexity of even this "typical" CME means that its "evolution" and effects can only be understood by drawing on the widest possible range of data sources and analytic methods (as we have attempted here). It is apparent that the 3-D structure of this event is complex, and that this structure may be determined by asymmetries in the initial eruption as well as by interaction between the ICME/MC and the background solar wind during interplanetary transit. The 3-D structure of the ICME will also play an important role in governing the way in which it couples into the magnetosphere and ionosphere of the Earth. A promising direction for future work will be a comparison of the observational results of this study with 3-D numerical modelling of CME/ICME evolution with coupling into the terrestrial environment.

The AR eruption launched a strong impulsive event, characterised by a clear coronal radio burst and the launch of a fast CME. The SOHO|CDS results show that the initial CME was significantly non-uniform in character, with considerable variation in velocity across it. The interplanetary observations show that the ICME underwent considerable deceleration – almost certainly by interaction with the slower background solar wind ahead of it – and that most of this deceleration took place inside 80 $R_\odot$ – 100 $R_\odot$. There were considerable variations in the ICME velocities measured in interplanetary space, and these appear to reflect the non-uniform nature of the event but give overall good comparison with each other over increasing radial distance from the Sun – the ICME was expanding more rapidly in some regions than others, however. Determining its relative importance and determining the initial CME structure and its subsequent interaction with solar-wind structures and determining the interplanetary structure of the ICME were not possible from this initial study, but this study has emerged as an important question for future work. The ICME passed over the L_1 spacecraft at 02:11 UT on 15 May 2005, and the first magnetospheric response was seen only 29 minutes later – a rapid response. The ionosphere began to respond at 03:15 UT, when the PCN maximum occurred. The event stands as a good example of a fast Earth-directed CME/ICME/MC and thus is a good candidate for extended study.

This event (CME – ICME – MC) was originally thought to be a fairly "simple" solar eruption, and one which could be taken to be a "typical" CME/ICME/MC. The picture which has emerged from this study is of a much more complex event, with a significantly asymmetric

structure which, in turn, is probably important in governing its effects on the space environment of Earth. We are of the opinion that other "apparently simple" eruptions, investigated in the same detail as has been in our study here, would reveal comparable levels of complexity, and thus that this event may be taken to be a "typical" CME in terms of its complex and developing structure (if not in its detailed morphology). The results of this study suggest some additional specific lines of future research. It is clear that both the initial eruptive event and the interplanetary counterpart are significantly asymmetric in structure, and that at least part of the asymmetry apparent in the ICME is as a result of interaction between the ejection and the background solar wind. The relative importance of the initial CME structure and subsequent interaction in determining the ICME structure at 1 AU is, however, unclear, as is the role played by this structure in MC/magnetosphere coupling. Comparisons of observational results with 3-D MHD modelling could prove instructive in both cases, while future event studies – particularly for events with observations/measurements carried out using SMEI and/or the *Solar TErrestrial RElations Observatory* (STEREO) (Kaiser, 2005; Kaiser *et al.*, 2008) twin spacecraft – could provide greater detail on the ICME structure both in interplanetary space and in the vicinity of the Earth, particularly with higher-resolution 3-D reconstruction using SMEI brightness data.

This leaves the necessity of still more study of this event with some aspects and questions of it (and others) left to be answered.

Acknowledgements The University of California, San Diego (UCSD) authors acknowledge the US NSF (grants ATM0331513, ATM0852246, and ATM0925023), US Air Force Office of Scientific Research (AFOSR) (grant FA9550-06-1-0107), and NASA (grant NNG05GG45G) for their funding while working on these analyses and writing up this manuscript. Four of us (R.A. Fallows, A.P. Walsh, A.G. Wood, and A.S. Giunta) were supported by the Science and Technologies Facilities Council (STFC) in the UK during the period when this work was undertaken. Work at Predictive Science was supported by NASA (Heliophysics Theory and Living With A Star programs) and NSF (CISM and SHINE programs). H. Morgan acknowledges the support of NASA (grant NNX08AJ07G) to the Institute for Astronomy, University of Hawaii, for the work on CME image processing. The STELab IPS observations were carried out under the solar wind program of the Solar-Terrestrial Environment Laboratory (STEL) of Nagoya University. The work at Ooty is partially supported by the CAWSES-India Program, which is sponsored by ISRO. Pushchino authors acknowledge the support of the Russian Academy of Sciences Program "Solar Activity and Space Weather". J.A. Gonzalez-Esparza thanks the support of the CONACyT 48494 and DGAPA-PAPIIT (grant IN105310-3) projects. E. Aguilar-Rodriguez thanks the DGAPA-PAPIIT project (grant IN110309-2) and CONACyT project (grant 101625).

The authors would like to thank the directors and staff of EISCAT and MERLIN for their help and for the EISCAT and MERLIN data used in this study. EISCAT is supported by the scientific research councils of China, Finland, France, Germany, Japan, Norway, Sweden, and the United Kingdom (UK). MERLIN is operated by the University of Manchester (UK) on behalf of the STFC. We would also like to extend particular thanks to W.A. Coles and B.J. Rickett of UCSD, for making available their analysis routines, expertise, and advice to us when analysing the EISCAT and MERLIN IPS data. The PHOENIX-2 data were made available by the Radio Astronomy and Plasma Physics group of the Swiss Federal Institute of Technology, Zurich (ETZ). The 40 – 800 MHz radio spectral data are from the Type II Burst Catalogue generated and maintained by the Astrophysikalisches Institut Potsdam. E.A. Jensen thanks L. Jian from the Institute of Geophysics and Planetary Physics (IGPP), University of California, Los Angeles (UCLA), for input to the CME fits, and also T.L. Mulligan of The Aerospace Corporation for useful discussions.

All standard SOHO images used in this article are taken from the Coordinated Data Analysis Workshops (CDAW) CME catalog http://cdaw.gsfc.nasa.gov/CME_list/. The CDAW CME catalog is generated and maintained at the CDAW Data Center by NASA and The Catholic University of America in cooperation with the Naval Research Laboratory. SOHO is a project of international cooperation between ESA and NASA. The authors thank and acknowledge the *Wind* and ACE instrument groups for making their data freely available for scientific use. The authors also acknowledge the ESA *Cluster* Active Archive for provision of *Cluster* data. *Geotail* magnetic field and plasma data were provided by T. Nagai and Y. Saito through DARTS at the Institute of Space and Astronautical Science, JAXA. NORSTAR MSP data are courtesy of the University of Calgary. LANL MPA data were provided by Michelle Thomsen, and the IMAGE-FUV data are courtesy H. Frey and S. Mende. The Polar Cap Index was provided by the Danish Meteorological Institute.

The authors would like to extend special thanks to the referees of this manuscript for their welcome comments, helpful inputs, and the long length of time it will have taken to referee such a long, detailed, and complex paper.

Open Access This article is distributed under the terms of the Creative Commons Attribution Noncommercial License which permits any noncommercial use, distribution, and reproduction in any medium, provided the original author(s) and source are credited.

References

Abramenko, V.I., Yurchishin, V.B.: 1996, Modeling of a linear force-free magnetic field in a bounded domain. *Solar Phys.* **168**, 47 – 63. doi:10.1007/BF00145824.

Aguilar-Rodriguez, E., Gopalswamy, N., MacDowall, R., Yashiro, S., Kaiser, M.L.: 2005, A universal characteristic of type II radio bursts. *J. Geophys. Res.* **110**(A9), 12. doi:10.1029/2005JA011171.

Armstrong, J.W., Coles, W.A.: 1972, Analysis of three-station interplanetary scintillation data. *J. Geophys. Res.* **77**, 4602.

Balogh, A., Carr, C.M., Acuna, M.H., Dunlop, M.W., Beek, T.J., Brown, P., Fornacon, K.H., Georgescu, E., Glassmeier, K.H., Harris, J., Musmann, G., Oddy, T., Schwingenschuh, K.: 2001, The cluster magnetic field investigation: overview of in-flight performance and initial results. *Ann. Geophys.* **19**(10–12, Sp. Iss. SI), 1207 – 1217.

Bame, S.J., McComas, D.J., Barraclough, B.L., Phillips, J.L., Sofaly, K.J., Chavez, J.C., Goldstein, B.E., Sakurai, R.K.: 1992, The Ulysses solar wind plasma experiment. *Astron. Astrophys. Suppl.* **92**(2), 237.

Bame, S.J., McComas, D.J., Thomsen, M.F., Barraclough, B.L., Elphic, R.C., Glore, J.P., Gosling, J.T., Chavez, J.C., Evana, E.P., Wymer, F.J.: 1993, Magnetospheric plasma analyzer for spacecraft with constrained resources. *Rev. Sci. Inst.* **64**(4), 1026 – 1033.

Bewsher, D., Harrison, R.A., Brown, D.S.: 2008, The relationship between EUV dimming and coronal mass ejections. I. Statistical study and probability model. *Astron. Astrophys.* **478**, 897 – 906. doi:10.1051/0004-6361:20078615.

Bisi, M.M.: 2006, Interplanetary scintillation studies of the large-scale structure of the solar wind. Ph.D. Thesis, The University of Wales, Aberystwyth.

Bisi, M.M., Breen, A.R., Fallows, R.A., Thomasson, P., Jones, R.A., Wannberg, G.: 2005, Combined EISCAT/ESR/MERLIN Interplanetary Scintillation Observations of the Solar Wind. In: *ESA SP-592: Solar Wind 11/SOHO 16, Connecting Sun and Heliosphere* **16**. European Space Agency, 593 – 596.

Bisi, M.M., Breen, A.R., Fallows, R.A., Dorrian, G.D., Jones, R.A., Wannberg, G., Thomasson, P., Jordan, C.: 2006, Off-radial flow of the solar wind from EISCAT and MERLIN IPS observations. In: *EOS Trans. AGU, Fall Meeting Supp. – Abstract SH33A-0399* **87**, 52.

Bisi, M.M., Fallows, R.A., Breen, A.R., Habbal, S.R., Jones, R.A.: 2007a, Large-scale structure of the fast solar wind. *J. Geophys. Res.* **112**, A06101. doi:10.1029/2006JA012166.

Bisi, M.M., Jackson, B.V., Fallows, R.A., Breen, A.R., Hick, P.P., Wannberg, G., Thomasson, P., Jordan, C.A., Dorrian, G.D.: 2007b, Combined STELab, EISCAT, ESR, and MERLIN IPS observations of the solar wind. *Proc. SPIE* **6689**, 668911-1. doi:10.1117/12.735443.

Bisi, M.M., Jackson, B.V., Hick, P.P., Buffington, A., Clover, J.M.: 2007c, *Coronal Mass Ejection Reconstructions from Interplanetary Scintillation Data Using a Kinematic Model: A Brief Review* **14**, World Scientific Publishing, Singapore. Chap. 12.

Bisi, M.M., Jackson, B.V., Hick, P.P., Buffington, A., Odstrcil, D., Clover, J.M.: 2008, Three-dimensional reconstructions of the early November 2004 coordinated data analysis workshop geomagnetic storms: analyses of STELab IPS speed and SMEI density data. *J. Geophys. Res.* **113**(A12), A00A11. doi:10.1029/2008JA013222.

Bisi, M.M., Jackson, B.V., Buffington, A., Clover, J.M., Hick, P.P., Tokumaru, M.: 2009a, Low-resolution STELab IPS 3D reconstructions of the whole heliosphere interval and comparison with in-ecliptic solar wind measurements from STEREO and wind instrumentation. *Solar Phys.* **256**, 201 – 217. doi:10.1007/s11207-009-9350-9.

Bisi, M.M., Jackson, B.V., Clover, J.M., Manoharan, P.K., Tokumaru, M., Hick, P.P., Buffington, A.: 2009b, 3-D reconstructions of the early-November 2004 CDAW geomagnetic storms: analysis of Ooty IPS speed and density data. *Ann. Geophys.* **27**, 4479 – 4489.

Bisi, M.M., Fallows, R.A., Breen, A.R., O'Neill, I.J.: 2010a, Interplanetary scintillation observations of stream interaction regions in the solar wind. *Solar Phys.* **261**, 149 – 172, in this issue. doi:10.1007/s11207-009-9471-1.

Bisi, M.M., Jackson, B.V., Hick, P.P., Buffington, A., Clover, J.M., Tokumaru, M., Fujiki, K.: 2010b, Three-dimensional reconstructions and mass determination of the 2008 June 2 LASCO coronal mass ejection using STELab interplanetary scintillation observations. *Astrophys. J. Lett.* **715**, L104 – L108. doi:10.1088/2041-8205/715/2/L104.

Bisi, M.M., Jackson, B.V., Breen, A.R., Dorrian, G.D., Fallows, R.A., Clover, J.M., Hick, P.P.: 2010c, Three-dimensional (3-D) reconstructions of EISCAT IPS velocity data in the declining phase of solar cycle 23. *Solar Phys.*, in press.

Bothmer, V., Schwenn, R.: 1994, Eruptive prominences as sources of magnetic clouds in the solar wind. *Space Sci. Rev.* **70**, 215 – 220. doi:10.1007/BF00777872.

Bothmer, V., Schwenn, R.: 1998, The structure and origin of magnetic clouds in the solar wind. *Ann. Geophys.* **16**, 1 – 24.

Bougeret, J., Kaiser, M.L., Kellogg, P.J., Manning, R., Goetz, K., Monson, S.J., Monge, N., Friel, L., Meetre, C.A., Perche, C., Sitruk, L., Hoang, S.: 1995, Waves: the radio and plasma wave investigation on the Wind spacecraft. *Space Sci. Rev.* **71**, 231 – 263. doi:10.1007/BF00751331.

Bourgois, G., Coles, W.A., Daigne, G., Silen, J., Turunen, T., Williams, P.J.: 1985, Measurements of the solar wind velocity with EISCAT. *Astron. Astrophys.* **144**, 452 – 462.

Breen, A.R., Coles, W.A., Grall, R.R., Klinglesmith, M.T., Markkanen, J., Moran, P.J., Tegid, B., Williams, P.J.S.: 1996a, Eiscat measurements of the solar wind. *Ann. Geophys.* **14**, 1235 – 1245.

Breen, A.R., Coles, W.A., Grall, R., Løvhaug, U.P., Markkanen, J., Misawa, H., Williams, P.J.S.: 1996b, EISCAT measurements of interplanetary scintillation. *J. Atmos. Terr. Phys.* **58**, 507 – 519.

Breen, A.R., Riley, P., Lazarus, A.J., Canals, A., Fallows, R.A., Linker, J., Mikić, Z.: 2002, The solar wind at solar maximum: comparisons of EISCAT IPS and *in situ* observations. *Ann. Geophys.* **20**, 1291 – 1309.

Breen, A.R., Fallows, R.A., Bisi, M.M., Thomasson, P., Jordan, C.A., Wannberg, G., Jones, R.A.: 2006, Extremely long baseline interplanetary scintillation measurements of solar wind velocity. *J. Geophys. Res.* **111**(A10), 8104. doi:10.1029/2005JA011485.

Breen, A.R., Fallows, R.A., Bisi, M.M., Jones, R.A., Jackson, B.V., Kojima, M., Dorrian, G.D., Middleton, H.R., Thomasson, P., Wannberg, G.: 2008, The solar eruption of 2005 May 13 and its effects: long-baseline interplanetary scintillation observations of the Earth-directed coronal mass ejection. *Astrophys. J. Lett.* **683**, L79 – L82. doi:10.1086/591520.

Brekke, A.: 1997, Book Review: Physics of the upper polar atmosphere / Wiley, 1997. *J. Br. Astron. Assoc.* **107**, 222.

Brueckner, G.E., Howard, R.A., Koomen, M.J., Korendyke, C.M., Michels, D.J., Moses, J.D., Socker, D.G., Dere, K.P., Lamy, P.L., Llebaria, A., Bout, M.V., Schwenn, R., Simnett, G.M., Bedford, D.K., Eyles, C.J.: 1995, The large angle spectroscopic coronagraph (LASCO). *Solar Phys.* **162**, 357 – 402.

Buonsanto, M.J.: 1999, Ionospheric storms – a review. *Space Sci. Rev.* **88**, 563 – 601. doi:10.1023/A:1005107532631.

Burlaga, L.F.: 1995, *Interplanetary Magnetohydrodynamics*, Oxford University Press, New York.

Burlaga, L.F., Behannon, K.W., Klein, L.W.: 1987, Compound streams, magnetic clouds, and major geomagnetic storms. *J. Geophys. Res.* **92**, 5725 – 5734. doi:10.1029/JA092iA06p05725.

Burlaga, L.F., Lepping, R.P., Jones, J.A.: 1990, Global configuration of a magnetic cloud. In: *AGU Geophys. Monogr. Ser.* **58**, AGU, Washington, 373 – 377.

Burlaga, L., Sittler, E., Mariani, F., Schwenn, R.: 1981, Magnetic loop behind an interplanetary shock – Voyager, Helios, and IMP 8 observations. *J. Geophys. Res.* **86**, 6673 – 6684. doi:10.1029/JA086iA08p06673.

Canals, A.: 2002, Interplanetary scintillation studies of the solar wind during the rising phase of the solar cycle. Ph.D. Thesis, The University of Wales, Aberystwyth.

Cane, H.V., Sheeley, N.R. Jr., Howard, R.A.: 1987, Energetic interplanetary shocks, radio emission, and coronal mass ejections. *J. Geophys. Res.* **92**, 9869 – 9874. doi:10.1029/JA092iA09p09869.

Canfield, R.C., Hudson, H.S., McKenzie, D.E.: 1999, Sigmoidal morphology and eruptive solar activity. *Geophys. Res. Lett.* **26**, 627 – 630. doi:10.1029/1999GL900105.

Coles, W.A.: 1995, Interplanetary scintillation observations of the high-latitude solar wind. *Space Sci. Rev.* **72**, 211 – 222.

Coles, W.A.: 1996, A bimodal model of the solar wind speed. *Astrophys. Space Sci.* **243**(1), 87 – 96.

Coles, W.A., Rickett, B.J.: 1976, IPS observations of the solar wind speed out of the ecliptic. *J. Geophys. Res.* **81**, 4797 – 4799.

Dasso, S., Mandrini, C.H., Schmieder, B., Cremades, H., Cid, C., Cerrato, Y., Saiz, E., Démoulin, P., Zhukov, A.N., Rodriguez, L., Aran, A., Menvielle, M., Poedts, S.: 2009, Linking two consecutive non-merging magnetic clouds with their solar sources. *J. Geophys. Res. (Space Phys.)* **114**(A13), 2109. doi:10.1029/2008JA013102.

Davis, T.N., Sugiura, M.: 1966, Auroral electrojet activity index a.e. and its universal time variations. *J. Geophys. Res.* **71**(3), 785.

Delaboudinière, J.P., Artzner, G.E., Brunaud, J., Gabriel, A., Hochedez, J.F., Millier, F., Song, X.Y., Au, B., Dere, K.P., Howard, R.A., Kreplin, R., Michels, D.J., Moses, J.D., Defise, J.M., Jamar, C., Rochus, P., Chauvineau, J.P., Marioge, J.P., Catura, R.C., Lemen, J.R., Shing, L., Stern, R.A., Gurman, J.B., Eupert, W.M., Maucherat, A., Clette, F., Cugnon, P., van Dessel, E.L.: 1995, EIT: extreme-ultraviolet imaging telescope for the SOHO mission. *Solar Phys.* **162**, 291 – 312.

Démoulin, P.: 2008, A review of the quantitative links between CMEs and magnetic clouds. *Ann. Geophys.* **26**, 3113 – 3125.

Dennis, B.R., Lin, R.P., Canfield, R.C., Crannell, C.J., Emslie, A.G., Holman, G.D., Hudson, H.H., Hurford, G.J., Ling, J.C., Madden, N.W., Ramaty, R.: 1996, High-energy solar spectroscopic imager (HESSI). In: Rust, D.M. (ed.) *Society of Photo-Optical Instrumentation Engineers (SPIE) Conference Series* **2804**, 228 – 240.

Domingo, V., Fleck, B., Poland, A.I.: 1995, SOHO: The solar and heliospheric observatory. *Space Sci. Rev.* **72**, 81 – 84.

Dungey, J.W.: 1961, Interplanetary magnetic field and the auroral zones. *Phys. Rev. Lett.* **6**, 47 – 48. doi:10.1103/PhysRevLett.6.47.

Ebihara, Y., Fok, M., Sazykin, S., Thomsen, M.F., Hairston, M.R., Evans, D.S., Rich, F.J., Ejiri, M.: 2005a, Ring current and the magnetosphere – ionosphere coupling during the superstorm of 20 November 2003. *J. Geophys. Res.* **110**(A9), 9. doi:10.1029/2004JA010924.

Ebihara, Y., Fok, M., Sazykin, S., Thomsen, M.F., Hairston, M.R., Evans, D.S., Rich, F.J., Ejiri, M.: 2005b, Correction to "Ring current and the magnetosphere – ionosphere coupling during the superstorm of 20 November 2003". *J. Geophys. Res.* **110**(A9), 10290. doi:10.1029/2005JA011373.

Eriksson, S., Hairston, M.R., Rich, F.J., Korth, H., Zhang, Y., Anderson, B.J.: 2008, High-latitude ionosphere convection and Birkeland current response for the 15 May 2005 magnetic storm recovery phase. *J. Geophys. Res. (Space Phys.)* **113**(A12). doi:10.1029/2008JA013139.

Escoubet, C.P., Schmidt, R., Goldstein, M.L.: 1997, Cluster – science and mission overview. *Space Sci. Rev.* **79**, 11 – 32. doi:10.1023/A:1004923124586.

Escoubet, C.P., Fehringer, M., Goldstein, M.: 2001, The Cluster mission – introduction. *Ann. Geophys.* **19**(10–12, Sp. Iss. SI), 1197 – 1200.

Eyles, C.J., Simnett, G.M., Cooke, M.P., Jackson, B.V., Buffington, A., Hick, P.P., Waltham, N.R., King, J.M., Anderson, P.A., Holladay, P.E.: 2003, The solar mass ejection imager (SMEI). *Solar Phys.* **217**, 319 – 347.

Fallows, R.A.: 2001, Studies of the solar wind throughout a solar cycle. Ph.D. Thesis, The University of Wales, Aberystwyth.

Fallows, R.A., Breen, A.R., Dorrian, G.D.: 2008, Developments in the use of EISCAT for interplanetary scintillation. *Ann. Geophys.* **26**, 2229 – 2236.

Fallows, R.A., Breen, A.R., Bisi, M.M., Jones, R.A., Wannberg, G.: 2006, Dual-frequency interplanetary scintillation observations of the solar wind. *Geophys. Res. Lett.* **33**, 11106. doi:10.1029/2006GL025804.

Fallows, R.A., Breen, A.R., Bisi, M.M., Jones, R.A., Dorrian, G.D.: 2007, Interplanetary scintillation using EISCAT and MERLIN: extremely long baselines at multiple frequencies. *Astron. Astrophys. Trans.* **26**, 489 – 500. doi:10.1080/10556790701612197.

Fossi, B.C.M., Noci, G., Poletto, G.: 1992, The Ulysses space mission. *Nuovo Cimento C, Geophys. Space Phys. C* **15**, 493 – 500.

Freeman, M.P., Farrugia, C.J., Burlaga, L.F., Hairston, M.R., Greenspan, M.E., Ruohoniemi, J.M., Lepping, R.P.: 1993, The interaction of a magnetic cloud with the Earth – ionospheric convection in the northern and southern hemispheres for a wide range of quasi-steady interplanetary magnetic field conditions. *J. Geophys. Res.* **98**, 7633 – 7655. doi:10.1029/92JA02350.

Gibson, W.C., Burch, J.L., Scherrer, J.R., Tapley, M.B., Killough, R.L., Volpe, F.A., Davis, W.D., Vaccarello, D.C., Grismore, G., Sakkas, D., Housten, S.J.: 2000, The IMAGE observatory. *Space Sci. Rev.* **91**(1–2), 15 – 50.

Gold, R.E., Krimigis, S.M., Hawkins, S.E. III, Haggerty, D.K., Lohr, D.A., Fiore, E., Armstrong, T.P., Holland, G., Lanzerotti, L.J.: 1998, Electron, proton, and alpha monitor on the advanced composition explorer spacecraft. *Space Sci. Rev.* **86**, 541 – 562. doi:10.1023/A:1005088115759.

Goldstein, H.: 1983, On the field configuration in magnetic clouds. In: *NASA Conference Publication* **228**, 731 – 733.

Gonzalez, W.D., Joselyn, J.A., Kamide, Y., Kroehl, W.W., Rostoker, G., Tsurutani, B., Vasyliunas, V.M.: 1994, What is a geomagnetic storm. *J. Geophys. Res.* **99**(A4), 5771 – 5792.

Gonzalez-Esparza, J.A., Aguilar-Rodriguez, E.: 2009, Speed evolution of fast CME/Shocks with SOHO/LASCO, WIND/WAVES, IPS and *in-situ* WIND data: analysis of kilometric Type-II emissions. *Ann. Geophys.* **27**, 3957 – 3966.

Gopalswamy, N.: 2004, Interplanetary radio bursts. In: Gary, D.E., Keller, C.U. (eds.) *Solar and Space Weather Radio Physics: Current Status and Future Developments 2004*, *Astrophysics and Space Science Library* **314**, Kluwer Academic, Dordrecht, 305 – 333.

Gopalswamy, N.: 2010, Large-scale solar eruptions. In: Gopalswamy, N., Hasan, S.S., Ambastha, A. (eds.) *Heliophysical Processes*, *Astrophysics and Space Science Proceedings*, Springer, Berlin, 53, Chap. 4. doi:10.1007/978-3-642-11341-3_4.

Gopalswamy, N., Aguilar-Rodriguez, E., Yashiro, S., Nunes, S., Kaiser, M.L., Howard, R.A.: 2005, Type II radio bursts and energetic solar eruptions. *J. Geophys. Res.* **110**(A9), 12. doi:10.1029/2005JA011158.

Gosling, J.T.: 1990, Coronal mass ejections and magnetic flux ropes in interplanetary space. In: *AGU Geophys. Monogr. Ser.* **58**, AGU, Washington, 343 – 364.

Gosling, J.T.: 1993, The solar flare myth. *J. Geophys. Res.* **98**, 18937 – 18949. doi:10.1029/93JA01896.

Gosling, J.T., McComas, D.J., Skoug, R.M., Smith, C.W.: 2006, Magnetic reconnection at the heliospheric current sheet and the formation of closed magnetic field lines in the solar wind. *Geophys. Res. Lett.* **33**, 17102. doi:10.1029/2006GL027188.

Haider, S.A., Abdu, M.A., Batista, I.S., Sobral, J.H., Kallio, E., Maguire, W.C., Verigin, M.I.: 2009, On the responses to solar X-ray flare and coronal mass ejection in the ionospheres of Mars and Earth. *Geophys. Res. Lett.* **36**, 13104. doi:10.1029/2009GL038694.

Hanuise, C., Cerisier, J.C., Auchère, F., Bocchialini, K., Bruinsma, S., Cornilleau-Wehrlin, N., Jakowski, N., Lathuillère, C., Menvielle, M., Valette, J., Vilmer, N., Watermann, J., Yaya, P.: 2006, From the Sun to the Earth: impact of the 27 – 28 May 2003 solar events on the magnetosphere, ionosphere and thermosphere. *Ann. Geophys.* **24**, 129 – 151.

Hargreaves, J.K.: 1992, The solar-terrestrial environment: an introduction to geospace – the science of the terrestrial upper atmosphere, ionosphere and magnetosphere. *Comb. Atmos. Space Sci. Ser.* **5**.

Harrison, R.A.: 2003, SOHO observations relating to the association between flares and coronal mass ejections. *Adv. Space Res.* **32**, 2425 – 2437. doi:10.1016/S0273-1177(03)90412-1.

Harrison, R.A., Sawyer, E.C., Carter, M.K., Cruise, A.M., Cutler, R.M., Fludra, A., Hayes, R.W., Kent, B.J., Lang, J., Parker, D.J., Payne, J., Pike, C.D., Peskett, S.C., Richards, A.G., Gulhane, J.L., Norman, K., Breeveld, A.A., Breeveld, E.R., Al Janabi, K.F., McCalden, A.J., Parkinson, J.H., Self, D.G., Thomas, P.D., Poland, A.I., Thomas, R.J., Thompson, W.T., Kjeldseth-Moe, O., Brekke, P., Karud, J., Maltby, P., Aschenbach, B., Bräuninger, H., Kühne, M., Hollandt, J., Siegmund, O.H.W., Huber, M.C.E., Gabriel, A.H., Mason, H.E., Bromage, B.J.I.: 1995, The coronal diagnostic spectrometer for the solar and heliospheric observatory. *Solar Phys.* **162**, 233 – 290. doi:10.1007/BF00733431.

Hewish, A., Scott, P.F., Wills, D.: 1964, Interplanetary scintillations of small diameter radio sources. *Nature* **203**, 1214.

Hill, S.M., Pizzo, V.J., Balch, C.C., Biesecker, D.A., Bornmann, P., Hildner, E., Lewis, L.D., Grubb, R.N., Husler, M.P., Prendergast, K., Vickroy, J., Greer, S., Defoor, T., Wilkinson, D.C., Hooker, R., Mulligan, P., Chipman, E., Bysal, H., Douglas, J.P., Reynolds, R., Davis, J.M., Wallace, K.S., Russell, K., Freestone, K., Bagdigian, D., Page, T., Kerns, S., Hoffman, R., Cauffman, S.A., Davis, M.A., Studer, R., Berthiaume, F.E., Saha, T.T., Berthiume, G.D., Farthing, H., Zimmermann, F.: 2005, The NOAA Goes-12 solar X-ray imager (SXI) 1. Instrument, operations, and data. *Solar Phys.* **226**, 255 – 281. doi:10.1007/s11207-005-7416-x.

Hovestadt, D., Hilchenbach, M., Bürgi, A., Klecker, B., Laeverenz, P., Scholer, M., Grünwaldt, H., Axford, W.I., Livi, S., Marsch, E., Wilken, B., Winterhoff, H.P., Ipavich, F.M., Bedini, P., Coplan, M.A., Galvin, A.B., Gloeckler, G., Bochsler, P., Balsiger, H., Fischer, J., Geiss, J., Kallenbach, R., Wurz, P., Reiche, K., Gliem, F., Judge, D.L., Ogawa, H.S., Hsieh, K.C., Möbius, E., Lee, M.A., Managadze, G.G., Verigin, M.I., Neugebauer, M.: 1995, CELIAS – charge, element and isotope analysis system for SOHO. *Solar Phys.* **162**, 441 – 481. doi:10.1007/BF00733436.

Jackson, B.V., Hick, P.P.: 2005, Three-dimensional tomography of interplanetary disturbances. In: Gary, D., Keller, C.U. (eds.) *Solar and Space Weather Radiophysics: Current Status and Future Developments*, *Astrophysics and Space Science Library* **314**, Kluwer Academic, Dordrecht, 355 – 386. Chap. 17.

Jackson, B.V., Hick, P.P., Kojima, M., Yokobe, A.: 1998, Heliospheric tomography using interplanetary scintillation observations, 1. Combined Nagoya and Cambridge data. *J. Geophys. Res.* **103**(A6), 12049 – 12067.

Jackson, B.V., Hick, P.P., Buffington, A., Kojima, M., Tokumaru, M., Fujiki, K., Ohmi, T., Yamashita, M.: 2003, Time-dependent tomography of hemispheric features using interplanetary scintillation (IPS) remote-sensing observations. In: Velli, M., Bruno, R., Malara, F., Bucci, B. (eds.) *Solar Wind Ten*, *American Institute of Physics Conference Series* **679**, 75 – 78. doi:10.1063/1.1618545.

Jackson, B.V., Buffington, A., Hick, P.P., Altrock, R.C., Figueroa, S., Holladay, P.E., Johnston, J.C., Kahler, S.W., Mozer, J.B., Price, S., Radick, R.R., Sagalyn, R., Sinclair, D., Simnett, G.M., Eyles, C.J., Cooke, M.P., Tappin, S.J., Kuchar, T., Mizuno, D., Webb, D.F., Anderson, P.A., Keil, S.L., Gold, R.E., Waltham, N.R.: 2004, The solar mass-ejection imager (SMEI) mission. *Solar Phys.* **225**, 177 – 207. doi:10.1007/s11207-004-2766-3.

Jackson, B.V., Buffington, A., Hick, P.P., Wang, X., Webb, D.: 2006, Preliminary three-dimensional analysis of the heliospheric response to the 28 October 2003 CME using SMEI white-light observations. *J. Geophys. Res.* **111**(A10), 4. doi:10.1029/2004JA010942.

Jackson, B.V., Bisi, M.M., Hick, P.P., Buffington, A., Clover, J.M., Sun, W.: 2008, Solar mass ejection imager (SMEI) 3D reconstruction of the 27 – 28 May 2003 CME sequence. *J. Geophys. Res.* **113**(A00A15). doi:10.1029/2008JA013224.

Jackson, B.V., Hick, P.P., Buffington, A., Bisi, M.M., Clover, J.M., Hamilton, M.S., Tokumaru, M., Fujiki, K.: 2010, 3D reconstruction of density enhancements behind interplanetary shocks from solar mass ejection imager white-light observations. In: Maksimovic, M., Issautier, K., Meyer-Vernet, N., Moncuquet, M., Pantellini, F. (eds.) *American Institute of Physics Conference Series* **1216**, 659 – 662. doi:10.1063/1.3395953.

Jain, M., Chauhan, M.L., Shrivastava, S.K., *et al.*: 2008, On the relationship of Forbush decrease event of May 2005 with solar parameters. In: *International Cosmic Ray Conference* **1**, 295 – 298.

Johnstone, A., Alsop, C., Burge, S., Carter, P.J., Coates, A.J., Coker, A.J., Fazakerley, A.N., Grande, M., Gowen, R.A., Gurgiolo, C., Hancock, B.K., Narheim, B., Preece, A., Sheather, P.H., Winningham, J.D., Woodliffe, R.D.: 1997, Peace: a plasma electron and current experiment. *Space Sci. Rev.* **79**(1–2), 351 – 398.

Jones, R.A.: 2007, Interplanetary scintillation observations of the inner solar wind. Ph.D. Thesis, The University of Wales, Aberystwyth.

Jones, R.A., Breen, A.R., Fallows, R.A., Bisi, M.M., Thomasson, P., Wannberg, G., Jordan, C.A.: 2006, The solar eruption of May 13 2005: EISCAT and MERLIN observations of a coronal radio burst. *Ann. Geophys.* **24**, 2413 – 2418. www.ann-geophys.net/24/2413/2006/.

Jones, R.A., Breen, A.R., Fallows, R.A., Canals, A., Bisi, M.M., Lawrence, G.: 2007, Interaction between coronal mass ejections and the solar wind. *J. Geophys. Res.* **112**(A11), 8107. doi:10.1029/2006JA011875.

Kaiser, M.L.: 2005, The STEREO mission: an overview. *Adv. Space Res.* **36**, 1483 – 1488. doi:10.1016/j.asr.2004.12.066.

Kaiser, M.L., Kucera, T.A., Davila, J.M., St. Cyr, O.C., Guhathakurta, M., Christian, E.: 2008, The STEREO mission: an introduction. *Space Sci. Rev.* **136**, 5 – 16. doi:10.1007/s11214-007-9277-0.

Kazachenko, M.D., Canfield, R.C., Longcope, D.W., Qiu, J., Des Jardins, A., Nightingale, R.W.: 2009, Sunspot rotation, flare energetics, and flux rope helicity: the eruptive flare on 2005 May 13. *Astrophys. J.* **704**, 1146 – 1158. doi:10.1088/0004-637X/704/2/1146.

Keika, K., Nakamura, R., Baumjohann, W., Angelopoulos, V., Chi, P.J., Glassmeier, K.H., Fillingim, M., Magnes, W., Auster, H.U., Fornacon, K.H., Reeves, G.D., Yumoto, K., Lucek, E.A., Carr, C.M., Dandouras, I.: 2009, Substorm expansion triggered by a sudden impulse front propagating from the dayside magnetopause. *J. Geophys. Res.* **114**, A00C24. doi:10.1029/2008JA013445.

Kleimenova, N.G., Kozyreva, O.V.: 2007, Daytime quasiperiodic geomagnetic pulsations during the recovery phase of the strong magnetic storm of May 15, 2005. *Geomagn. Aeron.* **47**, 580 – 587. doi:10.1134/S0016793207050064.

Klinglesmith, M.: 1997, The polar solar wind from 2.5 to 40 solar radii: results of intensity scintillation measurements. Ph.D. Thesis, University of California, San Diego (UCSD).

Klinglesmith, M.T., Grall, R.R., Coles, W.A.: 1996, 933 MHz IPS velocity measurements at EISCAT. In: *Solar Wind 8* **382**, 180 – 183.

Kojima, M., Kakinuma, T.: 1987, Solar cycle evolution of solar wind speed structure between 1973 and 1985 observed with the interplanetary scintillation method. *J. Geophys. Res.* **92**, 7269 – 7279.

Kokubun, S., Yamamoto, T., Acuna, M.H., Hayashi, K., Shiokawa, K., Kawano, H.: 1994, The geotail magnetic-field experiment. *J. Geomagn. Geoelectr.* **46**(1), 7 – 21.

Kozyreva, O.V., Kleimenova, N.G.: 2007, Geomagnetic pulsations and magnetic disturbances during the initial phase of a strong magnetic storm of May 15, 2005. *Geomagn. Aeron.* **47**, 470 – 480. doi:10.1134/S001679320704007X.

Krall, J., Yurchyshyn, V.B., Slinker, S., Skoug, R.M., Chen, J.: 2006, Flux rope model of the 2003 October 28 – 30 coronal mass ejection and interplanetary coronal mass ejection. *Astrophys. J.* **642**, 541 – 553. doi:10.1086/500822.

Lang, K.R.: 2001, *The Cambridge Encyclopedia of the Sun*, Cambridge University Press, Cambridge.

Lang, J., Thompson, W.T., Pike, C.D., Kent, B.J., Foley, C.R.: 2002, The radiometric calibration of the coronal diagnostic spectrometer. In: Pauluhn, A., Huber, M.C.E., von Steiger, R. (eds.) *The Radiometric Calibration of SOHO (ESA SR-002)* **2**, 105.

Lara, A., Borgazzi, A.I.: 2009, Dynamics of interplanetary CMEs and associated type II bursts. In: Gopalswamy, N., Webb, D.F. (eds.) *IAU Symp.* **257**, 287 – 290. doi:10.1017/S1743921309029421.

Larson, D.E., Lin, R.P., McTiernan, J.M., McFadden, J.P., Ergun, R.E., McCarthy, M., Rème, H., Sanderson, T.R., Kaiser, M., Lepping, R.P., Mazur, J.: 1997, Tracing the topology of the October 18 – 20, 1995, magnetic cloud with $\sim 0.1 - 10^2$ keV electrons. *Geophys. Res. Lett.* **24**, 1911 – 1914. doi:10.1029/97GL01878.

Lepping, R.P., Burlaga, L.F., Jones, J.A.: 1990, Magnetic field structure of interplanetary magnetic clouds at 1 AU. *J. Geophys. Res.* **95**, 11957 – 11965. doi:10.1029/JA095iA08p11957.

Lindsay, G.M., Luhmann, J.G., Russell, C.T., Gosling, J.T.: 1999, Relationships between coronal mass ejection speeds from coronagraph images and interplanetary characteristics of associated interplanetary coronal mass ejections. *J. Geophys. Res.* **104**, 12515 – 12524. doi:10.1029/1999JA900051.

Linker, J.A., Mikić, Z., Bisecker, D.A., Forsyth, R.J., Gibson, S.E., Lazarus, A.J., Lecinski, A., Riley, P., Szabo, A., Thompson, B.J.: 1999, Magnetohydrodynamic modeling of the solar corona during whole Sun month. *J. Geophys. Res.* **104**(A5), 9809.

Lippiello, E., de Arcangelis, L., Godano, C.: 2008, Different triggering mechanisms for solar flares and coronal mass ejections. *Astron. Astrophys.* **488**, L29 – L32. doi:10.1051/0004-6361:200810164.

Liu, C., Lee, J., Yurchyshyn, V., Deng, N., Cho, K., Karlický, M., Wang, H.: 2007, The eruption from a sigmoidal solar active region on 2005 May 13. *Astrophys. J.* **669**, 1372 – 1381. doi:10.1086/521644.

Lockwood, M., Moen, J.: 1999, Reconfiguration and closure of lobe flux by reconnection during northward IMF: possible evidence for signatures in cusp/cleft auroral emissions. *Ann. Geophys.* **17**, 996 – 1011. doi:10.1007/s005850050827.

Lugaz, N., Vourlidas, A., Roussev, I.I., Morgan, H.: 2009, Solar – terrestrial simulation in the STEREO era: the 24 – 25 January 2007 eruptions. *Solar Phys.* **256**, 269 – 284. doi:10.1007/s11207-009-9339-4.

Manoharan, P.K.: 1993, Study of solar wind using single-station interplanetary scintillation. *Bul. Astron. Soc. India* **21**, 383 – 384.

Manoharan, P.K., Ananthakrishnan, S.: 1990, Determination of solar-wind velocities using single-station measurements of interplanetary scintillation. *Mon. Not. Roy. Astron. Soc.* **244**, 691 – 695.

Manoharan, P.K., Kojima, M., Gopalswamy, N., Kondo, T., Smith, Z.: 2000, Radial evolution and turbulence characteristics of a coronal mass ejection. *Astrophys. J.* **530**, 1061 – 1070. doi:10.1086/308378.

Marubashi, K.: 1986, Structure of the interplanetary magnetic clouds and their solar origins. *Adv. Space Res.* **6**, 335 – 338. doi:10.1016/0273-1177(86)90172-9.

McComas, D.J., Bame, S.J., Barker, P., Feldman, W.C., Phillips, J.L., Riley, P., Griffee, J.W.: 1998a, Solar wind electron proton alpha monitor (SWEPAM) for the advanced composition explorer. *Space Sci. Rev.* **86**, 563 – 612. doi:10.1023/A:1005040232597.

McComas, D.J., Riley, P., Gosling, J.T., Balogh, A., Forsyth, R.: 1998b, Ulysses' rapid crossing of the coronal hole boundary. *J. Geophys. Res.* **103**(A2), 1955 – 1967.

Mende, S.B., Heetderks, H., Frey, H.U., Lampton, M., Geller, S.P., Abiad, R., Siegmund, O.H.W., Tremsin, A.S., Spann, J., Dougani, H., Fuselier, S.A., Magoncelli, A.L., Bumala, M.B., Murphree, S., Trondsen, T.: 2000, Far ultraviolet imaging from the image spacecraft. 2. Wideband fuv imaging. *Space Sci. Rev.* **91**(1–2), 271 – 285.

Mendillo, M.: 2006, Storms in the ionosphere: patterns and processes for total electron content. *Rev. Geophys.* **44**(RG4001). doi:10.1029/2005RG000193.

Messmer, P., Benz, A.O., Monstein, C.: 1999, PHOENIX-2: a new broadband spectrometer for decimetric and microwave radio bursts first results. *Solar Phys.* **187**, 335 – 345. doi:10.1023/A:1005194314845.

Mikić, Z., Linker, J.A., Schnack, D.D., Lionello, R., Tarditi, A.: 1999, Magnetohydrodynamic modeling of the global solar corona. *Phys. Plasmas* **6**(5), 2217.

Mikić, Z., Linker, J.A., Lionello, R., Riley, P., Titov, V.: 2009, Modeling the May 13, 2005 CME (oral presentation) SHINE Workshop, Wolfville, Nova Scotia, Canada.

Milan, S.E., Wild, J.A., Grocott, A., Draper, N.C.: 2006, Space- and ground-based investigations of solar wind-magneto sphere – ionosphere coupling. *Adv. Space Res.* **38**(8), 1671 – 1677. doi:10.1016/j.asr.2005.08.009.

Milan, S.E., Hutchinson, J., Boakes, P.D., Hubert, B.: 2009, Influences on the radius of the auroral oval. *Ann. Geophys.* **27**(7), 2913 – 2924.

Moore, R.L., Labonte, B.J.: 1980, The filament eruption in the 3B flare of July 29, 1973 – onset and magnetic field configuration. In: Sheridan, K.V., Dulk, G.A. (eds.) *Solar and Interplanetary Dynamics*, *IAU Symp.* **91**, 207 – 210.

Moore, R.L., Sterling, A.C., Hudson, H.S., Lemen, J.R.: 2001, Onset of the magnetic explosion in solar flares and coronal mass ejections. *Astrophys. J.* **552**, 833 – 848. doi:10.1086/320559.

Moran, P.J., Breen, A.R., Varley, C.A., Williams, P.J.S., Wilkinson, W.P., Markkanen, J.: 1998, Measurements of the direction of the solar wind using interplanetary scintillation. *Ann. Geophys.* **16**, 1259 – 1264.

Morgan, H., Habbal, S.R.: 2007, The long-term stability of the visible F corona at heights of 3 – 6 $R_\odot$. *Astron. Astrophys.* **471**, L47 – L50. doi:10.1051/0004-6361:20078071.

Morgan, H., Habbal, S.R.: 2009, A method for separating CMEs from the quiescent corona. *Astrophys. J.*, in press.

Morgan, H., Habbal, S.R., Woo, R.: 2006, The depiction of coronal structure in white-light images. *Solar Phys.* **236**, 263 – 272. doi:10.1007/s11207-006-0113-6.

Morgan, H., Habbal, S.R., Lugaz, N.: 2009, Mapping the structure of the corona using Fourier backprojection tomography. *Astrophys. J.* **690**, 1119 – 1129. doi:10.1088/0004-637X/690/2/1119.

Mukai, T., Machida, S., Saito, Y., Hirahara, M., Terasawa, T., Kaya, N., Obara, T., Ejiri, M., Nishida, A.: 1994, The low-energy particle (lep) experiment onboard the geotail satellite. *J. Geomagn. Geoelectr.* **46**(8), 669 – 692.

Nishida, A.: 1994, The Geotail mission. *Geophys. Res. Lett.* **21**(25), 2871 – 2873.

Odstrcil, D., Pizzo, V.J.: 2002, Numerical simulation of interplanetary disturbances. In: Sawaya-Lacoste, H. (ed.) *Solspa 2001, Proceedings of the Second Solar Cycle and Space Weather Euroconference* **477**, 281 – 284.

Odstrcil, D., Pizzo, V.J., Arge, C.N.: 2005, Propagation of the 12 May 1997 interplanetary coronal mass ejection in evolving solar wind structures. *J. Geophys. Res.* **110**(A9), 2106. doi:10.1029/2004JA010745.

Ogilvie, K.W., Desch, M.D.: 1997, The Wind spacecraft and its early scientific results. *Adv. Space Res.* **20**, 559 – 568.

Ogilvie, K.W., Chornay, D.J., Fritzenreiter, R.J., Hunsaker, F., Keller, J., Lobell, J., Miller, G., Scudder, J.D., Sittler, E.C. Jr., Torbert, R.B., Bodet, D., Needell, G., Lazarus, A.J., Steinberg, J.T., Tappan, J.H., Mavretic, A., Gergin, E.: 1995, SWE, a comprehensive plasma instrument for the Wind spacecraft. *Space Sci. Rev.* **71**, 55 – 77.

Owens, M., Cargill, P.: 2004, Non-radial solar wind flows induced by the motion of interplanetary coronal mass ejections. *Ann. Geophys.* **22**, 4397 – 4406.

Owens, M.J., Cargill, P.J., Pagel, C., Siscoe, G.L., Crooker, N.U.: 2005, Characteristic magnetic field and speed properties of interplanetary coronal mass ejections and their sheath regions. *J. Geophys. Res.* **110**(A9), 1105. doi:10.1029/2004JA010814.

Pizzo, V.J., Hill, S.M., Balch, C.C., Biesecker, D.A., Bornmann, P., Hildner, E., Grubb, R.N., Chipman, E.G., Davis, J.M., Wallace, K.S., Russell, K., Cauffman, S.A., Saha, T.T., Berthiume, G.D.: 2005, The NOAA Goes-12 solar X-ray imager (SXI) 2. Performance. *Solar Phys.* **226**, 283 – 315. doi:10.1007/s11207-005-7417-9.

Reiff, P.H., Burch, J.L.: 1985, IMF b(y)-dependent plasma flow and Birkeland currents in the dayside magnetosphere. II – a global model for northward and southward IMF. *J. Geophys. Res.* **90**, 1595 – 1609. doi:10.1029/JA090iA02p01595.

Reiner, M.J., Kaiser, M.L., Fainberg, J., Stone, R.G.: 1998, A new method for studying remote type II radio emissions from coronal mass ejection-driven shocks. *J. Geophys. Res.* **103**, 29651 – 29664. doi:10.1029/98JA02614.

Reme, H., Aoustin, C., Bosqued, M., Dandouras, I., Lavraud, B., Sauvaud, J.A., Barthe, A., Bouyssou, J., Camus, T., Coeur-Joly, O., Cros, A., Cuvilo, J., Ducay, F., Garbarowitz, Y., Medale, J.L., Penou, E., Perrier, H., Romefort, D., Rouzaud, J., Vallat, C., Alcayde, D., Jacquey, C., Mazelle, C., d'Uston, C., Mobius, E., Kistler, L.M., Crocker, K., Granoff, M., Mouikis, C., Popecki, M., Vosbury, M., Klecker, B., Hovestadt, D., Kucharek, H., Kuenneth, E., Paschmann, G., Scholer, M., Sckopke, N., Seidenschwang, E., Carlson, C.W., Curtis, D.W., Ingraham, C., Lin, R.P., McFadden, J.P., Parks, G.K., Phan, T., Formisano, V., Amata, E., Bavassano-Cattaneo, M.B., Baldetti, P., Bruno, R., Chionchio, G., Lellis, A.D., Marcucci, M.F., Pallocchia, G., Korth, A., Daly, P.W., Graeve, B., Rosenbauer, H., Vasyliunas, V., McCarthy, M., Wilber, M., Eliasson, L., Lundin, R., Olsen, S., Shelley, E.G., Fuselier, S., Ghielmetti, A.G., Lennartsson, W., Escoubet, C.P., Balsiger, H., Friedel, R., Cao, J.B., Kovrazhkin, R.A., Papamastorakis, I., Pellat, R., Scudder, J., Sonnerup, B.: 2001, First multispacecraft ion measurements in and near the Earth's magnetosphere with the identical cluster ion spectrometry (cis) experiment. *Ann. Geophys.* **19**(10–12, Sp. Iss. SI), 1303 – 1354.

Rickett, B.: 1992, IPS observations of the solar wind velocity and microscale density irregularities in the inner solar wind. In: *Solar Wind Seven Colloquium*, 255 – 258.

Riley, P., Bame, S.J., Barraclough, B.L., Feldman, W.C., Gosling, J.T., Hoogeveen, G.W., McComas, D.J., Phillips, J.L., Goldstein, B.E., Neugebauer, M.: 1997, ULYSSES solar wind plasma observations at high latitudes. *Adv. Space Res.* **20**, 15.

Riley, P., Linker, J.A., Mikić, Z.: 2001, An empirically-driven global MHD model of the corona and inner heliosphere. *J. Geophys. Res.* **106**(A8), 15889.

Riley, P., Linker, J.A., Mikić, Z., Lionello, R.: 2001, MHD modeling of the solar corona and inner heliosphere: comparison with observations. In: Song, P., Singer, H.J., Siscoe, G.L. (eds.) *Space Weather*, *Geophys. Monogr. Ser.* **125**, AGU, Washington, 159.

Rishbeth, H., Williams, P.J.S.: 1985, Ionospheric Radar: the system and its early results. *Mon. Not. Roy. Astron. Soc.* **26**, 478 – 512.

Rostoker, G., Samson, J.C., Creutzberg, F., Hughes, T.J., McDiarmid, D.R., McNamara, A.G., Jones, A.V., Wallis, D.D., Cogger, L.L.: 1995, Canopus – a ground-based instrument array for remote-sensing the high-lattitude ionosphere during the istp/ggs program. *Space Sci. Rev.* **71**(1 – 4), 743 – 760.

Russell, C.T., Mulligan, T.: 2002, The true dimensions of interplanetary coronal mass ejections. *Adv. Space Res.* **29**, 301 – 306. doi:10.1016/S0273-1177(01)00588-9.

Scherrer, P.H., Bogart, R.S., Bush, R.I., Hoeksema, J.T., Kosovichev, A.G., Schou, J., Rosenberg, W., Springer, L., Tarbell, T.D., Title, A., Wolfson, C.J., Zayer, I., MDI Engineering Team: 1995, The solar oscillations investigation – Michelson Doppler Imager. *Solar Phys.* **162**, 129 – 188. doi:10.1007/BF00733429.

Schwenn, R., dal Lago, A., Huttunen, E., Gonzalez, W.D.: 2005, The association of coronal mass ejections with their effects near the Earth. *Ann. Geophys.* **23**, 1033 – 1059.

Shishov, V.I., Shishova, T.D.: 1979, Influence of source sizes on the spectra of interplanetary scintillations – observations. *Sov. Astron.* **23**, 345.

Shishov, V.I., Tyul'Bashev, S.A., Subaev, I.A., Chashei, I.V.: 2008, Monitoring of interplanetary and ionospheric scintillation of an ensemble of radio sources. *Solar Syst. Res.* **42**, 341 – 350. doi:10.1134/S0038094608040072.

Siscoe, G., Odstrcil, D.: 2008, Ways in which ICME sheaths differ from magnetosheaths. *J. Geophys. Res.* **113**(A12), A00B07. doi:10.1029/2008JA013142.

Smith, C.W., L'Heureux, J., Ness, N.F., Acuna, M.H., Burlaga, L.F., Scheifele, J.: 1998, The ACE magnetic fields experiment. *Space Sci. Rev.* **86**(1 – 4), 613 – 632.

Stone, E.C., Frandsen, A.M., Mewaldt, R.A., Christian, E.R., Margolies, D., Ormes, J.F., Snow, F.: 1998, The advanced composition explorer. *Space Sci. Rev.* **86**, 1 – 22. doi:10.1023/A:1005082526237.

Summers, H.P.: 2004, The ADAS Manual, Version 2.6. World Wide Web. http://www.adas.ac.uk/manual.php, accessed November 2009.

Swarup, G., Sarma, N.V.G., Joshi, M.N., Kapahi, V.K., Bagri, D.S., Damle, S.V., Ananthakrishnan, S., Balasubramanian, V., Bhave, Sinha, R.P.P.: 1971, Large steerable radio telescope at Ootacamund, India. *Nature* **230**, 185.

Thomasson, P.: 1986, MERLIN. *Quart. J. Roy. Astron. Soc.* **27**, 413 – 431.

Troshichev, O.A., Andrezen, V.G., Vennerstrom, S., Friis-Christensen, E.: 1988, Magnetic activity in the polar cap – a new index. *Planet. Space Sci.* **36**, 1095 – 1102. doi:10.1016/0032-0633(88)90063-3.

Tsurutani, B.T., Gonzalez, W.D., Lakhina, G.S., Alex, S.: 2003, The extreme magnetic storm of 1 – 2 September 1859. *J. Geophys. Res.* **108**, 1268. doi:10.1029/2002JA009504.

Tverskaya, L.V., Ginzburg, E.A., Ivanova, T.A., Pavlov, N.N., Svidsky, P.M.: 2007, Peculiarities of the outer radiation belt dynamics during the strong magnetic storm of May 15, 2005. *Geomagn. Aeron.* **47**, 696 – 703. doi:10.1134/S0016793207060023.

Wanliss, J.A., Showalter, K.M.: 2006, High-resolution global storm index: *Dst versus* SYM-H. *J. Geophys. Res.* **111**(A2). doi:10.1029/2005JA011034.

Wannberg, G., Wolf, I., Vanhainen, L.G., Koskenniemi, K., Röttger, J., Postila, M., Markkanen, J., Jacobsen, R., Stenberg, A., Larsen, R., Eliassen, S., Heck, S., Huuskonen, A.: 1997, The EISCAT Svalbard Radar, a case study in modern incoherent scatter radar system design. *Radio Sci.* **32**, 2283 – 2307.

Wannberg, G., Vanhainen, L.G., Westman, A., Breen, A.R., Williams, P.J.S.: 2002, The new 1420 MHz dual polarisation interplanetary scintillation (IPS) facility at EISCAT. In: *Conference Proceedings*, Union of Radio Scientists (URSI).

Widing, K.G.: 1978, Forbidden lines of Fe XIX, Fe XX, and Fe XXI in solar flares. *Astrophys. J.* **222**, 735 – 739. doi:10.1086/156192.

Wolfson, J., Bruner, M., Jurcevich, B., Lemen, J., Schrijver, K., Shine, R., Strong, K., Tarbell, T., Title, A., Golub, L., Bookbinder, J., Deluca, E., Acton, L., Handy, B., Kankelborg, C., Fisher, R.: 1997, The TRACE mission. *Bull. Am. Astron. Soc.* **29**, 887.

Wood, A.G., Pryse, S.E., Middleton, H.R., Howells, V.S.C.: 2008, Multi-instrument observations of nightside plasma patches under conditions of IMF Bz positive. *Ann. Geophys.* **26**, 2203 – 2216.

Xie, H., Ofman, L., Lawrence, G.: 2004, Cone model for halo CMEs: application to space weather forecasting. *J. Geophys. Res.* **109**(A18), 3109. doi:10.1029/2003JA010226.

Xie, H., Gopalswamy, N., St. Cyr, O.C.: 2009, Modeling and prediction of fast CME/shocks associated with type II bursts. In: Gopalswamy, N., Webb, D.F. (eds.) *IAU Symp.* **257**, 489 – 491. doi:10.1017/S1743921309029755.

Yee, J., Cameron, G.E., Kusnierkiewicz, D.Y.: 1999, Overview of TIMED. In: Larar, A.M. (ed.) *Society of Photo-Optical Instrumentation Engineers (SPIE) Conference Series* **3756**, 244 – 254.

Yurchyshyn, V., Liu, C., Abramenko, V., Krall, J.: 2006, The May 13, 2005 eruption: observations, data analysis and interpretation. *Solar Phys.* **239**, 317 – 335. doi:10.1007/s11207-006-0177-3.

Zhang, J., Richardson, I.G., Webb, D.F., Gopalswamy, N., Huttunen, E., Kasper, J.C., Nitta, N.V., Poomvises, W., Thompson, B.J., Wu, C.C., Yashiro, S., Zhukov, A.N.: 2007a, Solar and interplanetary

sources of major geomagnetic storms ($Dst \leq -100$ nT) during 1996 – 2005. *J. Geophys. Res.* **112**(A11), 10102. doi:10.1029/2007JA012321.

Zhang, J., Richardson, I.G., Webb, D.F., Gopalswamy, N., Huttunen, E., Kasper, J.C., Nitta, N.V., Poomvises, W., Thompson, B.J., Wu, C.C., Yashiro, S., Zhukov, A.N.: 2007b, Correction to "Solar and interplanetary sources of major geomagnetic storms ($Dst \leq -100$ nT) during 1996 – 2005". *J. Geophys. Res.* **112**(A11), 12103. doi:10.1029/2007JA012891.